

2006-01-19

Functional MRI Data Analysis Techniques and Strategies to Map the Olfactory System of a Rat Brain.

Praveen P. Kulkarni
Worcester Polytechnic Institute

Follow this and additional works at: <https://digitalcommons.wpi.edu/etd-dissertations>

Repository Citation

Kulkarni, P. P. (2006). *Functional MRI Data Analysis Techniques and Strategies to Map the Olfactory System of a Rat Brain..* Retrieved from <https://digitalcommons.wpi.edu/etd-dissertations/37>

This dissertation is brought to you for free and open access by [Digital WPI](#). It has been accepted for inclusion in Doctoral Dissertations (All Dissertations, All Years) by an authorized administrator of Digital WPI. For more information, please contact wpi-etd@wpi.edu.

**Functional MRI Data Analysis Techniques and Strategies to Map the
Olfactory System of a Rat Brain.**

by

Praveen P. Kulkarni

A Dissertation

Submitted to the Faculty

of

Worcester Polytechnic Institute

In partial fulfillment of the requirements for the

Degree of Doctor of Philosophy in

Mechanical Engineering

by

December 2005

APPROVED:

Prof. John M. Sullivan, Jr.,
Advisor.

Prof. Reinhold Ludwig,
Committee Member.

Prof. Craig F. Ferris,
Committee Member.

Prof. Brian J. Savidonis,
Committee Member.

Prof. Grétar Tryggvason,
Department Head.

Abstract

Understanding mysteries of a brain represents one of the great challenges for modern science. Functional magnetic resonance imaging (fMRI) has two features that make it unique amongst other imaging modalities used in behavioral neuroscience. First, it can be entirely non-invasive and second, fMRI has the spatial and temporal resolution to resolve patterns of neuronal activity across the entire brain in less than a minute. fMRI indirectly detects neural activity in different parts of the brain by comparing contrast in MR signal intensity prior to and following stimulation. Areas of the brain with increased synaptic and neuronal activity require increased levels of oxygen to sustain this activity. Enhanced brain activity is accompanied by an increase in metabolism followed by increases in blood flow and blood volume. The enhanced blood flow usually exceeds the metabolic demand exposing the active brain area to high level of oxygenated hemoglobin. Oxygenated hemoglobin increases the MR signal intensity that can be detected in MR scanner.

This relatively straight forward scenario is, unfortunately, oversimplified. The fMRI signal change to noise ratio is extremely small. In this work a quantitative analysis strategy to analyze fMRI data was successfully developed, implemented and optimized for the rat brain. Therein, each subject is registered or aligned to a complete volume-segmented rat atlas. The matrices that transformed the subject's anatomy to the atlas space are used to embed each slice within the atlas. All transformed pixel locations of the anatomy images are tagged with the segmented atlas major and minor regions creating a fully segmented representation of each subject.

This task required the development of a full 3D surface atlas based upon 2D non-uniformly spaced 2D slices from an existing atlas. A multiple materials marching cube (M3C) algorithm was used to generate these 1277 subvolumes. After this process, they were coalesced into a dozen major zones of the brain (amygdaloid complex, cerebrum, cerebellum, hypothalamus, etc.). Each major brain category was subdivided into approximately 10 sub-major zones. Many scientists are interested in behavior and reactions to pain, pleasure, smell, for example. Consequently, the 3D volume atlas was segmented into functional zones as well as the anatomical regions. A utility (program) called Tree Browser was developed to interactively display and choose different anatomical and/or functional areas.

Statistical t-tests are performed to determine activation on each subject within their original coordinate system. Due to the multiple t-test analyses performed, a false-positive detection controlling mechanism was introduced. A statistical composite of five components was created for each group. The individual analyses were summed within groups. The strategy developed in this work is unique as it registers segments and analyzes multiple subjects and presents a composite response of the whole group. This strategy is robust, incredibly fast and statistically powerful.

The power of this system was demonstrated by mapping the olfactory system of a rat brain. Synchronized changes in neuronal activity across multiple subjects and brain areas can be viewed as functional neuro-anatomical circuits coordinating the thoughts, memories and emotions for particular behaviors using this fMRI module.

Acknowledgement

Professor John M. Sullivan Jr. has been the motivation behind this dissertation and he has taken great pains to go out of his way to guide me through this endeavor. His untiring efforts and support are everything I could have asked for in an advisor.

I would like to express my deepest gratitude to, Prof. Craig Ferris for his patience and countless hours spent helping refining the fMRI module. His guidance gave this work an enhanced direction. Also I would like to thank Prof. Jean King for her support and guidance.

I would like to thank Prof. Ludwig and Prof. Savilonis and Prof. Tryggvason for consenting to be a part of my thesis committee.

I would like to thank all the members of the CCNI (WPI) laboratory especially Dr. J. Zhang and Udo Benz for their constant help and support. I want to thank Hamid, Murali, Huang Wei and Rostislav; they were more than just lab mates.

I would like to thank Tara Messenger for her help in conducting MRI experiments. I also want to thank everybody at CCNI (UMASS) especially Wei Chen, Marcelo Febo, Mat Brevard, Josie Harder, Karl Schmidt, Feng Luo and Steve Bird for their suggestions.

There are too many people to list who have kept my spirit alive during my stay at WPI. ME department staff: Barbara Furman, Barbara Edilberti and Pamela St. Louis. My friends: Viren, Souvik, Siju, Chirag, Radha, Jayant and last but not least Gana who have borne my tantrums. My parents who have shown me the way by example and inspired everything I have done. Priti and Prasanna: for their love and support. I would like to express my gratitude to Tara and Shashank for their constant encouragement throughout my stay in Worcester. Finally I would like to thank Swati for her patience and confidence in me.

This work has been funded, in part, by NIH Grant No. 1 R01 DA 13517-01, NIH Grant No. P01 CA80139, and the ME Dept. Summer Scholarship Fund.

List of Contents

Abstract.....	ii
Acknowledgement	iv
List of Contents.....	v
List of Figures.....	ix
List of Tables	xiv
1: Introduction.....	1
1.1 Brain Mapping Techniques.....	2
1.1.1 Lesions	2
1.1.2 Direct stimulation of exposed cortical tissue.....	2
1.1.3 Intra-cranial stimulation and recording.....	2
1.1.4 Temporary lesions and stimulation via TMS and TES.....	2
1.1.5 Electromagnetic recording.....	3
1.1.6 Hemodynamic response to neural activity.....	3
1.2 fMRI data Analysis.....	5
1.3 Outline	6
2: MRI and fMRI.....	8
2.1 Overview of MR imaging.....	8
2.2 Spin in Magnetic Field.....	9
2.3 Radio Frequency field and MR signal.....	11
2.4 Relaxation Processes.....	15
2.4.1 T_1 relaxation.....	15
2.4.2 T_2 relaxation.....	16
2.5 Magnetic Resonance Imaging.....	19
2.5.1 Slice Selection.....	19
2.5.2 Frequency Encoding	20
2.5.3 Phase Encoding.....	21
2.6 MRI Sequences.....	22
2.6.1 Spin Echo Pulse Sequence.....	23
2.6.2 Gradient Recalled Echo Pulse Sequences.....	23

2.7 Functional MRI (fMRI)	24
2.7.1 Hemodynamics	27
2.7.2 Event-Related Functional MRI	28
2.7.3 Statistical Testing.....	29
3: The Rat Brain Atlas	30
3.1 Swanson Rat Brain Atlas	30
3.1.1 Discrepancies of the atlas.....	32
3.1.2 Multiple lines and curves bundled into a single boundary	33
3.1.3 Nonintersecting or over-extended spline segments	34
3.1.4 Overlapping regions.....	35
3.1.5 Remotely labelled regions.....	35
3.1.6 Other issues	36
3.2 Making Computationally Robust Data	37
3.2.1. Spline Approximation.....	37
3.2.2 Extend/Intersect/Merge.....	38
3.2.3 Identify brain regions.....	41
3.2.4 Overlapping Areas:	45
3.2.5 Mirroring and output.....	46
3.3 Converting data into Pixel image set	46
3.4 Atlas 3D	47
3.5 Classification of Anatomical area: (The Tree Browser).....	48
4: Registration, Segmentation and Data Analysis.....	51
4.1 Coordinate system and their transforms	52
4.1.1 Image-to-world Transform.....	53
4.1.2 World-to-image Transform.....	54
4.1.3 Image-to-image Transform	55
4.2 Registration.....	55
4.2.1 Manual Registration.....	56
4.2.2 Landmark Registration.....	57
4.2.3 Intensity-Based Registration.....	60
4.2.3.1 Correlation Coefficient (CC)	60

4.2.3.2 Squared Intensity Difference (SSD)	61
4.2.3.3 Ratio Image Uniformity (RIU)	61
4.2.3.4 Mutual Information (MI)	62
4.3 Registration strategy	63
4.3.1 Intra Registration	64
4.3.2 Inter Registration	64
4.4 Segmentation	65
4.4.1 Mapping MRI image	67
4.4.2 Integrated volume approach [30]	68
4.5 Statistical Analysis of BOLD data	69
4.5.1 Understanding fMRI data	70
4.5.2 fMRI experimental Design	71
4.5.2.1 Block Design	71
4.5.2.2 Event Related design (single epoch)	72
4.5.3 Data Analysis	73
4.5.3.1 Subtraction technique	74
4.5.3.2 Student's t-test	75
4.5.3.3 Correlation technique	77
4.5.3.4 General Linear Model [99]	80
4.6 Multiple Comparison	81
4.6.1 Bonferroni correction	82
4.6.2 False discovery rate	82
5: fMRI Module in MIVA	86
5.1 Project	87
5.2 Registration	88
5.2.1 Intra Modality Registration	90
5.2.2 Inter-Modality Registration	93
5.2.2.1 4-Point Fiducial Registration	93
5.2.2.2 N Point Fiducial Registration	97
5.2.3 Merge-Registration	98
5.3 Segmentation	99

5.4 T-test Analysis	100
5.5 Results.....	102
6: Mapping Olfactory System.....	106
6.1 Main Olfactory System.....	107
6.2 Methods and Material.....	110
6.2.1 Animals	110
6.2.2 Animal Restrainer	110
6.2.3 Acclimating Animals to the Imaging Protocol	111
6.2.4 Imaging Protocol.....	112
6.3 Experiment Design	114
6.4 Data Analysis.....	117
6.5 Results and Discussion	120
7: Conclusion	124
References.....	126

List of Figures

Figure 1.1: This figure schematically summarizes the state of knowledge of localization of human functional brain in 1957.	1
Figure 1.2: Classification of Brain mapping techniques.....	5
Figure 2.1: A charged, spinning nucleus creates a magnetic moment which acts like a bar magnet.....	9
Figure 2.2 : (a) A collection of ^1H nuclei (spinning protons) in the absence of an externally applied magnetic field. The magnetic moments have random orientations. (b) An external magnetic field B_0 is applied which causes the nuclei to align themselves in one of two orientations with respect to B_0 (denoted parallel and anti-parallel).[10]	10
Figure 2.3: (a) In the presence of an externally applied magnetic field, B_0 , nuclei are constrained to adopt one of two orientations with respect to B_0 . As the nuclei possess spin, these orientations are not exactly at 0 and 180 degrees to B_0 . (b) A magnetic moment precessing around B_0 . Its path describes the surface of a cone.	11
Figure 2.4: A collection of spins at any given instant in an external magnetic field, B_0 . A small net magnetisation, M , is detectable in the direction of B_0	12
Figure 2.5: (top) The effect of RF radiation on the net magnetization M is to produce a second magnetic field M_{x-y} . M is tilted from its original longitudinal z-axis orientation, along the direction of the external magnetic field B_0 , into the transverse x-y plane. (bottom) An illustration of flip angle, which is the angle through which M has rotated away from the z-axis.	14
Figure 2.6: (a) After a 90 degrees RF pulse, M lies in the x-y plane and rotates about the z-axis. The component of M in the x-y plane decays over time. An alternating current, shown in Figure (b), is induced in the receiver coil.....	15
Figure 2.7: Formation of a spin echo at time TE after a 90 degree pulse.	18
Figure 2.8: Dephasing of the magnetization vector by T_2^* and rephasing by a 180 degree pulse to form a spin echo.	18
Figure 2.9: Decay of signal with time in a spin echo sequence.	19
Figure 2.10: Two FIDs and their Fourier transforms.....	21

Figure 2.11: Schematic of interactions in the formation of BOLD signal.
Positive/negative arrow indicates positive/negative correlations between the parameters.
The right most pathway is the most significant effect in most BOLD fMRI..... 27

Figure 2.12: Typical time course for activation related signal in T2 weighted (BOLD) functional MRI..... 28

Figure 3.1: Based on complexity of the different brain levels, Swanson has used a variable number of sections per unit length of the brain. [12]..... 31

Figure 3.2: Left: Original Nissl-stained brain photomicrographs. Right: Freehand drawing of the brain and delineation of the neuroanatomical region using *AI*TM software [12]..... 31

Figure 3.3: Left: A part of a brain map in *AI*[®] with preview mode on, Right: same section with preview mode off. Notice the bundled lines and curves in the boundary of the regions 34

Figure 3.4: An example of un-connected spline in the brain map 34

Figure 3.5: Overlapping regions in rat brain atlas 35

Figure 3.6: Dart-shaped symbols indicate the direction of the boundaries which are supposed to exist (red dashed lines)..... 36

Figure 3.7: Spline Approximation Red curve is the spline which has been roughly approximated by assuming just two values of 0 and 1 as for its parameter..... 38

Figure 3.8: The same spline approximated with for line segments, corresponding to t values of 0, 0.25, 0.75 and 1. 38

Figure 3.9: Above: Open node lies in the E2 element box, thus it is snapped into element. Below: Open node is outside the box, so it is directly connected to endpoint of the E2... 39

Figure 3.10: Merging redundant elements 40

Figure 3.11: Using seed points to identify regions of the brain and assigning material codes to the defining boundary elements. 42

Figure 3.12: Finding the isolated islands and figuring out the second material code..... 43

Overlapping areas 43

Figure 3.13: Line crossing algorithm to identify regions defined by line segments..... 44

Figure 3.14: Removing the void loops whose elements have just one material code..... 46

Figure 3.15: The Rat brain axial slice after segmentation. Each colored area defines unique anatomical area.....	47
Figure 3.16: The Tree Browser with Rat Brain Shell.	49
Figure 3.17: The Tree Browser with four anatomical areas.....	49
Figure 3.18: The Tree Browser with functional area (Reward System)	50
Figure 4.1: Image and World Coordinate System.....	52
Figure 4.2: Classification of Image registration techniques.	56
Figure 4.3: Manual Registration. (a) Registration pallet. (b) Before registration and (c) After registration. [18]	57
Figure 4.4: shows a simple example of 2D landmark registration between an MR image and a rat brain atlas. (a) Landmarks chosen on Subject and Atlas. (b) Before registration (c) After registration.....	60
Figure 4.5: Classification of segmentation algorithms.	66
Figure 4.6: Show fMRI data registered to a segmented rat atlas. A magnified 2x2 pixel region of the fMRI data shows that the problem is one of classifying each fMRI voxel with that material from the higher resolution dataset that best approximates the voxel space.....	68
Figure 4.7: a) Subject voxels classified based on atlas material located at the centroid of MRI subject voxel. b) Improved algorithm based on material with greatest frequency of occurrence within subject voxel. c) XOR operation on Figures a and b to contrast the two methods. Note that a significant number of pixels have been reclassified.	69
Figure 4.8: a) three dimensional MR image slices. b) bottom image is single slice collected at different time points and top image is plot of intensity of one voxel in time.	70
Figure 4.9 Typical types of block designs.	72
Figure 4.10: Block diagram of single epoch event related design paradigm.....	73
Figure 4.11: Various reference functions that can be used to correlate with a pixel time course to detect activations. [97].....	79
Figure 5.1: fMRI Module: Project	87
Figure 5.2: fMRI module: Intra-R registration Panel.....	90

Figure 5.3: How to choose two panel view port and display atlas and standard image side by side.	94
Figure 5.4: Markers created on Atlas image as well as on anatomy image.	94
Figure 5.5: fMRI Module: Inter Registration Palate.....	96
Figure 5.6: fMRI Module: Merge-R Palate.....	98
Figure 5.7: fMRI Module: Segmentation Palate.....	100
Figure 5.8: fMRI module: Analyze palate.	101
Figure 5.9: Design of fMRI experiment.....	101
Figure 5.10: Positive, negative activation and <i>p</i> value map.....	103
Figure 5.11: Time history chart of ROI.	104
Figure 5.12: The Composite data summery sheet.....	105
Figure 6.1: Section through the nasal cavity of a rat. [49].....	107
Figure 6.2: Olfactory epithelium of a rat with a schematic representation of an olfactory sensory neuron.[49].....	108
Figure 6.3: Rat olfactory system.....	109
Figure 6.4: Studies were performed with a multi-concentric dual-coil, small animal restrainer developed by Insight Neuroimaging Systems, LLC, (Worcester, MA).....	111
Figure 6.5: With repeated restraint and exposure to a simulated imaging session rats show reduced autonomic and endocrine measures of stress [67].....	112
Figure 6.6: Bruker Biospec 4.7T/40cm horizontal magnet (Oxford Instruments, U.K.) equipped with a Biospec Bruker console (Bruker, MA, U.S.A) and a 20-G/cm magnetic field gradient insert.	113
Figure 6.7: Block diagram for CO ₂ challenge.....	115
Figure 6.8: Schematic diagram of 1% odorant challenge.	115
Figure 6.9: Motion artifact assessments by subtraction of images.	116
Figure 6.10: Registration of four different subjects to standard subject.....	117
Figure 6.11: Registration of standard image to Rat Atlas.....	118
Figure 6.12: Composite map of ten different subjects was created to map olfactory system.....	119
Figure 6.13: Activation in primary olfactory system due to four odorants.....	120

Figure 6.14: Comparison of number of voxels activated in different ROIs of Primary Olfactory system	121
Figure 6.15: Whole brain responses from four odorants axial and coronal views.....	122
Figure 6.16: Comparison of number of activated voxels of three odorants with Benzaldehyde	123

List of Tables

Table 1.1 Comparison of Brain Mapping Technique.	5
Table 2.1 Physiological and MR parameter changes due to increased neuronal activity..	25
Table 4.1 Classification of voxels in V simultaneous tests.....	83

1: Introduction

Understanding mysteries of a brain represents one of the great challenges for modern science. It has long been known that extensive localization exists within the brain. A schematic summary of such knowledge, published in the late 1950s, is shown in Figure1 (The vertebrate visual system; Stephen Polyak 1957) [1]. What was the basis for this figure? Where did the data come from? What were the technologies that gave rise to this data?

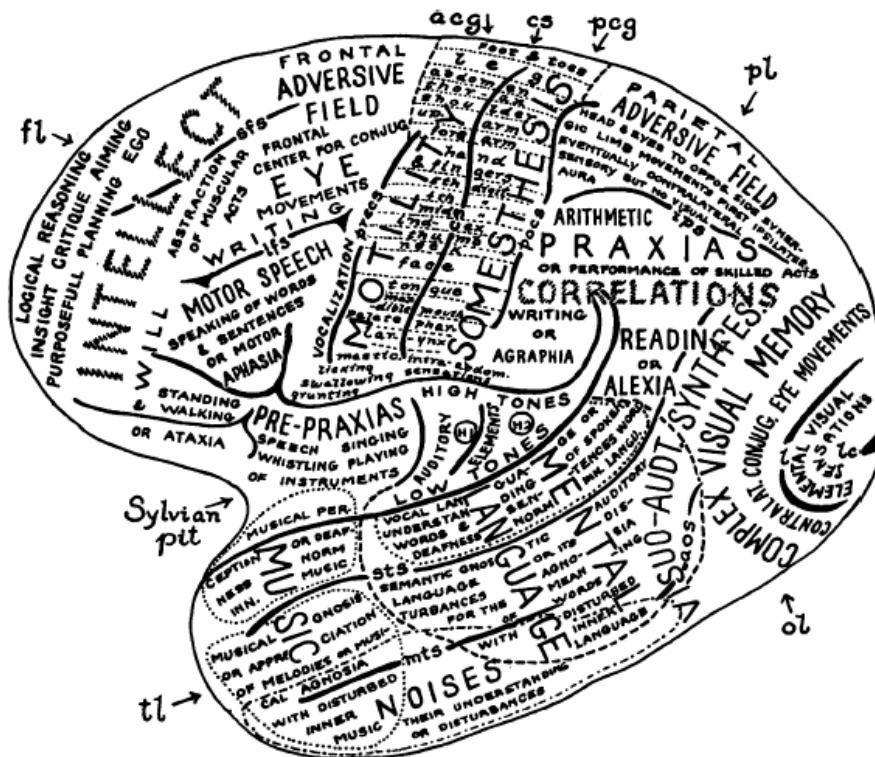


Figure1.1: This figure schematically summarizes the state of knowledge of localization of human functional brain in 1957.

The answers to these questions are based upon two techniques: study of brains with lesions (caused by stroke, disease or traumatic wounds) and direct electrical stimulation of the cortex of the patient undergoing brain surgery. Since then many new

technologies have been developed and improved upon in last half century. Some of these techniques are described briefly as follows.

1.1 Brain Mapping Techniques

1.1.1 Lesions

Historically the oldest data alluding to the localization of human brain functions came from people with lesions caused by disease or trauma. In the Russo-Japan war of 1905 rifles were used which for the first time fired bullets that moved fast enough to enter and exit the brains of victims cleanly, often leaving well defined scotomas in their visual field, but no other neurological damage. Despite the complications of cortical folds and individual differences Dr. Inouye reconstructed the retinotopic maps in the visual cortex that followed the spatial regularity of visual world. [106, 107]

1.1.2 Direct stimulation of exposed cortical tissue

In the middle of the 20th century, direct stimulation of cortical region was used to map function. This work was the basis for much of the information displayed in figure 1. This technique is still widely used. [108]

1.1.3 Intra-cranial stimulation and recording

This subdural and/or intra-cortical technique places one or more strips of recording electrodes directly into patient's brain. The electrical signals gathered from these electrodes show activated areas of brain for certain stimulus. [1, 108]

1.1.4 Temporary lesions and stimulation via TMS and TES

Transcranial magnetic stimulation (TMS) and Transcranial electric stimulation (TES) are semi-invasive techniques. In TMS a coil is placed near the subjects head and a very brief but very large pulse is applied which creates a very strong transient magnetic

field. Transient magnetic field induces current flow in nearby neurons impairing them temporarily. In TES spatially separated electrodes are placed on the head and current is run between electrodes. The electrode placements cause some current to flow through the brain which temporarily disrupts activity within that portion of the brain. This strategy is used to show that that brain region is necessary for certain a function or behavior.

These techniques are invasive and can hardly be used ethically (including mapping animal brains) for brain mapping. More recent brain mapping techniques are non-invasive, give exceptional spatial and temporal resolution of activation maps and mitigate the ethical issues involved with delineating brain function.

1.1.5 Electromagnetic recording

Two technologies used for non-invasively recording the electrical activity of the human brain are electroencephalography (EEG) and magnetoencephalography (MEG). Both are exceptionally safe and capable of millisecond temporal resolution. They can measure electrical activity continuously to obtain event-related potential (ERP of EEG) or event related field (ERF of MEG) responses to fixed type of stimulus. Due to this robust response these techniques are widely used in brain mapping and cognitive neuroscience. However, both techniques are limited in terms of volumetric spatial resolution because they can only measure signals external of the head. [1,109]

1.1.6 Hemodynamic response to neural activity

Another strategy used to investigate brain function is based on more indirect measures: the change in blood flow and change in venous oxygenation level that follow neural activity. Collectively these are referred to as hemodynamic changes, and they are the source of virtually all volumetric functional brain imaging data. There are two major

technologies based upon hemodynamic response namely Positron Emission tomography (PET) and functional Magnetic Resonance Imaging (fMRI).

PET is based on radioactive atoms that release positrons. Each positron annihilates a nearby electron which results in a release of a pair of oppositely directed high energy gamma rays. The coincident detection of this gamma ray pair forms the basis for PET. PET has been an important tool in the mapping of all aspects of brain function physiology, not just neural activation. Glucose metabolism, protein synthesis, dopamine receptor detection, and DNA replication are just a few biological functions studied using PET. Blood flow, blood volume and oxygen utilization have been studied quantitatively using PET.

Functional MRI (fMRI) refers, in present context, to the detection of hemodynamic changes associated with neural activity using the technology of MRI. fMRI is sensitive to the oxygenation status of hemoglobin and therefore produces images that reflect changes in cerebral blood flow and volume. With enhanced synaptic and neuronal activity there is a compensatory increase in blood flow and blood volume that can be measured and attributed to neuronal activity. This blood has a high concentration of oxygenated hemoglobin causing a positive, Blood Oxygenation Level Dependent (BOLD) change in MR signal [2, 3]. Since fMRI data analysis is topic of this dissertation detailed mechanism and application is covered in later chapter. Overall the brain mapping techniques can be summarized as shown in figure 1.2 and comparison of different techniques is shown in Table1.1.

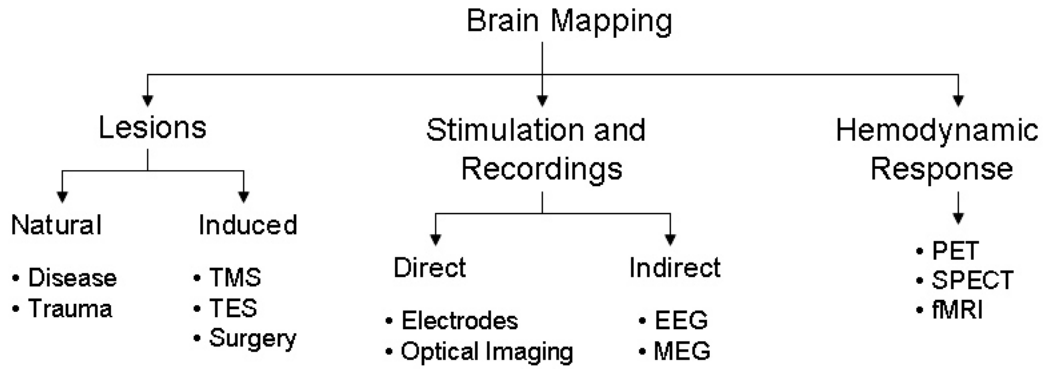


Figure 1.2: Classification of Brain mapping techniques

Technique	Resolution	Advantage	Disadvantage
SPET	10 mm	Low Cost.	Radiation expositor Limited spatial and temporal resolution
PET	5 mm	Sensitive, Metabolic Studies, Receptor mapping, Better spatial resolution the than SPECT.	Radiation expositor Very Expensive
EEG	Poor	Very low cost, Good temporal resolution, Non-invasive.	Not an imaging technique Not good for deep structures
MEG	5 mm	High temporal resolution, Non-invasive.	Very Expensive Not an imaging technique Not good for deep structures
fMRI	0.5 - 1mm	High spatial resolution Good temporal resolution No radiation Non-invasive	Very Expensive, Motion artifact, Correlational, Limited to activation studies.

Table 1.1 Comparison of Brain Mapping Technique.

1.2 fMRI data Analysis

The changes in MR signal induced by changes blood flow, volume, and oxygenation are the basis for all fMRI methods. There are three main functional imaging techniques.

- Blood Oxygen Level Dependent (BOLD) Technique
- Cerebral Blood Flow (CBF) Technique
- Cerebral Blood Volume (CBV) Technique

The BOLD effect is the basis for most of the current fMRI studies to map brain activation patterns. The goal of BOLD fMRI studies is to map patterns of local changes in magnetic resonance (MR) signal in the brain as an indicator of neural activity associated with particular stimuli. The prototypical fMRI experiment has blocks of control and stimulus periods while the series of dynamic images are collected. The time course for each image voxel is analyzed to test its significance relative to the control/stimulation periods. This fMRI strategy is a critical component of brain mapping. Many creative statistical methods have been proposed and there has been considerable debate about the ranking of each approach. Given the flexibility of fMRI and range of experiments possible it seems likely that a number of different statistical processing approaches can be applied to yield useful data. In this work a quantitative fMRI data analysis strategy was successfully developed and optimized for the rat brain.

1.3 Outline

For the analysis of fMRI data it is important to understand physics of MRI. Chapter two describes quantum mechanic explanation of magnetic resonance imaging (MRI) which includes Larmor Equation, T1 and T2 relaxation time, RF field and different pulse sequences. The chapter is concluded with description of fMRI data and its characteristics.

Development of a digital Rat Brain Atlas was the corner stone of this work. Published computerized Rat anatomy atlases, like Swanson's Rat Brain Atlas, had some major flaws to be converted to a digital Atlas. Chapter three focuses on the system developed to remove these flaws automatically that creates numerically robust digital atlas.

Chapter four deals with registration, segmentation and statistical analysis, the main steps in fMRI data analysis strategy. The chapter starts with different coordinate systems and transformation among them. This is followed by mathematical formulation of different registration techniques used in fMRI module. Further the brain mapping algorithm is described and chapter is concluded by detailed formulation of statistical analysis techniques.

Chapter five focuses on software implementation of the strategy. Chapter six demonstrates the power of the system developed by analyzing olfactory response by rat for four different odorants.

2: MRI and fMRI

Functional brain mapping with magnetic resonance imaging (MRI) is a rapidly growing field that has emerged within the past several years. Functional MRI (fMRI) is the use of MRI equipment to detect regional changes of cerebral metabolism or in blood flow, volume or oxygenation in response to task activation. The most popular technique utilizes blood oxygenation level dependent (BOLD) contrast, which is based on the differing magnetic properties of oxygenated (diamagnetic) and deoxygenated (paramagnetic) blood. These magnetic susceptibility differences lead to small, but detectable changes in susceptibility-weighted MR image intensity [5, 75, 76]. To understand the fMRI method, investigators should be familiar with the physical principles of magnetic resonance that determine its signal characteristics, and through which it is possible to form images. This chapter is dedicated to principles of Nuclear Magnetic Resonance (NMR). The acronyms NMR and MRI are used interchangeably. Many of the illustrations and MRI physics explanation is based on “Basic Principles of MR Imaging” written by Keller. [10]

2.1 Overview of MR imaging

- The subject is placed into a strong, homogeneous magnetic field. Various atomic nuclei, particularly the proton nucleus of the hydrogen atom (from here, we will consider only these protons), align themselves with this field and reach equilibrium. The subject is thereby "magnetized."
- The proton nuclei precess about the applied field at a characteristic frequency, but at a random phase (or orientation) with respect to one another.

- Application of a brief radio frequency (RF) electromagnetic pulse disturbs the equilibrium and introduces transient phase coherence to the nuclear magnetization that can, in turn, be detected as a radio signal and formed into an image.

2.2 Spin in Magnetic Field

The vertebrate body is primarily fat and water. Fat and water have many hydrogen atoms which make the body approximately 63% hydrogen atoms. Hydrogen nuclei have an NMR signal [76]. For these reasons magnetic resonance imaging primarily images the NMR signal from the hydrogen nuclei. In quantum mechanics spin is represented by a magnetic spin quantum number. Spin can be visualized as a rotating motion of the nucleus about its own axis. As atomic nuclei are charged, the spinning motion causes a magnetic moment in the direction of the spin axis. This phenomenon is shown in Figure 2.1. The strength of the magnetic moment is a property of the type of nucleus.

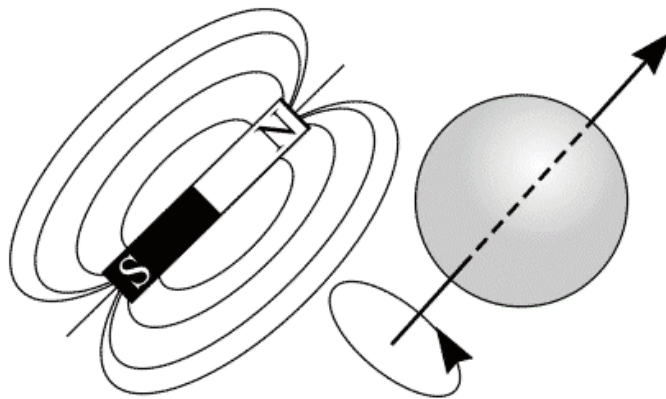


Figure 2.1: A charged, spinning nucleus creates a magnetic moment which acts like a bar magnet
[10]

Consider a collection of ^1H nuclei (spinning protons) as in Figure 2.2(a). In the absence of an externally applied magnetic field, the magnetic moments have random

orientations. However, if an externally supplied magnetic field B_0 is imposed, the magnetic moments have a tendency to align with the external field (Figure 2.2 (b)).

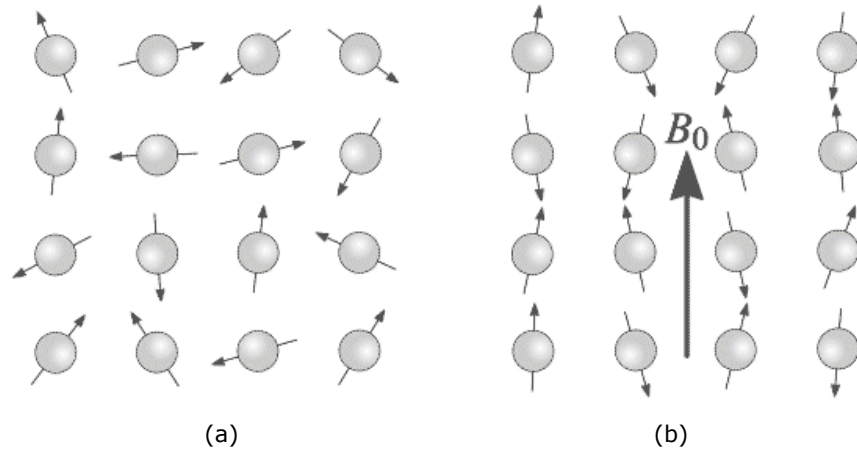


Figure 2.2 : (a) A collection of 1H nuclei (spinning protons) in the absence of an externally applied magnetic field. The magnetic moments have random orientations. (b) An external magnetic field B_0 is applied which causes the nuclei to align themselves in one of two orientations with respect to B_0 (denoted parallel and anti-parallel).[10]

The magnetic moments or spins are constrained to adopt one of two orientations when placed in external magnetic field B_0 , denoted parallel and anti-parallel. The angles subtended by these orientations and the direction of B_0 are labeled θ , respectively in Figure 2.3(a). The spin axes are not exactly aligned with B_0 , they precess around B_0 with a characteristic frequency as shown in Figure 2.3(b). This is analogous to the motion of a spinning top precessing in the earth's gravitational field.

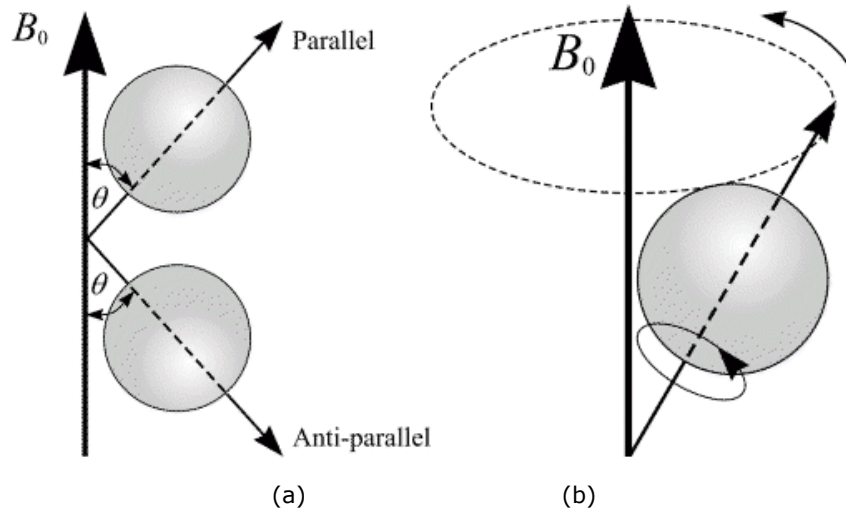


Figure 2.3: (a) In the presence of an externally applied magnetic field, B_0 , nuclei are constrained to adopt one of two orientations with respect to B_0 . As the nuclei possess spin, these orientations are not exactly at 0 and 180 degrees to B_0 . (b) A magnetic moment precessing around B_0 . Its path describes the surface of a cone.[10]

The Larmor equation expresses the relationship between the strength of a magnetic field, B_0 , and the precessional frequency, F , of an individual spin.

$$\gamma B_0 = F$$

The proportionality constant γ is the value of the gyromagnetic ratio of the nucleus. The precessional frequency, F , is also known as the Larmor frequency. For a hydrogen nucleus, the gyromagnetic ratio γ is 42.57 MHz/T where T is Tesla.

2.3 Radio Frequency field and MR signal

For a collection of ^1H nuclei, let the number of spins adopting the parallel and anti-parallel states be P_1 and P_2 respectively, with corresponding energy levels E_1 and E_2 . E_2 is greater than E_1 causing P_1 to be greater than P_2 . An obvious question is why do spins adopt the higher energy anti-parallel state? The answer is that spins of P_1 may move to P_2 if the exact amount of energy, $\Delta E = E_2 - E_1$ is supplied to the system. If the

temperature of the system were absolute zero, all spins would adopt the parallel orientation [10, 77]. Thermal energy will cause P_2 to be populated. At room temperature in a 1.5 Tesla magnetic field, there will typically be a population ratio $P_2:P_1$ equal to 100,000:100,006.

At any given instant, the magnetic moments of a collection of ^1H nuclei can be represented as vectors, as shown in Figure 2.4. Every vector can be described by its components perpendicular to and parallel to B_0 . For a large enough number of spins distributed on the surface of the cone, individual components perpendicular to B_0 cancel, leaving only components in the direction parallel to B_0 . The small population difference results in net magnetization M in the direction of the B_0 field.

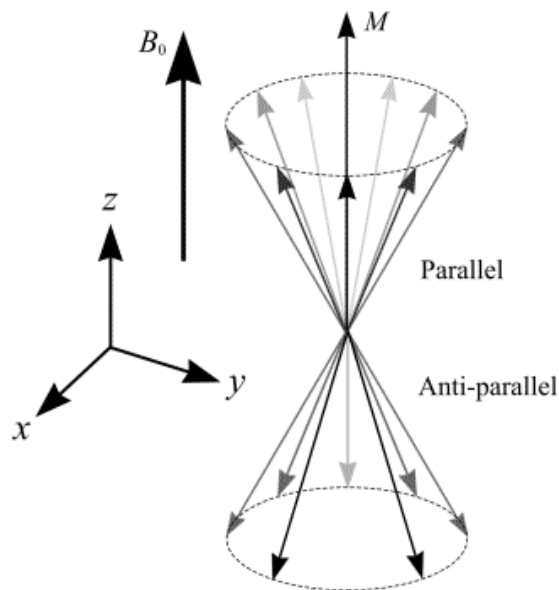


Figure 2.4: A collection of spins at any given instant in an external magnetic field, B_0 . A small net magnetisation, M , is detectable in the direction of B_0 . [10]

Suppose the direction of B_0 is aligned with the z-axis of Euclidean 3-space. The plane perpendicular to B_0 contains the x and y-axes. In order to detect a signal from ^1H nuclei, radio frequency (RF) energy must be applied. RF energy at the Larmor frequency

induces transfer between two energy levels whereas RF energy at other frequencies has no effect. RF energy, like all electromagnetic radiation, has electric and magnetic field components. Suppose the magnetic field component is represented by B_1 and lies in the x-y plane. The x-y components of M will be made coherent by the B_1 field giving a net x-y component to M and hence effectively causes M to tilt from the z direction into the x-y plane. This phenomenon is described further in top left of Figure 2.5.

The angle through which M has rotated away from the z-axis is known as the flip angle. The strength and duration of B_1 determine the amount of energy available to achieve spin transitions between parallel and anti-parallel states. Thus, the flip angle is proportional to the strength and duration of B_1 . After pulses of 90 degrees and 270 degrees, M has no z component and the population ratio $P_2:P_1$ is exactly one. A pulse of 180 degrees rotates M into a position directly opposite to B_0 , with greater numbers of spins adopting anti-parallel (rather than parallel) states. If the B_1 field is applied indefinitely, M tilts away from the z-axis, through the x-y plane towards the negative z direction, and finally back towards the x-y plane and z-axis (where the process begins again).

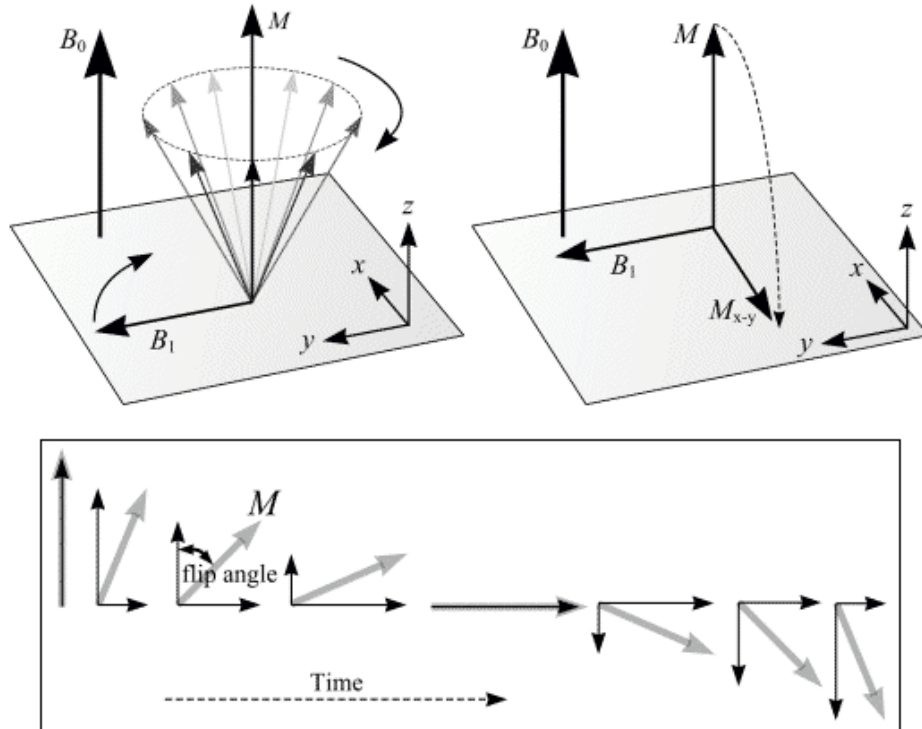


Figure 2.5: (top) The effect of RF radiation on the net magnetization M is to produce a second magnetic field M_{x-y} . M is tilted from its original longitudinal z-axis orientation, along the direction of the external magnetic field B_0 , into the transverse x-y plane. (bottom) An illustration of flip angle, which is the angle through which M has rotated away from the z-axis. [10]

Figure 2.6 (a) shows the situation after an RF pulse is applied that causes the net magnetization vector M to flip by 90 degrees. M lies in the x-y plane and begins to precess about the B_0 axis. M will induce an electromotive force in a receiver coil according to Faraday's law of magnetic induction. This is the principle of NMR signal detection. It is from this received RF signal that an MR image can be constructed. Figure 2.6(b) shows a graph of the voltage or signal induced in a receiver coil versus time. Such a graph, or waveform, is termed as free induction decay (FID). The magnitude of the generated signal depends on the number of nuclei contributing to produce the transverse magnetization and on the relaxation times.

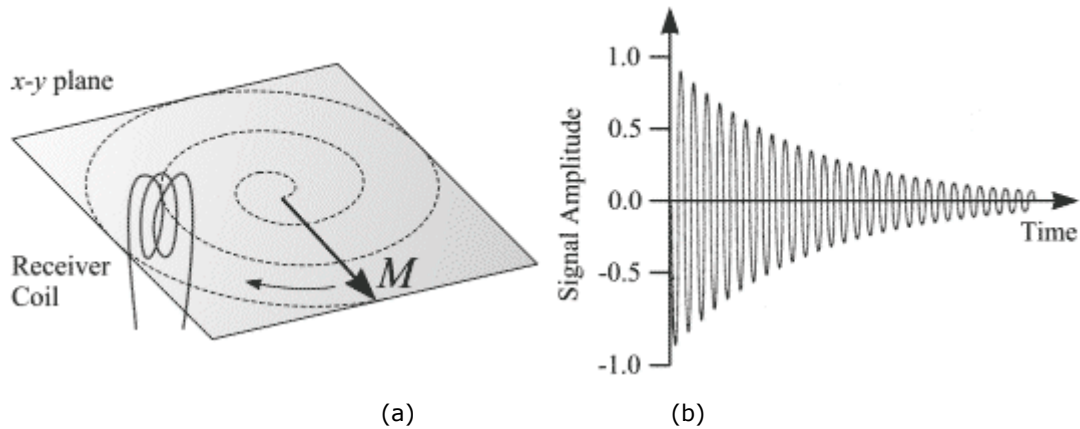


Figure 2.6: (a) After a 90 degrees RF pulse, M lies in the x-y plane and rotates about the z-axis. The component of M in the x-y plane decays over time. An alternating current, shown in Figure (b), is induced in the receiver coil. [10]

2.4 Relaxation Processes

The return of M to its equilibrium state (the direction of the z-axis) is known as relaxation. There are three factors that influence the recovery of M : magnetic field inhomogeneity, longitudinal T_1 relaxation and transverse T_2 relaxation. Magnetic field inhomogeneity refers to the spins at different spatial locations do not experience the same B_0 field. T_1 relaxation (also known as spin-lattice relaxation) is the realignment of spins (or recovery of M) with the external magnetic field B_0 (z-axis). T_2 relaxation (also known as T_2 decay, transverse relaxation or spin-spin relaxation) is the decrease in the x-y component of magnetization.

2.4.1 T_1 relaxation

Following termination of an RF pulse, nuclei will dissipate their excess energy as heat to the surrounding environment (or lattice) and revert to their equilibrium position. Realignment of the nuclei along B_0 , through a process known as recovery, leads to a gradual increase in the longitudinal magnetization. The time taken for a nucleus to relax

back to its equilibrium state depends on the rate that excess energy is dissipated to the lattice. Let M_{0-long} be the amount of magnetization parallel with B_0 before an RF pulse is applied. M_{long} is the z component of M at time t , following a 90 degree pulse at time $t = 0$. It can be shown that the process of equilibrium restoration is described by the equation

$$M_{long} = M_{0-long} \cdot \left(1 - e^{-t/T_1}\right)$$

where T_1 is the time taken for approximately 63% of the longitudinal magnetization to be restored following a 90 degree pulse.

2.4.2 T_2 relaxation

While nuclei dissipate their excess energy to the lattice following an RF pulse, the magnetic moments interact with each other causing a decrease in transverse magnetization. This effect is similar to that produced by magnet inhomogeneity, but on a smaller scale. The decrease in transverse magnetization (which does not involve necessarily the emission of energy) is called decay. The rate of decay is governed by a time constant, T_{2^*} , that is the time it takes for the transverse magnetization to decay to 37% of its original magnitude. T_{2^*} characterizes dephasing due to both B_0 inhomogeneity and transverse relaxation. Let $M_{0-trans}$ be the amount of transverse magnetization (M_{x-y}) immediately following an RF pulse. Let M_{trans} be the amount of transverse magnetization at time t , following a 90 degree pulse at time $t = 0$. It can be shown that

$$M_{trans} = M_{0-trans} \cdot e^{-t/T_{2^*}}$$

The echo-to-echo amplitudes decay as function of T_2 rather than T_{2^*} . In order to obtain signal with a T_2 dependence rather than a T_{2^*} dependence, a pulse sequence known as the spin-echo has been devised which reduces the effect of B_0 inhomogeneity on M_{x-y} . A

pulse sequence is an appropriate combination of one or more RF pulses and gradients (see next section) with intervening periods of recovery. A pulse sequence consists of several components, of which the main ones are the repetition time (TR), the echo time (TE), flip angle, the number of excitations (NEX), bandwidth and acquisition matrix.

Figures 2.7 and 2.8 show pictorially how the spin echo pulse sequence works. Figure 2.7 is a graph of pulsed RF and received signal verses time, while Figure 2.8 is a phase diagram of the magnetization vector M . After a 90 degree pulse, a signal is formed which decays with T_2^* characteristics. This is illustrated by the top right ellipse in Figure 2.8 which shows three spins at different phases due to their different precessional frequencies. The fastest spin is labeled f and the slowest s . At time $TE/2$, a 180 degree pulse is applied to the sample (see bottom left ellipse in Figure 2.8) which causes the three spins to invert. After inversion, the order of the spins is reversed with the fastest lagging behind the others. At time TE, the spins become coherent again so that a signal (known as the spin echo) is produced.

If a subsequent 180 degree pulse is applied at time $TE/2$ after the peak signal of the first spin echo, then a second spin echo signal will form at time TE after the first spin echo. The peak signal amplitude of each spin echo is reduced from its previous peak amplitude due to T_2 dephasing which cannot be rephased by the 180 degree pulses. Figure 2.9 shows how the signal from a spin echo sequence decays over time. A line drawn through the peak amplitude of a large number of spin echoes describes the T_2 decay, while individual spin echoes exhibit T_2^* decay.

Signal strength decays with time to varying degrees depending on the different materials in the sample. Different organs have different T_1 s and T_2 s and hence different

rates of decay of signal. When imaging anatomy, some degree of control of the contrast of different organs or parts of organs is possible by varying TR and TE. The intensity of a spin echo signal, I , can be approximated as

$$I = N(H) \cdot f(V) \cdot (1 - e^{-TR/T_{R1}}) \cdot e^{-TE/T_2}$$

where $N(H)$ is the proton density and $f(V)$ is a function of flow.

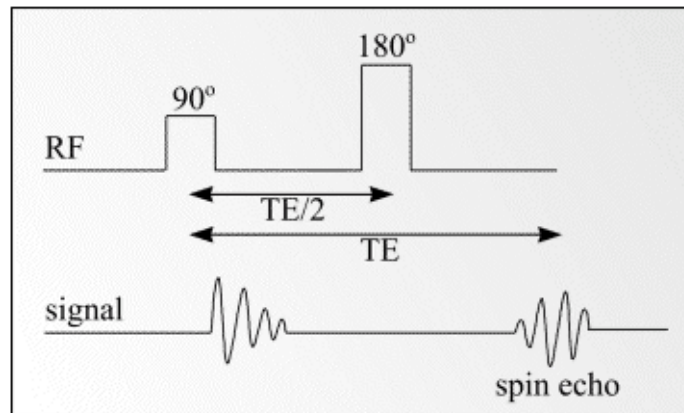


Figure 2.7: Formation of a spin echo at time TE after a 90 degree pulse.

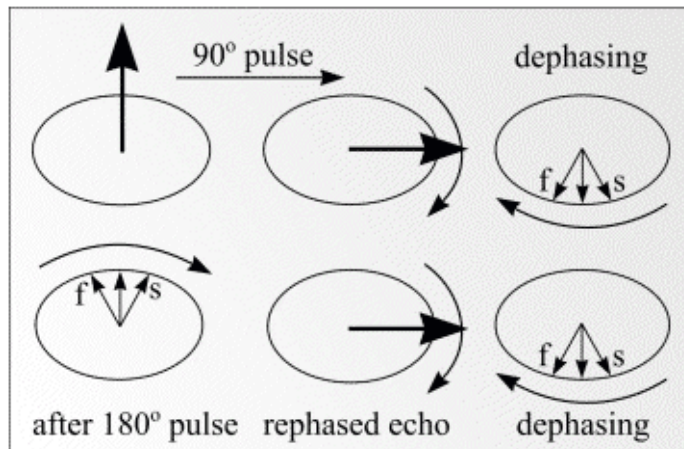


Figure 2.8: Dephasing of the magnetization vector by T_2^* and rephasing by a 180 degree pulse to form a spin echo.

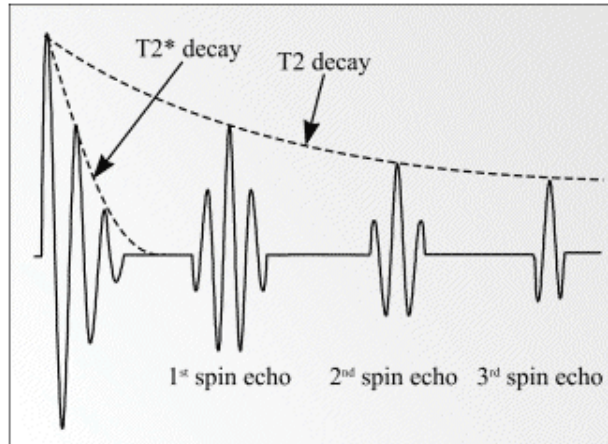


Figure 2.9: Decay of signal with time in a spin echo sequence.

2.5 Magnetic Resonance Imaging

The actual location within the sample from which the RF signal was emitted is determined by superimposing magnetic field gradients on the magnet generating the otherwise homogeneous external magnetic field B_0 . For example, a magnetic field gradient can be superimposed by placing two coils of wire (wound in opposite directions) around the B_0 field with longitudinal axis orientated in the z direction and then by passing direct current through the coils. The magnetic field from the coil pair adds to the B_0 field, with the result that one end of the magnet has a higher field strength than the other. According to the Larmor equation, the magnetic field gradient causes identical nuclei to precess at different Larmor frequencies. The frequency deviation is proportional to the distance of the nuclei from the centre of the gradient coil and the current flowing through the coil.

2.5.1 Slice Selection

With an axial gradient coil activated, a single frequency RF pulse is applied to the whole sample. Only a narrow plane perpendicular to the longitudinal axis at the centre of

the sample absorbs the RF energy. Elsewhere the coupled gradient and B_0 frequency is mismatched to the RF frequency and resonance will not occur. This technique allows a slice, with thickness determined by the magnetic field gradient strength, to be selected from a sample.

2.5.2 Frequency Encoding

Three magnetic field gradients, placed orthogonally to one another inside the bore of the magnet, are required to encode information in three dimensions. With a slice selected and excited as described in the previous paragraph, current is switched to one of the two remaining gradient coils (referred to as the frequency encoding gradient). This has the effect of spatially encoding the excited slice along one axis, so that columns of spins perpendicular to the axis precess at slightly different Larmor frequencies. For a homogeneous sample, the intensity of the signal at each frequency is proportional to the number of protons in the corresponding column.

The frequency encoding gradient is activated just before the receiver is gated on and remains on while the signal is sampled or read out. For this reason the frequency encoding gradient is also known as the readout gradient. The resulting FID is a graph of signal (formed from the interference pattern of the different frequencies) induced in the receiver verses time. If the FID is subjected to Fourier transform, a conventional spectrum in which signal amplitude is plotted as a function of frequency can be obtained. Thus, a graph of signal verses frequency is obtained which corresponds to a series of lines or views representing columns of spins in the slice. Figure 2.10 shows two simple FIDs and their Fourier transforms.

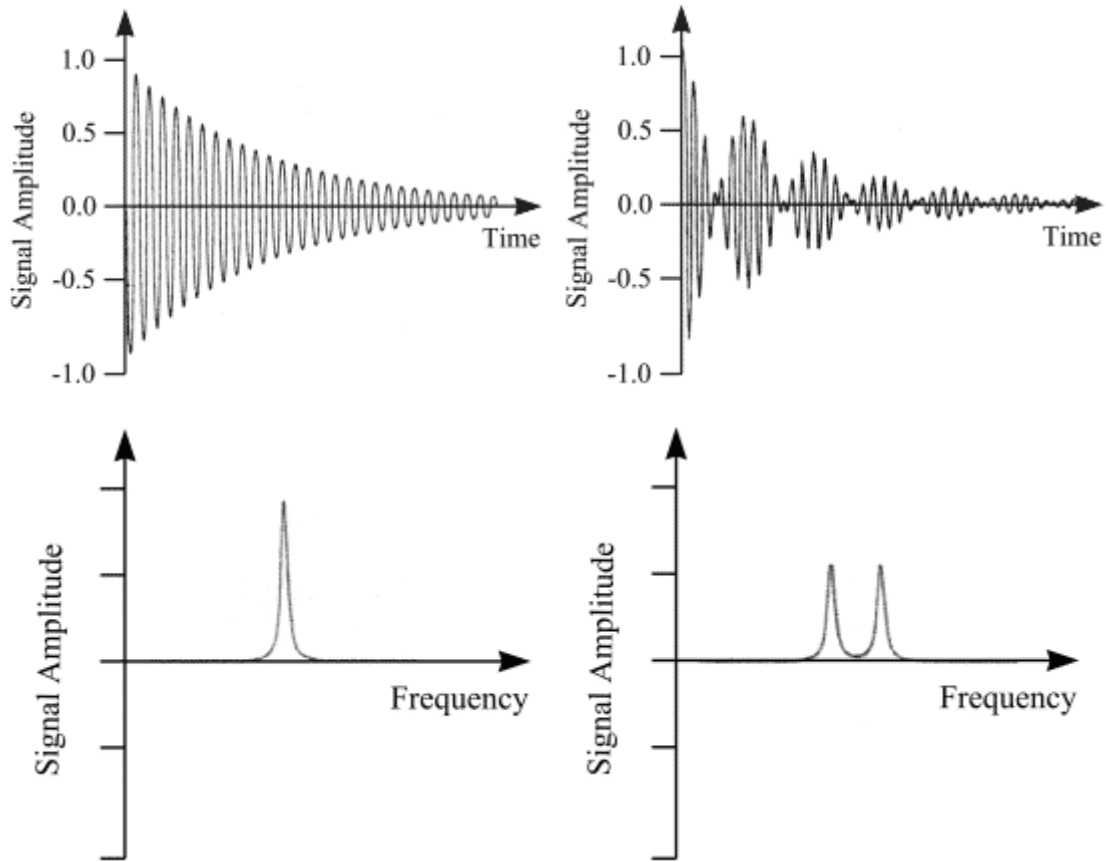


Figure 2.10: Two FIDs and their Fourier transforms.

2.5.3 Phase Encoding

Suppose a slice through a homogeneous sample has been selected and excited as described in Slice Selection section, and then frequency encoded according to the previous section. After a short time, the phase of the spins at one end of the gradient leads those at the other end because they are precessing faster. If the frequency encoding gradient is switched off, spins precess (once more) at the same angular velocity but with a retained phase difference. This phenomenon is known as phase memory.

A phase encoding gradient is applied orthogonally to the other two gradients after slice selection and excitation, but before frequency encoding. The phase encoding gradient does not change the frequency of the received signal because it is not on during signal

acquisition. It serves as a phase memory, remembering relative phase throughout the slice.

To construct a 256 x 256 pixels image a pulse sequence is repeated 256 times with only the phase encoding gradient changing. The change occurs in a stepwise fashion, with field strength decreasing until it reaches zero, then increasing in the opposite direction until it reaches its original amplitude. At the end of the scan, 256 lines (one for each phase encoding step) comprising 256 samples of frequency are produced. A Fourier transformation allows phase information to be extracted so that a pixel (x, y) in the slice can be assigned the intensity of signal which has the correct phase and frequency corresponding to the appropriate volume element. The signal intensity is then converted to a grey scale to form an image.

2.6 MRI Sequences

MRI signal intensity depends on many parameters, including proton density, T_1 and T_2 relaxation times. Different pathologies can be selected or illuminated by the proper choice of pulse sequence parameters. Repetition time (TR) is the time between two consecutive RF pulses measured in milliseconds. For a given type of nucleus in a given environment, TR determines the amount of T_1 relaxation. The longer the TR , the more the longitudinal magnetization is recovered. Tissues with short T_1 have greater signal intensity than tissues with a longer T_1 at a given TR . A long TR allows more magnetization to recover and thus reduces differences in the T_1 contribution in the image contrast. Echo time (TE) is the time from the application of an RF pulse to the measurement of the MR signal. TE determines how much decay of the transverse magnetization is allowed to occur before the signal is read. It therefore controls the

amount of T_2 relaxation. The application of RF pulses at different TR s and the receiving of signals at different TE s produces variation in contrast in MR images. Two common MRI sequences are described that vary the TR , TE sequences for delineating different tissues.

2.6.1 Spin Echo Pulse Sequence

The spin echo (SE) sequence is the most commonly used pulse sequence in clinical imaging. The sequence comprises two radiofrequency pulses - the 90 degree pulse that creates the detectable magnetization and the 180 degree pulse that refocuses it at TE . The selection of TE and TR determines resulting image contrast. In T_1 -weighted images, tissues that have short T_1 relaxation times (such as adipose tissue) present a bright signal. Tissues with long T_1 relaxation times (such as cysts, cerebrospinal fluid and edema) show as dark signal. In T_2 -weighted images, tissues that have long T_2 relaxation times (such as fluids) appear bright.

In cerebral tissue, differences in T_1 relaxation times between white and grey matter permit the differentiation of these tissues on heavily T_1 -weighted images. Proton density-weighted images also allow distinction of white and grey matter, with tissue signal intensities mirroring those obtained on T_2 -weighted images. In general, T_1 -weighted images provide excellent anatomic detail, while T_2 -weighted images are often superior for detecting pathology.

2.6.2 Gradient Recalled Echo Pulse Sequences

Gradient recalled echo (GRE) sequences, which are significantly faster than SE sequences, differ from SE sequences in that there is no 180 degree refocusing RF pulse.

In addition, the single RF pulse in a GRE sequence is usually switched on for less time than the 90 degree pulse used in SE sequences. The scan time can be reduced by using a shorter TR, but this is at the expense of the signal to noise ratio (SNR) which drops due to magnetic susceptibility between tissues. At the interface of bone and tissue or air and tissue, there is an apparent loss of signal that is heightened as TE is increased. Therefore it is usually inappropriate to acquire T_2 -weighted images with the use of GRE sequences. Nevertheless, GRE sequences are widely used for obtaining T_1 -weighted images for a large number of slices or a volume of tissue in order to keep scanning times to a minimum. GRE sequences are often used to acquire T_1 -weighted 3D volume data that can be reformatted to display image sections in any plane. However, the reformatted data will not have the same in-plane resolution as the original images unless the voxel dimensions are the same in all three dimensions.

2.7 Functional MRI (fMRI)

The physiology of neuronal activity involves many complex processes. It was established, as long ago as 1890 [11] that physiological functions in the brain correspond to regional brain activity. Magnetic resonance has the capability to measure parameters related to several of these physiological functions, including changes in phosphorus metabolism and metabolic byproducts, blood flow, blood volume, and blood oxygenation. The most common current technique uses blood oxygen level dependent (BOLD) contrast [2,9]. This technique is based on the magnetic susceptibility of hemoglobin (Hb). Deoxygenated Hb is paramagnetic, while fully oxygenated Hb is diamagnetic. The presence of the paramagnetic deoxy-Hb distorts the static magnetic field. Spins in this non-uniform magnetic field precess at different frequencies causing more rapid phase dispersal and decay of the NMR signal. Therefore, changes in blood

oxygenation can cause changes in the MR decay parameter, T_2^* , leading to changes in image intensity in T_2^* -weighted images. Table 2.1, below summarizes the changes in physiology and MR parameters that enable MRI to detect signal changes based on blood oxygenation [5].

Blood Flow	↑↑↑
O ₂ Utilization	↑
Blood O ₂ Level	↑↑
Deoxy-Hemoglobin Level	↓↓
Distortions to B ₀	↓↓
Phase dispersal of M	↓↓
Effective Decay Rate (1/T ₂ [*])	↓↓
T ₂ [*] -weighted Signal	↑↑

Table 2.1 Physiological and MR parameter changes due to increased neuronal activity.

The relatively straight forward story is, unfortunately, oversimplified. To give some idea of the complexity of the physiological and physical response of this fMRI signal, refer to Figure 2.11, below (adapted from Springer, et al. [7,5]). In this figure, the connecting arrows describe the effect of one parameter on another. Positive/negative arrows indicate positive/negative correlations between the parameters. For example, an increase in blood flow with no other effects would lead to an increase in blood oxygenation while an increase in oxygen metabolism would lead to decrease in blood oxygenation. The rightmost pathway through the diagram is the dominant pathway of physiological and physical effects leading the positive change in BOLD signal in fMRI. There are pathways that have a net negative effect on the signal – as described above, the

increase in oxygen metabolism leads to decrease in blood oxygenation, which reduces the fMRI signal. Increases in blood volume will increase the amount of deoxyhemoglobin which makes the magnetic field less uniform and also reduced the fMRI signal. The positive signal changes seen in fMRI studies rely on the dominance of the increase in blood flow over changes in blood volume and oxygen utilization. Further adding to the complexity of the MR signal is an interaction between the observed MRI signal and physical properties such as vessel diameter, orientation, hematocrit and blood volume fraction.

In a typical functional MRI experiment, two or more behavioral conditions are applied and the images compared to delineate the regions of the brain that are different between the two conditions. Since the deoxy-Hb effect is quite small relative to the noise of the system it is typically not visible in a single experimental condition or time slice, but can be identified after statistical tests (e.g. a pixel-by-pixel t-test comparison between the conditions).

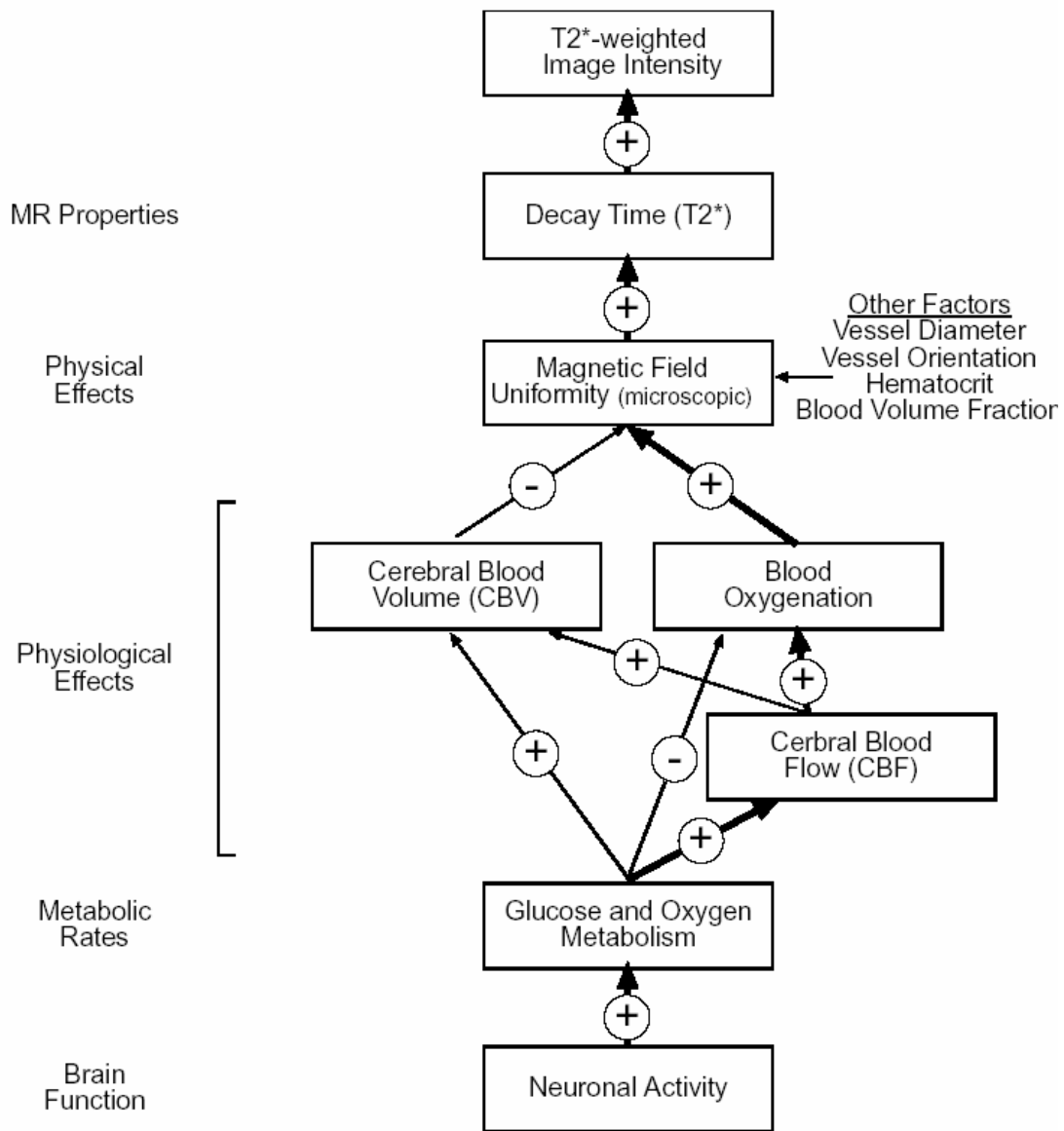


Figure 2.11: Schematic of interactions in the formation of BOLD signal. Positive/negative arrow indicates positive/negative correlations between the parameters. The right most pathway is the most significant effect in most BOLD fMRI.

2.7.1 Hemodynamics

It is important to consider the temporal dynamics of the activation response when designing experiments and processing strategies. The MRI response is delayed and relatively slow compared to actual brain activity. There are a number of factors

associated with the temporal response of the deoxy-Hb effect. It is commonly reported to take 6-9 s to reach peak and 8-20 seconds to return to base line intensity. Negative responses following a block of activity are commonly seen and while not widely replicated, some groups have reported an initial negative response 500-2500 ms after activity begins. Figure 2.12 contains a drawing of a typical temporal response to neuronal activity [5]. This temporal response must be considered when designing appropriate processing strategies, assigning images to particular behavioral states or transition regions, and detecting short duration states. This is also important for experimental design.

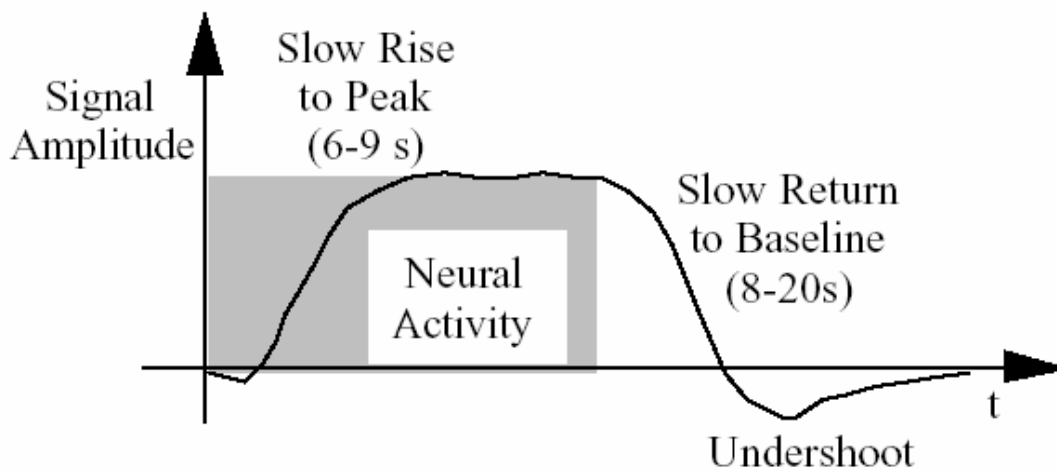


Figure 2.12: Typical time course for activation related signal in T2 waited (BOLD) functional MRI.

2.7.2 Event-Related Functional MRI

A recent development in functional MRI is the imaging of the responses to individual trials, known as event-related fMRI. Above figure (Fig. 2.12) describes the

response to a block of stimulation. Because the hemodynamic response is rather slow, the responses all blur together to exhibit roughly a constant amplitude in the central portion of the block. In event-related fMRI, the responses to individual trials are examined. This is done by using an experimental design that allows these responses to be extracted. For example, the inter-trial interval (ITI) can be extended to allow the response to develop and dissipate before the next trial is given (this is usually 10-12 seconds, but can be longer if the task being executed in the trial is rather long). Individual responses can also be extracted by randomly mixing the trial types or randomizing the ITI, but allowing the responses to overlap. When this is done, fluctuations in the signal intensity result from the summation of responses of differing sizes to the mixed trial types or from the summation of the responses to randomly timed trials. The estimation of the response location, size and shape in event-related fMRI is presently an active area for research.

2.7.3 Statistical Testing

Critical steps in any functional MRI study are data analysis and result compilation. In this work a quantitative analysis strategy was successfully developed and optimized for the rat brain. Therein, each subject is registered to a complete volume-segmented atlas. All registered images are then segmented based on atlas. Statistical tests are performed on each subject within their original coordinate system. A statistical composite is created for each ROI by summing up individual analysis within ROIs. The detailed description of the strategy and algorithm is described in Chapter 4.

3: The Rat Brain Atlas

A starting point to map any functional area is to have a template or reference brain anatomical map. The most widely used Rat brain atlas is Swanson's rat brain atlas (1998) [12], however, other rat atlases exist as well.

- Paxinos and Watson, 1986
- DeGroot, 1959
- König and Klippel, 1963
- Wüscher et al, 1965
- Albe-Fessard et al, 1966 and
- Pellegrino, 1979

3.1 Swanson Rat Brain Atlas

The core of Swanson's atlas is 73 drawings prepared from transverse Nissl-stained sections through the adult male rat brain. These drawings were created from photomicrographs of histological sections of a 315 gram adult male Sprague-Dawley rat brain [12].

The location of these 73 slices throughout the brain is illustrated in Figure 3.1. Since brain is a very heterogeneous structure, some levels require fewer sections than others for adequate illustration. Each drawing contains a wealthy amount of information regarding the neuroanatomical areas of the brain. Each region which has been identified is also given a label which is the abbreviation of the regions name. There are a total of 1277 labels in the atlas, meaning that one can distinguish 1277 different neuroanatomical

regions. These labels will serve as the seed points for loop detection in this work. Figure 3.2 shows a small part of section 5 of the brain with the labels.

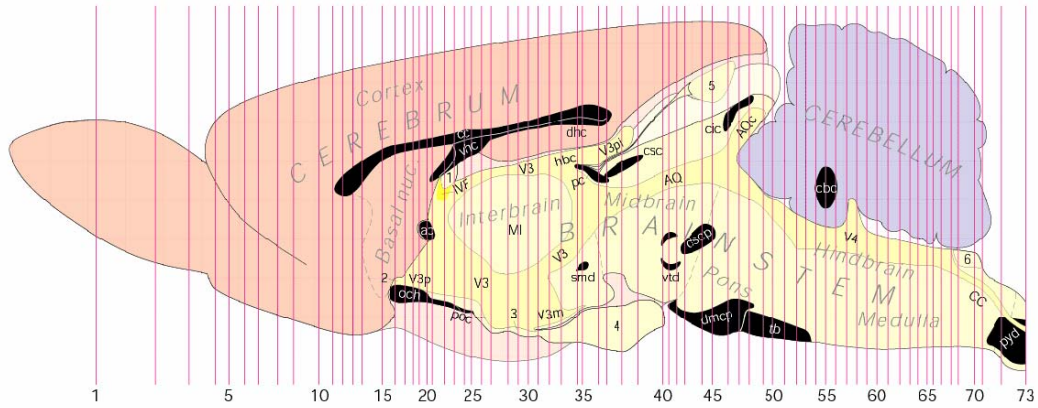


Figure 3.1: Based on complexity of the different brain levels, Swanson has used a variable number of sections per unit length of the brain. [12]

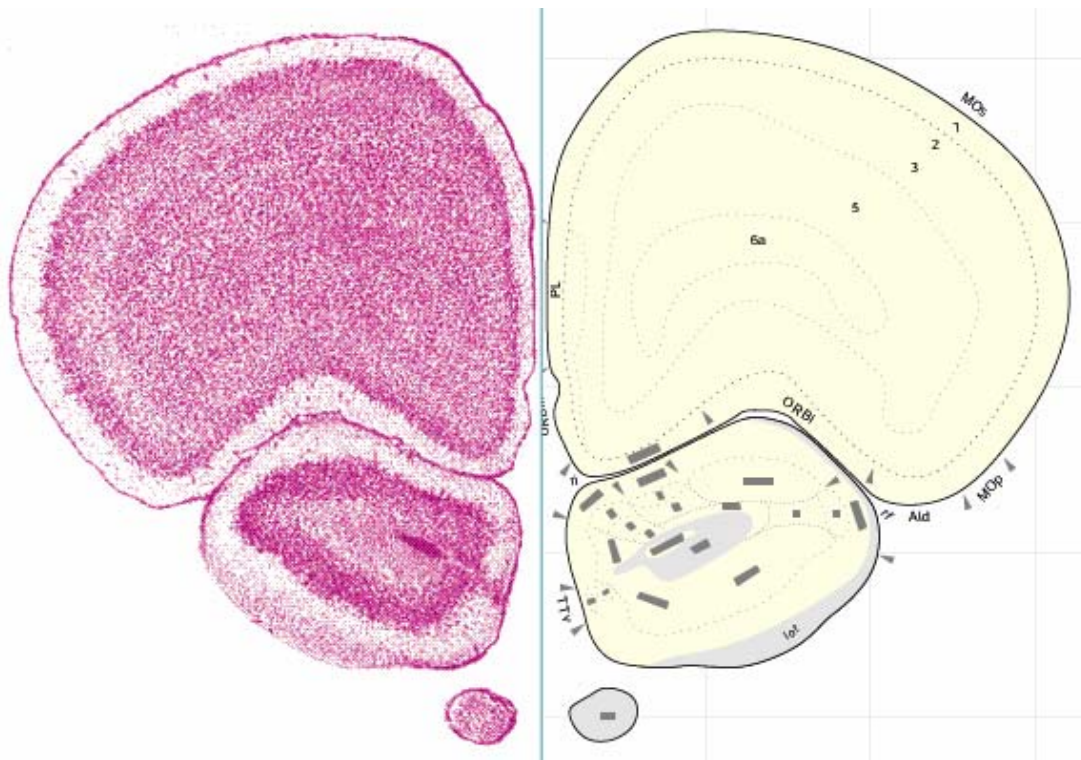


Figure 3.2: Left: Original Nissl-stained brain photomicrographs. Right: Freehand drawing of the brain and delineation of the neuroanatomical region using *AI™* software [12]

3.1.1 Discrepancies of the atlas

A working knowledge of a good computer graphics drawing application (such as Adobe Illustrator or Macromedia Freehand) is essential for modern rendering and display of structural information. These applications are based on vector graphics, which are mathematical descriptions of drawings that have a relatively small file size and can be scaled virtually infinitely without loss of detail. Pixel-based applications are appropriate for the manipulation of digital information (scanned photographs or videophotos), but produce crude drawings and very large file sizes.

There are many advantages of vector graphics over pen and ink drawings.

Technical advantages

- Uniform line thickness, any color and very smooth lines can be drawn.
- Any Bezier curves and irregular lines can be drawn and manipulated with relative ease.
- Computer graphics has advantage of working with layers which dramatically increases the usefulness of drawing because any combination of layer can be chosen for display or printing.
- Cloning and modification of existing files is a major advantage of computer graphics over traditional drawing methods that saves lot of time in map creation.
- The file size is relatively very small and can be virtually zoomed into any resolution without losing clarity.

Despite the aforementioned advantages of the templates and computer drawings, they can be computationally incompatible with existing software and platforms requiring image and graphics information. Also due to inherent characteristics of their creation,

which is freehand drawings, they might not comply with strict geometric rules which define the entities represented in the atlases or computer drawings. The following section, delineates issues and flaws encountered in the Swanson's atlas which prevent it from being used in a 3D form. The next section discusses the measurements and techniques used to resolve those issues. The following list identifies the major flaws found in the atlas:

- Multiple lines and curves bundled into a single boundary,
- Non-intersecting or over-extended spline segments,
- Overlapping regions,
- Functional or physical areas labeled remotely from the region, and
- Regions without any anatomical label.

3.1.2 Multiple lines and curves bundled into a single boundary

Multiple lines and curves bundled into a single boundary was the most common problem in the atlas. Adobe Illustrator (AI®) "preview" feature masks this redundancy such that the drawing looks as intended. Turning this feature off reveals multiple lines on the boundary of regions which have been created by the drawer when s/he was trying to generate neighboring regions. Figure 3.3 shows an example of such a situation. These multiple lines violate the unique definition of each region making the database unsuitable for generation of a 3D database.

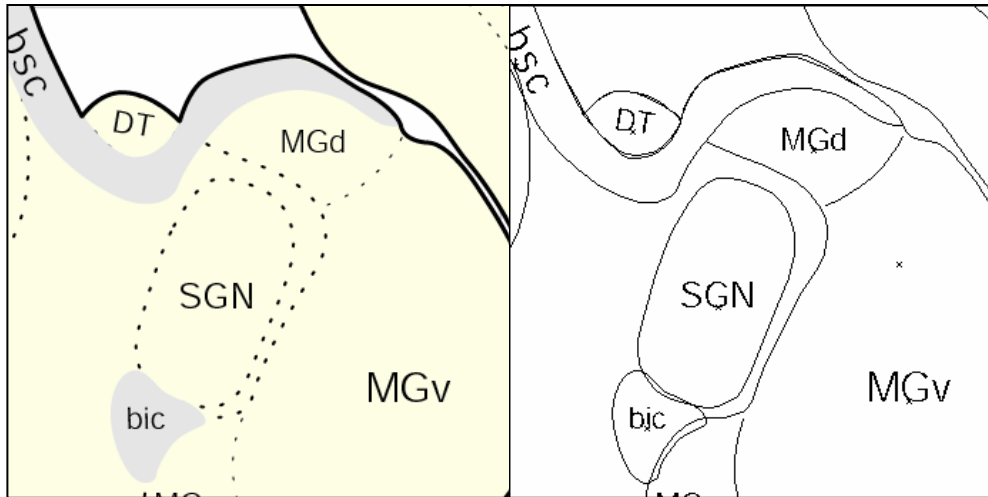


Figure 3.3: Left: A part of a brain map in AI® with preview mode on, Right: same section with preview mode off. Notice the bundled lines and curves in the boundary of the regions

3.1.3 Nonintersecting or over-extended spline segments

Numerous situations exist within the atlas drawings where the splines are neither connected nor close to any adjacent geometry entity. This condition makes the delineation of the regions ambiguous. If a bleeding algorithm were used to identify the regions of the brain, these open splines would foil the process. Figure 3.4 shows an example of such a case in the atlas.

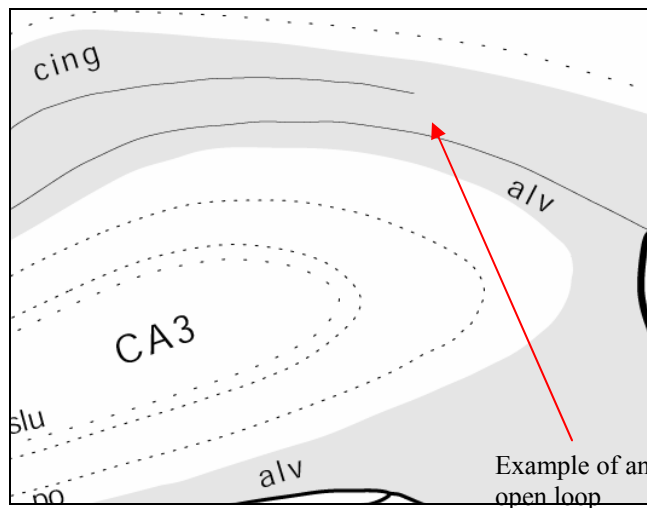


Figure 3.4: An example of un-connected spline in the brain map

3.1.4 Overlapping regions

Since Swanson has used the mask layer feature of AI® to generate the drawings, the boundaries of the regions frequently overlap creating ambiguous situations such as in Figure 3.5. In this example a region was created which has no meaning.

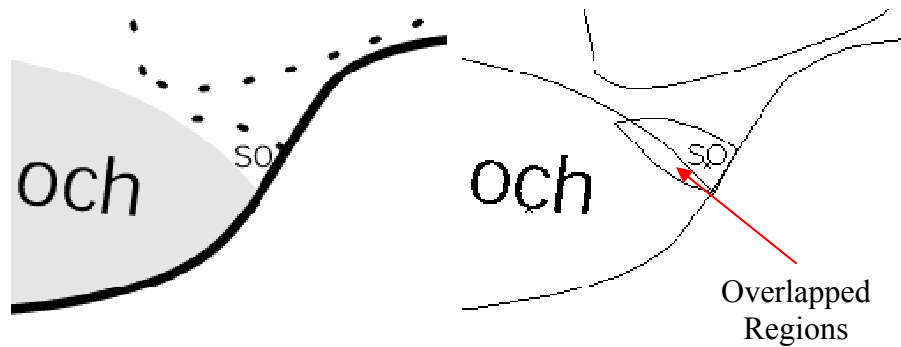


Figure 3.5: Overlapping regions in rat brain atlas

3.1.5 Remotely labelled regions

Some atlas boundary delineations were not intentionally drawn to keep the templates neat and simple looking. An example of such a case is for the areas that control the motion activities of the rat brain. Instead of having the lines inside the drawings, dart-shaped markers were placed on the exterior of the brain to indicate the direction of hypothetical lines, Figure 3.6.

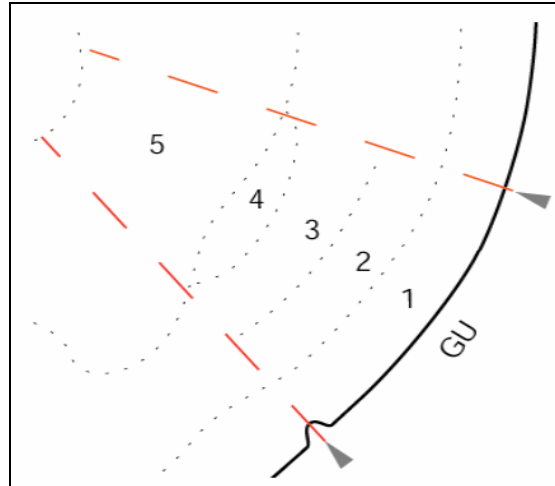


Figure 3.6: Dart-shaped symbols indicate the direction of the boundaries which are supposed to exist (red dashed lines).

3.1.6 Other issues

In addition to the flaws mentioned previously, there are other issues to be addressed. In some slices, abbreviated labels were used for labeling sub-regions of neuro-anatomical areas. Obviously these labels do not exist in the label listing of the atlas as they appear on the drawings. For example in level 26, there are labels such as pmi or mpv which are sub-regions of paraventricular nucleus hypothalamus (PVH) and they should read as: PVHpmi and PVHmpv in order to show their relevance to the main area. Also we encountered instances of areas that did not have any labeling although they had a clear boundary curve delineating the region from the background. Cerebellum lobes within drawings were composed of dotted lines. These lines were not delineations of any anatomical or neuroanatomical regions. Some regions contained multiple labels. The atlas authors did not clearly divide them into sub regions.

3.2 Making Computationally Robust Data

The majority of these flaws have been handled automatically by the routines developed, but minor preliminary manual adjustments were required. The manual adjustment includes: repositioning text at appropriate location; resizing text, to guarantee that the text is located within the region; exporting AI files to CADL format which is an ASCII type file.

The CADL files for each slice are read and data are converted to node and element format. Each node is defined by x and y coordinates. Each element is defined by two nodes it connects and two anatomical areas it separates. A sequence of functions, which use different algorithms, is then called to fulfill following tasks in that order.

1. spline approximation,
2. extend, insert and merge overlapping nodes and elements,
3. Identify loops of regions, i.e. assign each element two material codes of text labels whose regions are divided by that element.
4. Make the left part of the brain by mirroring the right side since original Swanson' atlas is bisymmetric.

3.2.1. Spline Approximation

The dominant drawing entities are splines. To reduce the complexity of calculations, and hence the CPU usage time, they were approximated by polylines. Each segment of the spline was replaced with 4 straight lines. To demonstrate this better, in equation 3.1 if we just give the spline parameter, i.e. t , start and ending values, the spline will be presented by a single line, as in Figure 3.7.

$$\begin{aligned}
 x_i &= ax_i \cdot t^3 + bx_i \cdot t^2 + cx_i \cdot t + dx_i \\
 y_i &= ay_i \cdot t^3 + by_i \cdot t^2 + cy_i \cdot t + dy_i
 \end{aligned}
 \tag{3-1}$$

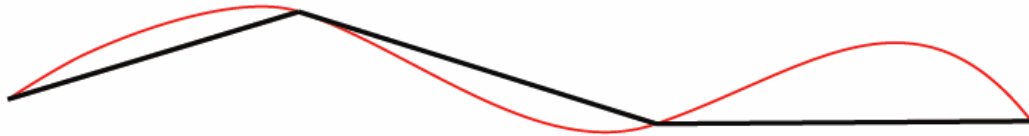


Figure 3.7: Spline Approximation Red curve is the spline which has been roughly approximated by assuming just two values of 0 and 1 as for its parameter.



Figure 3.8: The same spline approximated with for line segments, corresponding to t values of 0, 0.25, 0.75 and 1.

The routine that reads the splines, handles the approximation by using four values for t: 0, 0.25, 0.75 and 1 (Figure 3.8). The maximum error incurred was less than ¼ of a percent (0.0025). This insignificant error was associated with area shrinkage for splines with drastically changing curvatures (for example for splines depicting the choroids plexus (CHP) in section 25 of the brain). After this step, all overlapping nodes are merged. The linear span was less than 3×10^{-8} of the box width enclosing the brain map.

3.2.2 Extend/Intersect/Merge

The term “Node” refers to endpoints of each line segment and “Element” is used for the lines connecting the nodes. Note that all the data extracted from AI™ files, including splines, lines, and conic sections are now represented/approximated by a finite

number of lines. Therefore our database of atlas drawings consists of nodes and their coordinates and the connectivity of those nodes defined by the elements.

Open loops are identified by nodes attached to only one element. The algorithm follows:

Do Loop until the last node, i

If node_i exists in at least at 2 elements,

Continue loop i;

Else

*Find the shortest normal distance from the node_i to adjacent elements and save the element number: **element_j**;*

*If node_i lies within the **element_j** box,*

*Snap node_i into **element_j**;*

Else

*Connect node_i to the closest node of **element_j**;*

End Loop

The 2 different situation of connecting an open node to an element or another node is depicted in Figure 3.9.

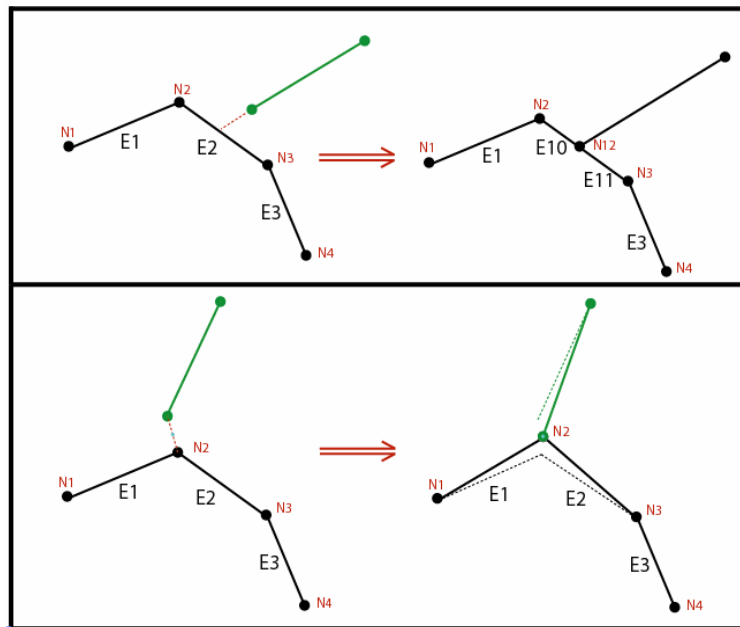


Figure 3.9: Above: Open node lies in the E2 element box, thus it is snapped into element. Below: Open node is outside the box, so it is directly connected to endpoint of the E2

New nodes were created whenever two elements intersected. This step was necessary because our algorithms assume that all elements separate two distinct materials only. Consequently, any intersecting elements are converted into 4 elements with the new node common to all. This guarantees a consistent topographic map of elements and nodes. This concept can be expressed as:

$$\text{if } x \in A \cap B \Rightarrow x \in A1 \cup B1,$$

where,

A : Set of points belonging to element 1

B : Set of points belonging to element 2

$A1$: Endpoint nodes of A , $n(A) = 2$

$B1$: Endpoint nodes of B , $n(B) = 2$

The same applies for elements, i.e. there can't exist two elements connecting the same two nodes, therefore:

$$A \subseteq B \Rightarrow A = B, \text{ or}$$

$$\text{if } n(A \cap B) > 1 \Rightarrow A = B$$

Thus we also merged redundant elements, Figure 3.10.

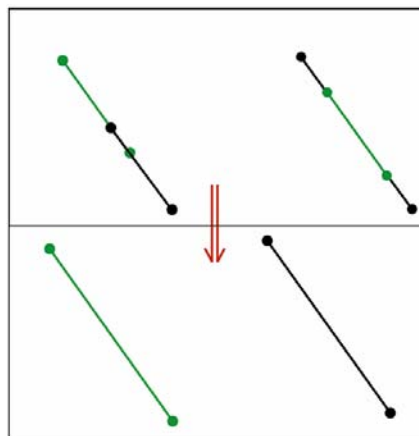


Figure 3.10: Merging redundant elements

3.2.3 Identify brain regions

In this step, the code categorizes elements to define regions corresponding to different areas of the brain. The text labels, provided in each brain map, were used as seed point locations. There were 1272 labels identifying the various neuroanatomical areas of the brain. Each element will assume two new features in addition to its nodes: material code A and B which have been separated by the element.

In order to determine tissue codes for each element, the coordinates of the seed points (atlas text labels) were used. A temporary semi-finite line was added to our nodes and elements database whose start point coordinate was the same as the seed point and its direction was completely arbitrary. Then all the elements intersected by this newly introduced line were tagged as potential elements belonging to tissue type in question. In order to narrow down to just one element, the tagged elements were sorted based on their distance to the seed point and the closest one was chosen as the element delineating the boundary of tissue A of the brain. Now one can legitimately assume that there exists at least one element attached to the recently found element which is also part of the boundary of tissue A. If more than one attached element exists, then the elements will be selected whose cross product with the current one results in a positive vector, in other words, using this method we choose the most left element connected to a current one. 'Left' is defined as the left hand side of an imaginary observer who is walking on the trail of current element from its tail to its head. Now that a new element of tissue type A has been identified, the algorithm will continue to find the next legitimate attached element. This process will continue till we find all the elements forming a closed loop around that

specific tissue type of the brain. We will refer to this process as a counter clockwise marching line algorithm, Figure 3.11.

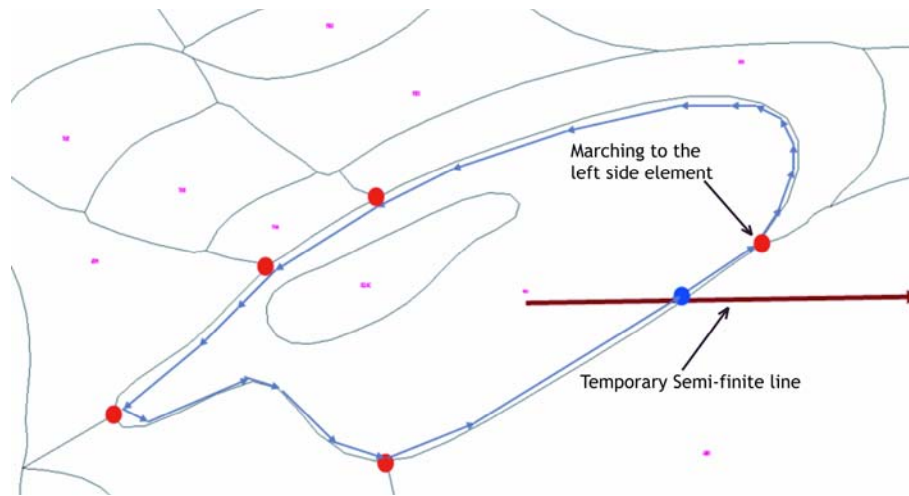


Figure 3.11: Using seed points to identify regions of the brain and assigning material codes to the defining boundary elements.

This algorithm can be expressed as:

Shoot a semi-infinite line and collect the intersected elements

Find the closest intersected element to the seed point and take it as the starting element

Do Loop until current elements becomes start element

Proceed to the next element based on a tail-to-head logic

If the current head node is shared by more than one element, select the element based on right-hand rule, i.e. steer to the relative left element

Keep the current element information in an array

End Loop

If the number of shared elements between the current loop and elements in global array of intersected is even

Repeat the above loop

Else

Assign the tissue code of the current seed point to the elements of the already recognized loop.

This algorithm can be used for all the seed points in the current map, but it does not guarantee that all the elements within our database have been completely classified. There can be instances that some elements would only have one tissue code assigned to them because they were located in the map such that they were close to only one seed point, i.e. they have been crossed only once by imaginary semi-infinite lines. Thus the second ID code for the loop elements is unknown.

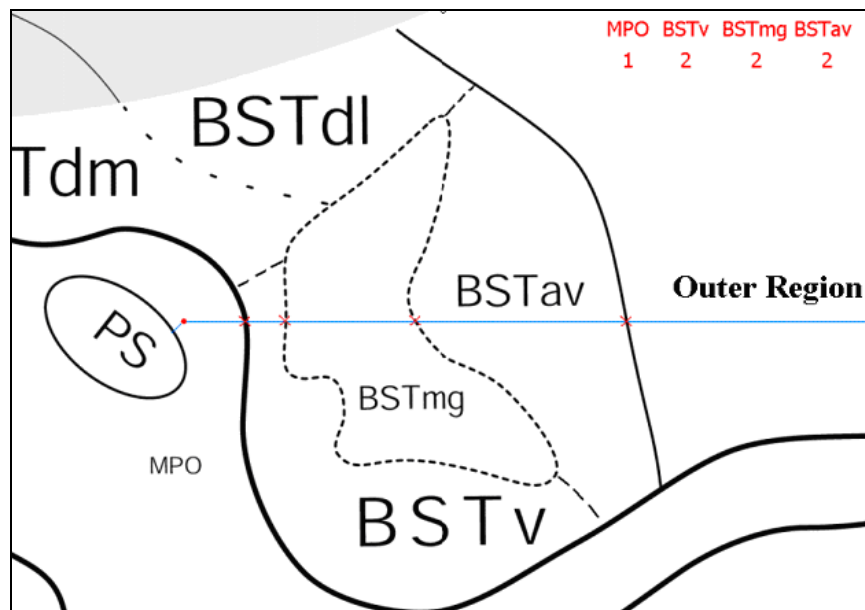


Figure 3.12: Finding the isolated islands and figuring out the second material code

Overlapping areas

As shown in Figure 3.12, the elements of region denoted by label “PS” could not be seen by other seed points except for “PS”. In order to resolve this issue we first need to identify those elements in our database. Then a simple, yet very efficient and robust, method was used to figure out the second ID. The following is the description of the method (see Figure 3.13).

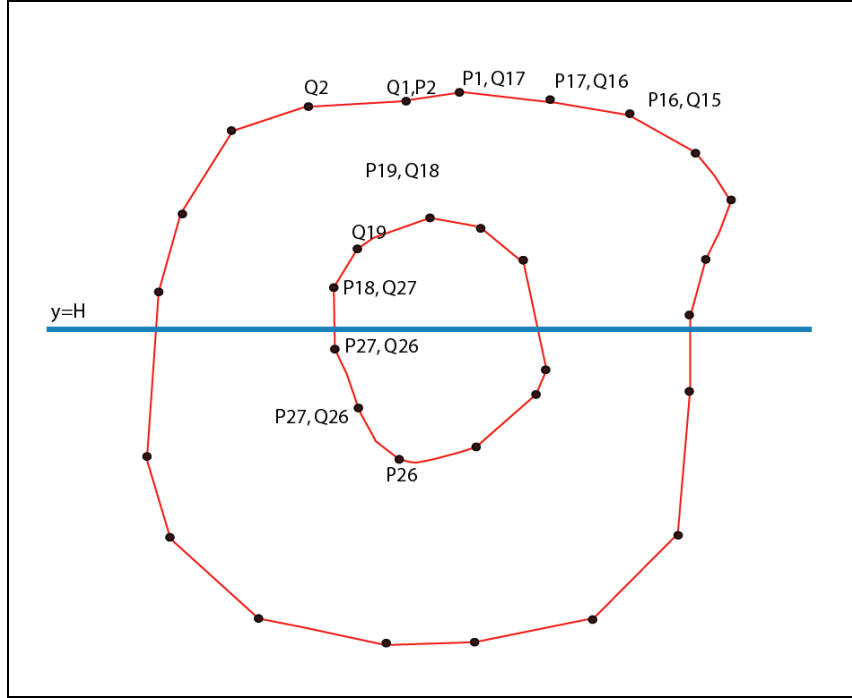


Figure 3.13: Line crossing algorithm to identify regions defined by line segments

- i) Create a semi-infinite line starting at midpoint of the element with one material ID.
- ii) Determine the intersection of line with all elements of the database. Let

$S = \{\overline{P_i Q_i}, i = 1, N\}$ be the set of line segments representing the region boundaries, and

$y = H$ be the equation of the horizontal line. The intersection points between the given horizontal line and the region are determined by considering the line segments

of S one by one. Consider line segment $\overline{P_i Q_i}$ as an example.

Write $X_1 = X(P_i), Y_1 = Y(P_i), X_2 = X(Q_i), Y_2 = Y(Q_i)$. There is intersection if

- a) $(Y_1 - H)(Y_2 - H) < 0$ or
- b) $(Y_1 - H)(Y_2 - H) = 0$ and $(H > Y_1$ or $H > Y_2)$

For any other cases, it is considered that there is no intersection. The point of

intersection is given by:

$$\left(X_1 + \frac{(H - Y_1)(X_2 - X_1)}{(Y_2 - Y_1)}, H \right)$$

- iii) The intersection points are arranged in ascending magnitude of X
- iv) Find the region codes present in the intersection list and count the number of each code.

The region ID whose occurrence count in intersection list is odd will be our missing code for the isolated loop (Figure 3.12)

This can be shown as following algorithm.

- *Identify the elements with only one material code Identify the elements with only one material code*
- *Shoot a semi-infinite line from midpoint of the element and collect the intersected elements*
- *Count the number of occurrence of each material in the intersected element list*
- *Pick the material code which has the odd number of occurrences and assign it to the elements of the current loop.*

3.2.4 Overlapping Areas:

When boundary definitions overlap void regions are created which need to be zippered. Elements adjacent to these void regions are missing one of the material attributes and can be identified easily. The void region is zippered by calculating midline locations between opposing boundaries as shown in Figure 3.14.

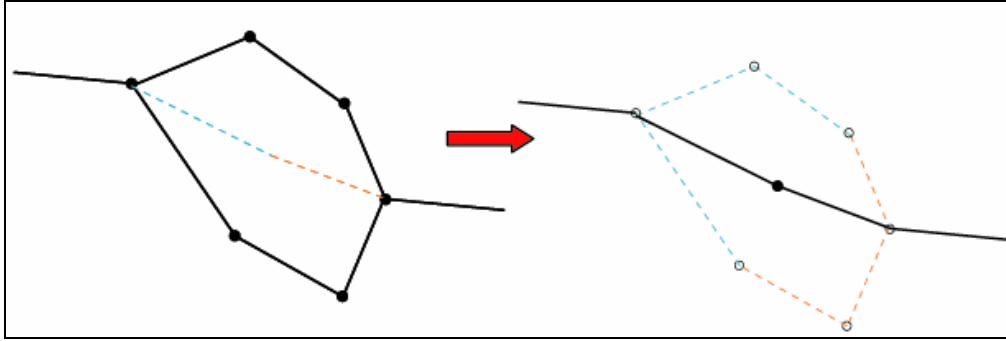


Figure 3.14: Removing the void loops whose elements have just one material code

3.2.5 Mirroring and output

After all elements are identified and assigned to appropriate loops, a routine re-sequences the node and element numbers prior to output. The atlas took advantage of symmetry and created only the left half. We mirrored the nodes and elements along the Superior-Inferior midline to create the full brain image.

The code outputs in ASCII format a text file containing the node numbers and their coordinates as well as the elements and their four attributes (two node numbers and two material codes).

3.3 Converting data into Pixel image set

The output file delineates each material region uniquely. They are suitable for further numerical analyses such as constructing pixel image data set or surface mesh. To use this brain atlas as a template for MRI images it is converted to pixel images where pixel intensity represents the anatomical area of the brain as listed in excel file. Figure 3.15 shows axial section of brain displayed in pseudo-color in MIVA software. The resolution of this image is chosen to be 512 by 512 pixels to encompass smallest anatomical area. The original vector data can be converted to any higher resolution if analysis speed and size of dataset is not an issue.



Figur 3.15: The Rat brain axial slice after segmentation. Each colored area defines unique anatomical area.

The original slices through the brain were not equally spaced. Most imaging software including MIVA require that axial image slices collected should be equidistance throughout dataset. We generated three hundred equidistance slices to account for smallest distance between original two atlas slices. The locations where information was not available were generated using nearest neighborhood algorithm. The final Atlas image dataset was 512 pixels X 512 pixels X 300 slices, corresponding to a 30 micron in-plane pixel spacing and slice separation of 70 micron.

3.4 Atlas 3D

After creating segmented images, surface models were generated using multiple materials marching Cube (M3C) algorithm [15]. A virtual cube was used to march through pairs of adjacent segmented images in a set. To improve the quality and

efficiency of the existing surface model linearization [16] smoothing and decimation was used. Smoothing is a technique that adjusts the node coordinates to improve the appearance of a mesh, and/or improve the shape of surface triangles. Contrary to the smoothing procedure, which does not change the number of nodes and triangles of a surface model, a decimation algorithm reduces the total number of surface triangles, while maintaining a good approximation to the original geometry.

3.5 Classification of Anatomical area: (The Tree Browser)

Further these 1277 segmented anatomical areas were grouped in to about 100 region of interests called sub-major areas. The sub-major areas were collected to a dozen major areas. A utility (program) was developed to display and choose different anatomical areas. Due to the hierarchical or tree like organization of major, sub-major and minor areas we called this utility as a tree browser. Figure 3.16 shows Tree-Browser with few anatomical areas displayed with entire shell of the rat brain. This tree browse is used as an utility to define regions of interest in fMRI project. The tree browser also has identified functional systems such as reward (dopamergic) pathway, olfactory system. The power of tree browser can only be realized when seen in action on computer screen. Following figures give some idea of the visualization capability of Tree Browser. Figure 3.16 shows layout of selection panel of anatomical areas with Rat brain shell displayed in visualization window. Figure 3.17 shows anatomical areas inside brain shell where as Figure 3.18 shows reward system as functional area.

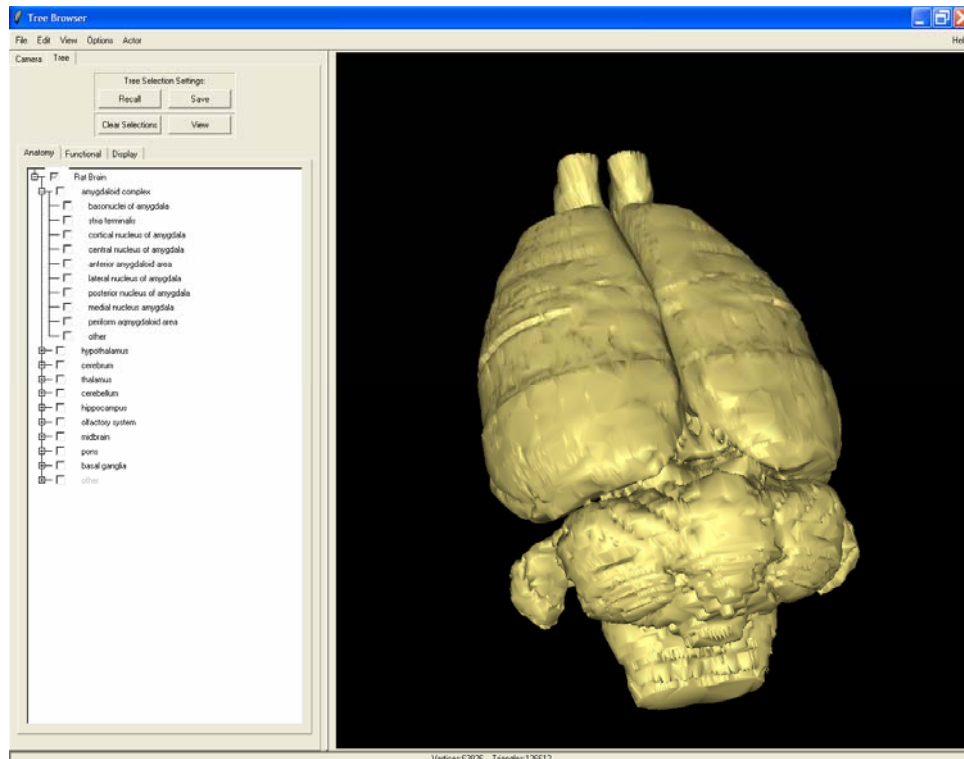


Figure 3.16: The Tree Browser with Rat Brain Shell.

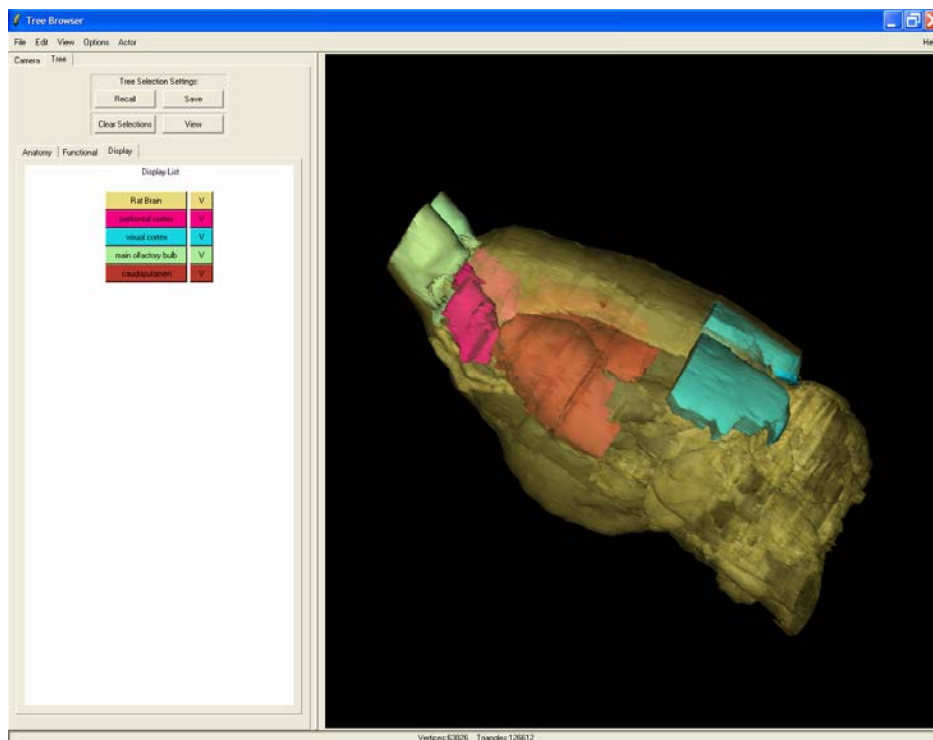


Figure 3.17: The Tree Browser with four anatomical areas.

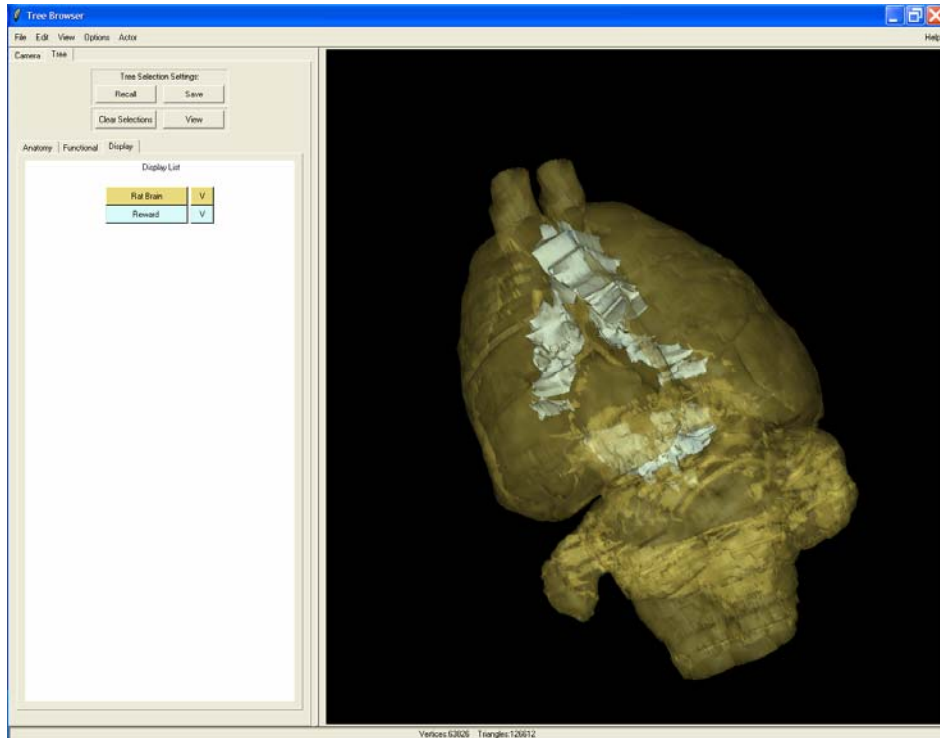


Figure 3.18: The Tree Browser with functional area (Reward System)

4: Registration, Segmentation and Data Analysis

To analyze functional MRI data, in general, a researcher or physician must perform

1. Registration,
2. Segmentation and
3. Statistical analysis

of the data in that order. Naturally an experienced researcher can look at a set of slices create loops around the region/s and run statistical tests to decide if that region/s are activated or not. However in that method they have 1) registered the image mentally picturing the area of interest then they 2) segmented the area by creating loop around the region and finally, performed a 3) statistical analysis within the loop. For this process a user needs very good understanding of the subject anatomy as well as knowledge of MRI physics (since T1 and T2 weighted images of same slice have very different pixels intensities). Also user must have very good hand-eye coordination or sophisticated tools to draw consistent ROIs in all images.

fMRI data is usually very noisy due to the lower resolution sampling and frequently responses from different subjects given the same stimulus are similar, but not exactly same. In behavior studies mapping functional areas of combined responses from multiple subjects improves the statistical power of the analysis. Naturally registering, segmenting and analyzing multiple images individually is a very time consuming task and can introduce human error in the analysis. In this work a semi-automatic quantitative analysis strategy was developed and optimized for the rat brain.

4.1 Coordinate system and their transforms

Before addressing registration segmentation process it is important to be familiar with coordinate systems and how the transformations occur within these systems.

Image coordinate system: defines the coordinate associated with image. The origin is located at the upper left corner in the first slice of image set. The x-axis is from left to right along a given row [the column direction]. The y-axis is top to bottom of a given column [up to down along the row direction]. The z-axis is from the first slice to the last slice along the plane direction, as shown in figure 4.1(a). The pixel/voxel location is always described in integer number from origin.

World coordinate system: describes the movement (translation rotation and scaling) in the real world. It is generally defined by the RAS coordinate system. The origin is positioned at the center of the FOV (field of view). The x-axis is from the left to right (L-R). The y-axis is from the posterior to anterior (P-A). The z-axis is from the inferior to superior (I-S), also shown in figure 4.1(b)

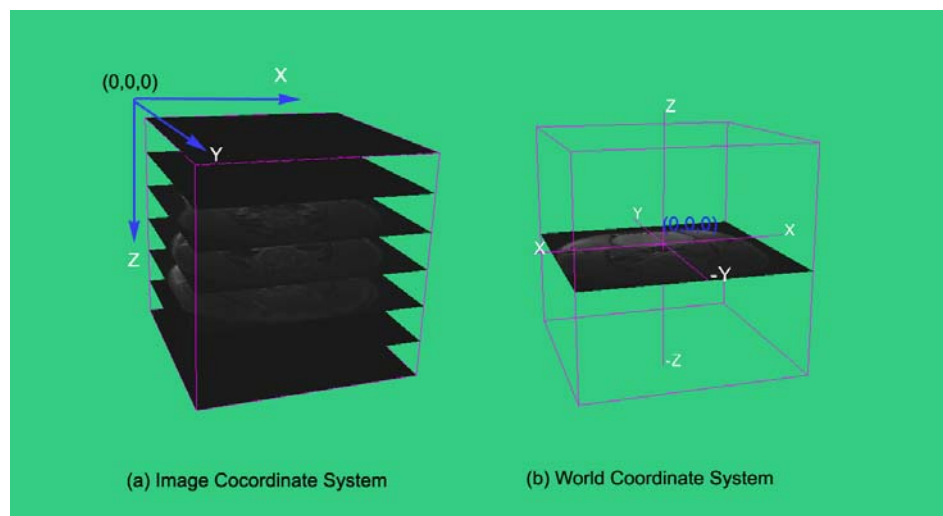


Figure 4.1: Image and World Coordinate System

4.1.1 Image-to-world Transform

Image-to-world transform is performed in the subject space to map the image coordinate to world coordinate. Three-dimensional subject space is defined with dimensions $[D_{sx}, D_{sy}, D_{sz}]$ in x, y, z directions.

$$\text{Spacing (voxel size) in x: } v_{sx} = \frac{FOV_{sx}}{D_{sx}}$$

$$\text{Spacing (voxel size) in y: } v_{sy} = \frac{FOV_{sy}}{D_{sy}}$$

$$\text{Spacing (voxel size) in z: } v_{sz} = \frac{FOV_{sz}}{D_{sz}}$$

The image-to-world transform T_s is calculated by

$$T_s = V_s \cdot C_s \quad (4.1)$$

Center Matrix C_s describes the movement of image coordinate from origin of image coordinate system to that of world coordinate system.

$$C_s = \begin{bmatrix} -1 & 0 & 0 & \frac{D_{sx}}{2} \\ 0 & -1 & 0 & \frac{D_{sy}}{2} \\ 0 & 0 & 0 & -\frac{D_{sz}}{2} \\ 0 & 0 & 0 & 1 \end{bmatrix} \quad (4.2)$$

Voxel size matrix V_s describes the voxel sizes in x, y, z directions, respectively.

$$V_s = \begin{bmatrix} v_{sx} & 0 & 0 & 0 \\ 0 & v_{sy} & 0 & 0 \\ 0 & 0 & v_{sz} & 0 \\ 0 & 0 & 0 & 1 \end{bmatrix} \quad (4.3)$$

4.1.2 World-to-image Transform

World-to-image transform is performed in the reference space to map the world coordinate to image coordinate. Three-dimensional reference space is defined with dimensions $[D_{rx}, D_{ry}, D_{rz}]$ in x, y, z directions.

$$\text{Spacing (voxel size) in x: } v_{rx} = \frac{FOV_{rx}}{D_{rx}}$$

$$\text{Spacing (voxel size) in y: } v_{ry} = \frac{FOV_{ry}}{D_{ry}}$$

$$\text{Spacing (voxel size) in z: } v_{rz} = \frac{FOV_{rz}}{D_{rz}}$$

The world-to-image transform T_r is calculated by:

$$T_r = V_r^{-1} \cdot C_r^{-1} \quad (4.4)$$

Center Matrix C_r describes the movement of world coordinate from origin of world coordinate system to that of image coordinate system.

$$C_r = \begin{bmatrix} -1 & 0 & 0 & \frac{D_{rx}}{2} \\ 0 & -1 & 0 & \frac{D_{ry}}{2} \\ 0 & 0 & 0 & \frac{D_{rz}}{2} \\ 0 & 0 & 0 & 1 \end{bmatrix} \quad (4.5)$$

Voxel size matrix V_r describes the voxel sizes in x, y and z directions, respectively.

$$V_r = \begin{bmatrix} v_{rx} & 0 & 0 & 0 \\ 0 & v_{ry} & 0 & 0 \\ 0 & 0 & v_{rz} & 0 \\ 0 & 0 & 0 & 1 \end{bmatrix} \quad (4.6)$$

4.1.3 Image-to-image Transform

The overall transformation from subject space into reference space is represented by a single matrix T , which is the product (concatenation) of world-to-image transform T_r , world-to-world transform T_w , and image-to-world transform T_s .

$$T = T_r \cdot T_w \cdot T_s \quad (4.7)$$

4.2 Registration

Image registration is a prerequisite to numerous imaging applications in the neurosciences. Registration is required for three dimensional reconstruction, multimodality image mappings, atlas construction and arithmetic operations such as image averaging, subtraction and correlation. Physical sectioning procedures, unlike various tomographic imaging techniques, also require additional superpositioning schemes to register serial sections. Since the mid 1980s investigators have used several approaches, with varying degrees of manual interaction, to perform image registration. These approaches use either information obtained about the shape and topology of objects in the image, or the presumed consistency in the intensity information from one slice to its immediate neighbor or from one brain or image set to another.

MR image registration techniques can be grossly classified as shown in Figure 4.2. Our objective is to register MRI anatomy images of multiple subjects to completely segmented atlas using minimal or no user intervention. Next sections describe how these different registration techniques work and their combined incorporation for a registration process.

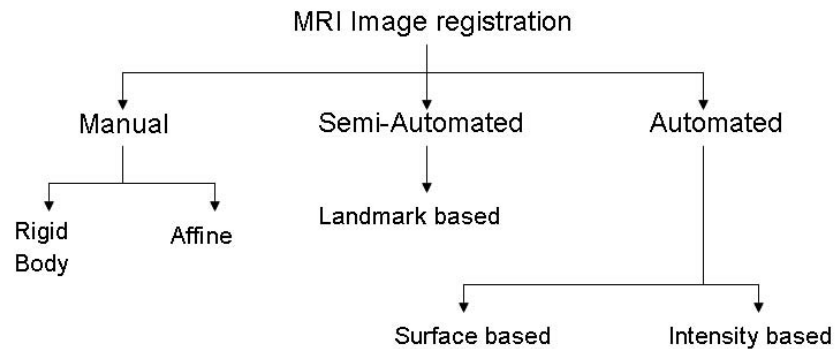


Figure 4.2: Classification of Image registration techniques.

4.2.1 Manual Registration

Manual registration requires the user to do all the registration work interactively based on the visual feedback from a computer visualization system. Many medical image applications [17,18] provide the utility for manual registration to register image studies from same or different modalities. Users are able to manipulate images through 3 orthogonal views (axial, coronal and sagittal) interactively with real-time visual feedback and achieve accurate alignment with the help of internal and surface features.

Figure 4.3(a) shows manual registration pallet in Medical Image Visualization and Analysis (MIVA) software. Good alignment can be achieved by manual adjustments of one image volume to fit another in three-dimensional space. The registration is the linear combination of the translation, rotation, scale factors in x, y, z directions, respectively. Figure 4.3 (b) shows overlay of reference (colored) image on subject image (gray) prior to registration and Figure 4.3 (C) shows after manual registration.

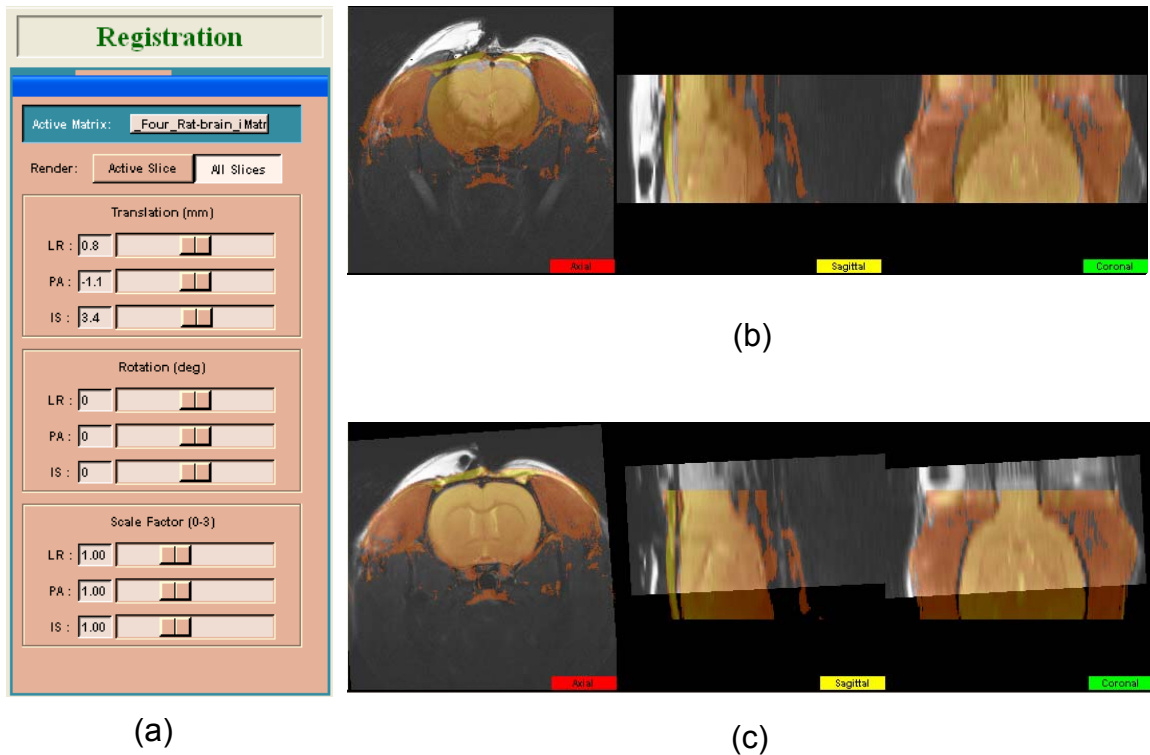


Figure 4.3: Manual Registration. (a) Registration pallet. (b) Before registration and (c) After registration. [18]

4.2.2 Landmark Registration

Landmark registration involves the identification of the coordinates (locations) of corresponding points within different images and determination of the spatial transformation to align these points.

There are two types of landmarks: internal landmarks and external landmarks. Internal landmarks are commonly known as anatomical markers, which are visible point-like anatomical features within the images of all the modalities. They are selected and marked by medical experts by means of software to define and register anatomical areas. An external marker is an artificial object that can be attached to the patient before the image acquisition. They need to be visible and easily identified within all images.

The basic process of landmark registration is: (1) identify and pair landmarks (anatomical features or external marker) from the corresponding images. (2) Calculate the geometrical transformation by minimizing the distance between the coordinates of these landmarks. Now let

$[S]$ = global co-ordinates of a Subject's Markers.

$[A]$ = the paired global co-ordinates of the Atlas or Reference Markers.

We seek a homogeneous coordinate transformation matrix $[T]$ that will map the subject onto the Atlas space, i.e. $[A] = [T][S]$. This 4x4 $[T]$ matrix can provide complete linear transformations (rotation, translation, scaling, skew, and perspective distortion).

A deterministic solution for the transformation matrix $[T]$ is available given 4 non-planar Markers in each dataset. In that situation the $[S]$ and $[A]$ matrices are 4x4 as well. Post-multiplying both sides by $[S]^{-1}$ yields the desired $[T]$ matrix, i.e.:

$$[T]_{4 \times 4} = [A]_{4 \times 4} [S]_{4 \times 4}^{-1} \quad (4.8)$$

The success of this four point registration depends on the matching of the paired landmarks in both sets as well as the spatial separation of the Markers. This strategy is incredibly fast and serves as an initial registration mechanism wonderfully. However, misalignment of a single marker can have significant negative consequences. If we use more than four markers then we have an over specified solution and it becomes an error minimization problem. The least square analysis is the most accepted statistical estimation strategy among scientist and engineers. The system equation in matrix form is

$$[A]_{4 \times n} = [T]_{4 \times 4} [S]_{4 \times n} \quad (4.9)$$

Where n is number of landmarks or markers. Define an error vector residual ε :

$$\varepsilon = A - TS$$

Select \hat{T} in such a way that the criterion $J = \sum_{i=1}^n \varepsilon_i^2 = \varepsilon^T \varepsilon$ is minimized.

$$J = (A - TS)^T (A - TS) \quad (4.10)$$

$$J = A^T A - 2A^T TS + S^T T^T TS \quad (4.11)$$

Differentiate J with respect to T and equate the results to zero to determine the condition on the estimate \hat{T} such that J is minimized.

$$\left. \frac{dJ}{dT} \right|_{T=\hat{T}} = -2S^T A + (2S^T S)\hat{T} = 0 \quad (4.12)$$

The solution for \hat{T} is:

$$\hat{T} = (S^T S)^{-1} S^T A \quad (4.13)$$

The landmark registration strategy can provide excellent alignment and has significant advantages compared to the 4-point registration due to the sensitivity of the fully constrained 4-point method. Both landmark registration strategies (the 4-point and n-point) yield excellent agreement between reference and subject sets after registration. The results are consistent, unbiased, and highly efficient. The system is rapid and requires an error analysis consisting of only the Marker points which is sparse compared to any pixel intensity-based registration strategy. This registration technique is demonstrated in figure 4.4.

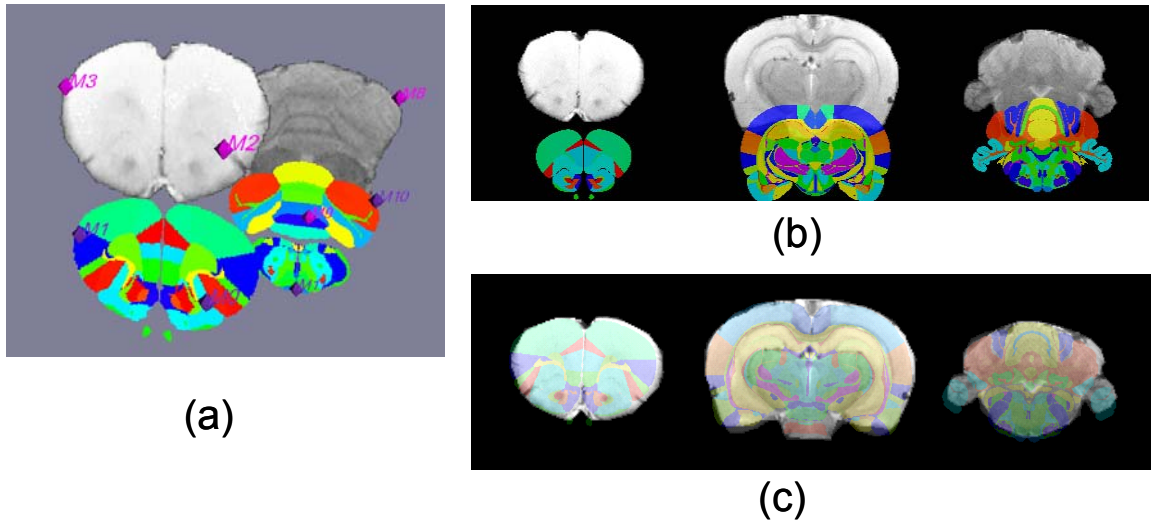


Figure 4.4: shows a simple example of 2D landmark registration between an MR image and a rat brain atlas. (a) Landmarks chosen on Subject and Atlas. (b) Before registration (c) After registration

4.2.3 Intensity-Based Registration

Since the early of 1990s, many fully automatic algorithms have been put forward for image registration based on optimizing voxel similarity measures. From the statistical view an image is the distribution of a random variable (image intensity). Voxel intensity-based registration measures the similarity of two images, the distributions of two random variables, by the statistical description and maximizes it by optimizing the transformation parameters.

4.2.3.1 Correlation Coefficient (CC)

The correlation coefficient (CC), also called Pearson's product-moment correlation coefficient, is used for the intra-modality registration. It is expressed as

$$CC = \frac{\sum_x (A(x) - \bar{A}) \cdot (B^T(x) - \bar{B})}{\sqrt{\sum_x (A(x) - \bar{A})^2} \cdot \sqrt{\sum_x (B^T(x) - \bar{B})^2}} \quad (4.14)$$

In which \bar{A} and \bar{B} are the mean intensity value of image A and B, respectively. T is the transformation.[79,80,81]

4.2.3.2 Squared Intensity Difference (SSD)

The sum of squared intensity differences (SSD) measure [80,82] is also used for intra modality registration of medical images. The SSD measure is calculated by:

$$SSD = \frac{1}{N} \sum_{i=1}^N [A(x) - B^T(x)]^2 \quad (4.15)$$

where A(x) and B(x) are the intensity value at the corresponding voxel x in image A and B respectively. N is the total pixel numbers of two images. T is the Transpose.

4.2.3.3 Ratio Image Uniformity (RIU)

Woods et al [19, 20, 21] introduced the ratio image uniformity (RIU) as the similarity measure in 1992 for intra-modality alignment of PET and MR images, as well as cross-modality registration of PET and MR images.

If A(x) and B(x) are the intensity value at the corresponding voxel of image A and B, respectively, the gray scale intensity ratio is $R(x) = A(x) / B(x)$. The registration strategy assumes that R(x) is maximally uniform across voxels if the two images are accurately registered. If σ is the standard deviation of R(x) and \bar{R} is the mean value of R(x) over all voxels within the image set, this strategy uses σ / \bar{R} as the similarity measure used to evaluate how well the two images are registered.

$$\text{Image Ratio} \quad R(x) = \frac{A(x)}{B(x)} \quad (4.16)$$

$$\text{Mean value} \quad \bar{R} = \frac{1}{N} \sum_x R(x) \quad (4.17)$$

$$\text{Standard deviation} \quad \sigma = \sqrt{\frac{1}{N} \sum_x (R(x) - \bar{R})^2} \quad (4.18)$$

$$\text{Ratio image uniformity} \quad RIU = \frac{\sqrt{\frac{1}{N} \sum_x (R(x) - \bar{R})^2}}{\bar{R}} \quad (4.19)$$

4.2.3.4 Mutual Information (MI)

In 1994 Viola and Wells [22, 23], and Maes, et al [24] presented a new approach for maximization of mutual information based on information theory. This approach applies the concept of mutual information to measure the statistical dependence of two image intensity distributions. It is based on the assumption that the mutual information will be maximized if two images are spatially aligned.

According to communication (information) theory, the uncertainty of a discrete random variable X with probability mass function (pmf) $p_x(x)$ is measured by its entropy $H(x)$. The Shannon entropy[25] is defined as:

$$H(x) = -\sum_x p_x(x) \log p_x(x) \quad (4.20)$$

Given two discrete random variables x and y with joint probability mass function $P_{xy}(x, y)$, the amount of information that one variable contains about the other is given by their mutual information:

$$\begin{aligned} \text{Mutual Information} \quad MI &= H(x) + H(y) - H(x, y) = H(x) - H(x | y) \\ &= H(y) - H(y | x) \end{aligned} \quad (4.21)$$

where:

Joint entropy of x and y:

$$H(x, y) = -\sum_{x,y} p_{xy}(x, y) \log p_{xy}(x, y) \quad (4.22)$$

Conditional entropy of A given B and of B given A:

$$H(x | y) = -\sum_{x,y} p_{xy}(x, y) \log p_{xy}(x | y) \quad (4.23)$$

$$H(y | x) = -\sum_{x,y} p_{xy}(x, y) \log p_{xy}(y | x) \quad (4.24)$$

Therefore, mutual information is the difference between the marginal entropy of x and y and the joint entropy of x and y.

4.3 Registration strategy

It is important to realize that pixel intensities (or more correctly, index values) in the atlas data set is the alphabetical rank of that anatomical area. Thus pixel intensities in the atlas have no correlation to pixel intensities in MRI data set. Naturally this eliminates intensity based automated algorithms to register subjects to an indexed atlas. To

overcome this problem we divided this process into two stages;

- Intra registration or within modality (MRI-MRI) and
- Inter registration or between different modalities (MRI and segmented atlas).

4.3.1 Intra Registration

Here the goal is to align all subjects to the standard subject. One of N subjects is designated as the standard subject and all other $(N-1)$ subjects are aligned to this standard subject.

$$\{\text{Standard}\} = \{T_{\text{Subject-to-standard}}\}_j \{\text{Subject}\}_j$$

where $j=1$ to $N-1$.

The Intra-modality allows intensity based automated registration approaches. The most common strategy in the literature currently is the Automated Image Registration technique by Woods et al [27]

4.3.2 Inter Registration

Landmark registration strategies are best suited for inter registrations, Ex: to align standard anatomy to segmented atlas.

$$\{\text{Atlas}\} = \{T_{\text{Standard-to-Atlas}}\} \{\text{Standard}\}$$

Since two registration strategies are performed we need to multiply *Subject-to-Standard* transformation matrices by Standard-to-atlas Transformation matrix to register all subjects to atlas.

$$\{\text{Atlas}\} = [T_{\text{Standard-to-Atlas}}] [T_{\text{Subject-to-standard}}]_j \{\text{Subject}\}_j$$

$$\{\text{Atlas}\} = [T_{\text{Subject-to-Atlas}}]_j \{\text{Subject}\}_j$$

4.4 Segmentation

Subdividing an image into meaningful regions and labeling those regions for further analysis of the image is called segmentation. In fMRI data analysis segmentation is very critical process. It is important to report which anatomical area (ROI) exhibits activated voxels.

There are different methods for segmentation of an image. Segmentation can be done manually by an operator who has enough expertise in the area to understand the image as well as distinguish different regions in it. Also computerized image segmentation methods can be used to facilitate the automated image segmentation but the results of computer segmentation do not always comply with what the human brain can achieve. Automated image segmentation strategies can be roughly divided into two categories: a single contrast, or gray scale, segmentation where a single 2D or 3D image is used and multi-spectral image segmentation where multiple images with different gray scale contrast are available [28]. The most common approach for multi-spectral segmentation is pattern recognition [28, 83]. These techniques generally appear to be successful particularly for brain images, but much work remains in the area of validation. Figure 4.5 gives general categorizations of segmentation algorithms.

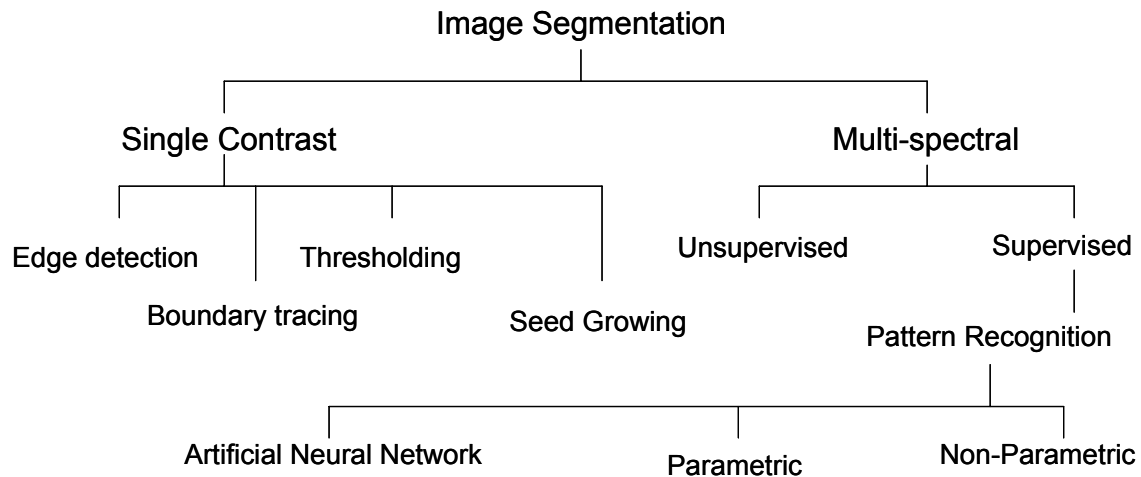


Figure 4.5: Classification of segmentation algorithms.

The difference between supervised and unsupervised methods is important due to the need for reproducible measurements. Supervised methods require operator input for segmentation. This can be done by selecting training pixels or training regions on the images. Unsupervised methods are automatic, in the sense that operator intervention may be necessary to complete the process but the result should be operator independent.

Though automated image segmentation is an active research area and holds potential, most of the segmentation algorithms are application specific and usually are tuned to one type of data set, for example MRI images with particular set of parameters. If we change those parameters (say instead of T1 weighted images use T2 weighted images) then it is very unlikely that same segmentation algorithm will work successfully. Segmentation algorithms can successfully delineate bigger structures like brain from cranium or structures that have significantly different properties from rest of the brain, like lesions from the rest of brain [29], but fail to differentiate smaller area like thalamus, hypothalamus, amygdala etc.

In this work we delineate different anatomical areas by superimposing the image onto Atlas and then extracting the segmented boundaries. This required the development of a completely segmented 3D Rat Brain Atlas. A caveat to this approach is that it assumes the subject rat brain is normal. If a subject brain has a tumor or other malady the alignment with an atlas will be in error. However, for most fMRI investigations, this assumption is valid.

4.4.1 Mapping MRI image

A common practice for functional Magnetic Resonance Imaging (fMRI) is to collect an anatomy volume image at an in-plane resolution of 256x256 with N slices through the brain. Subsequently, temporal sequences are collected at significantly lower in-plane resolutions, say 64x64 while retaining the same N slices through the brain. The reduced in-plane resolution allows a more rapid cycle frequency, a factor of 8 in this example. This compromise of spatial resolution is balanced by the enhanced transient data associated with the control and stimulation time dynamics of the fMRI study.

During the fMRI analysis each functional pixel deemed statistically significant is summed into the specific brain region based on the atlas registration. Consequently, it is imperative to reliably classify these voxels with the appropriate regions of the brain. Each subject [S] voxel is mapped to a specific location within the atlas [A]. The matrices $[T_{(Subject-to-atlas)}]_j$ that transformed the subject's anatomy to the atlas space were used to embed each slice within the atlas.

$$[A] = [T_{Subject-to-Atlas}] [S]$$

Since atlas resolution [512*512*300] is much higher than subject resolution [64*64*12] results in multiple atlas voxels occupying a single subject voxel. Now the subject voxel is classified based on centroid atlas voxel information or anatomical area.

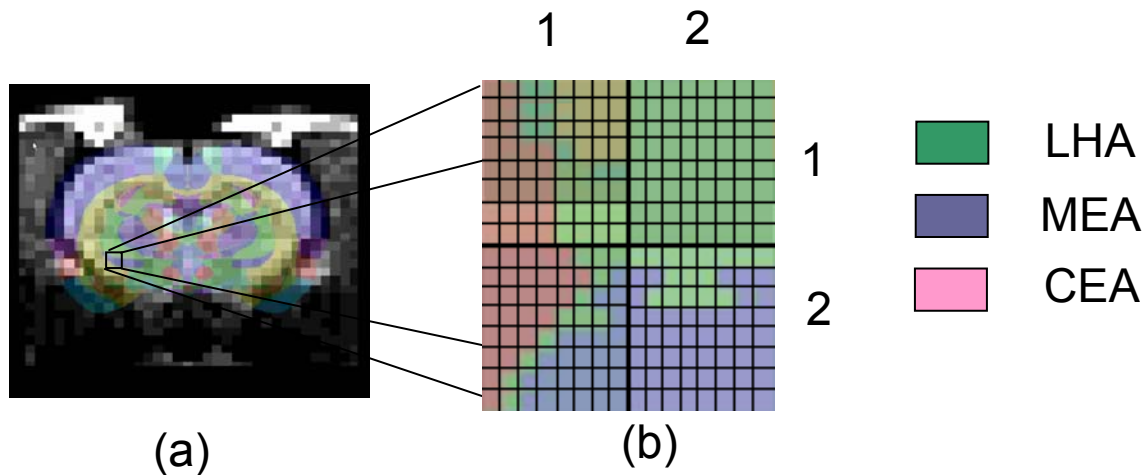


Figure 4.6: Show fMRI data registered to a segmented rat atlas. A magnified 2x2 pixel region of the fMRI data shows that the problem is one of classifying each fMRI voxel with that material from the higher resolution dataset that best approximates the voxel space.

4.4.2 Integrated volume approach [30]

Classifying voxel solely on its centroid location within the atlas can be misleading. As shown in figure 4.6 (b), quadrant 1, 2 (column, row) may get classified as LHA though it contributes very small area of voxel as compared to CEA and MEA. The algorithm was improved upon by classifying the functional pixel based on the integrated volume of the atlas space voxels occupying the single functional voxel space. In this approach, we march through all atlas voxels within each subject voxel and assign to that subject voxel, the atlas material that occurs with the greatest frequency within the functional voxel. This process is repeated for all subject voxels.

The algorithm was implemented and a typical mapped slice obtained from a 512*512*73 resolution rat atlas [14] and a 64*64*12 type functional MR dataset with the cerebrum and the amygdaloid complex as Regions Of Interest (ROI) are shown in Figures 4.7. For this dataset more than 700 functional pixels would have changed their classification between the centroid and majority volume strategies.

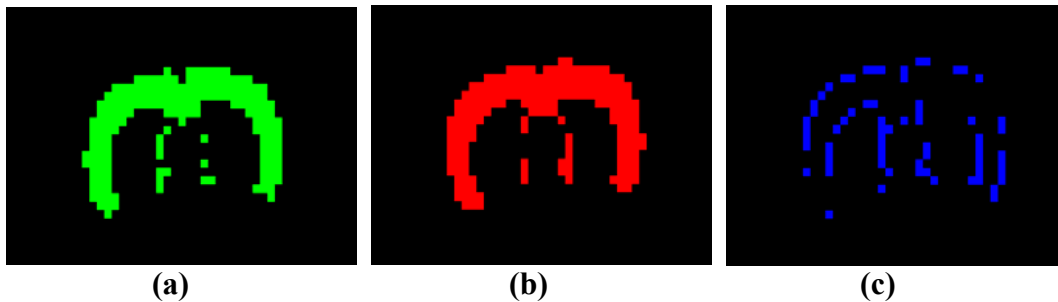


Figure 4.7: a) Subject voxels classified based on atlas material located at the centroid of MRI subject voxel. b) Improved algorithm based on material with greatest frequency of occurrence within subject voxel. c) XOR operation on Figures a and b to contrast the two methods. Note that a significant number of pixels have been reclassified.

4.5 Statistical Analysis of BOLD data

The statistical analysis of BOLD data is a critical part of brain mapping using fMRI. Many creative statistical methods have been proposed and there has been considerable debate about which is the “correct” approach. Given the flexibility of fMRI and the range of experiments that is possible, it seems likely that numerous statistical approaches can be applied to yield useful data. Although it is possible to devise many different techniques for detecting activation, if these techniques are to be used in practice it is necessary to know how much confidence can be placed in the results. That is to say, what is the probability that a purely random response could be falsely labeled as activation? This requires an understanding of the statistics behind the technique used. The

goal of this section is to highlight some of the important statistical analysis enhancements developed in this work.[33, 34]

4.5.1 Understanding fMRI data

fMRI is four dimensional data set; three spatial dimensions and time.

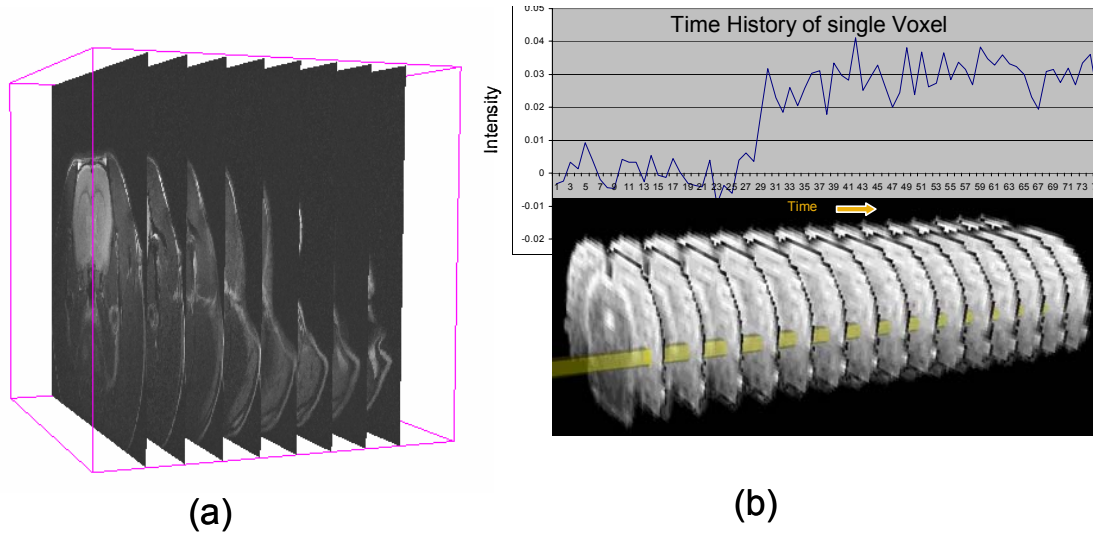


Figure 4.8: a) three dimensional MR image slices. b) bottom image is single slice collected at different time points and top image is plot of intensity of one voxel in time.

Figure 4.8 (a) shows multiple slices through rat brain in axial direction also called as three dimensional (3D) data or 3D volume. If we collect such multiple 3D volumes at specific time interval then we have four dimensional (4D) data. If we consider one voxel of this 4D data and march in time then we can plot time history of that voxel as shown in Figure 4.8 (b). Analysis of functional MRI data implies analysis of this time series. The test of activation can differ based on design paradigm of an experiment. A single epoch related design can be tested by student's t-test where as multiple epoch or repetitive event design can be tested by various regression analyses.

4.5.2 fMRI experimental Design

fMRI experiment design can be defined as guideline of controlling the timing and quality of presented stimuli to influence resulting brain processes. The goal of experimental design is

- To maximize the ability to test hypothesis.
- If possible to facilitate generation of new hypothesis.

Based on timing of presented stimuli the BOLD experiment design can be categorized in to two types.

- Block design.
- Event related design.

4.5.2.1 Block Design

Block design segregates different cognitive processes into distinct time periods. Many of the first proof-of-concept fMRI experiments were block designs with two conditions. In a block design, each condition is presented continuously for a period of few seconds (usually 6 to 20 seconds). In the earliest fMRI studies (Kwong et al [8], and Ogawa et al [9]), one common paradigm was to alternate between 60 second blocks of a flickering visual stimulus, and blocks without stimulation. In addition to comparing "on" versus "off" conditions, block designs have been used to look at differences between more similar conditions as well. Kanwisher et al. [31, 32]) has used block paradigms where the subject is presented with blocks of pictures of faces and blocks of pictures of houses to probe high-level features of the visual system.

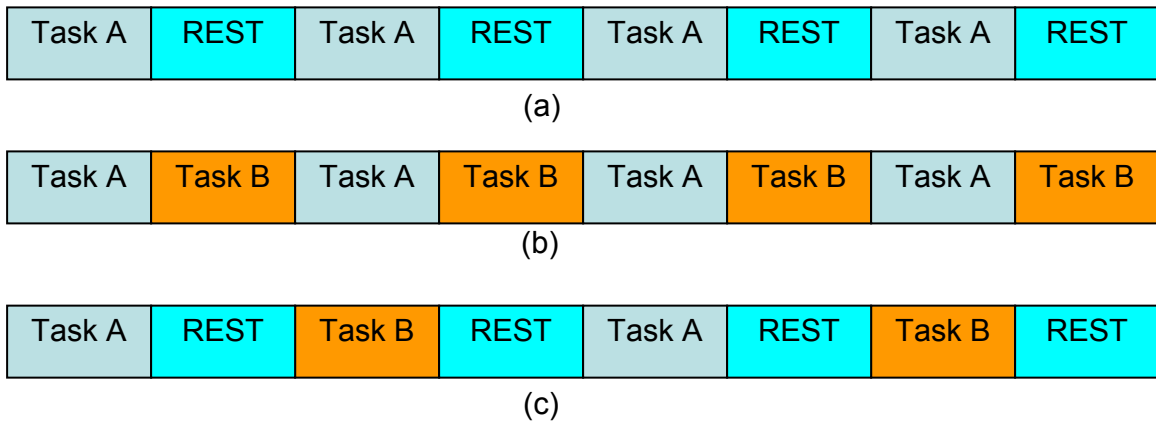


Figure 4.9 Typical types of block designs.

These block designs tend to be quite powerful for assessing BOLD signal magnitude differences between conditions. The length of the blocks of stimulation allows for the hemodynamic response function (HRF) to reach maximal values, while the inter-stimulus intervals are long enough for the HRF to return completely to baseline during non-stimulation. The downside of block designs is that they are not powerful at estimating the shape of the hemodynamic response (aside from its magnitude).

Block design is useful when testing for visual, tactile, and electrical type of stimulus where stimulation can be turned on and off frequently. But it is not as useful with many experimental paradigms having special requirements, such as odor stimulus, IV drug administration [33, 34] or some complex stimulus used to study emotions. In these experiments event related design serves the purpose.

4.5.2.2 Event Related design (single epoch)

The traditional block design that has multiple epochs of stimulation yields strong statistical power, yet it is susceptible to subjective psychophysical/psychological variability arising from sensitization, habituation, interstimulus interaction, and

predictability due to repeating cycles of stimulus presentation [84]. Event-related fMRI designs can minimize some of these factors, especially those due to predictability. In other words for block design we assume that the BOLD effect remains constant across the epoch of interest, but the BOLD response is much more transient and more importantly may vary according brain regions and stimulus duration and may be stimulus type. The typical event related design has one control period followed by stimulation period. Figure 4.10 shows block diagram of single epoch event related design paradigm.

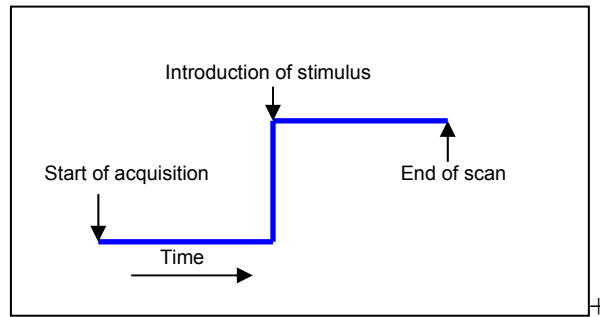


Figure 4.10: Block diagram of single epoch event related design paradigm.

4.5.3 Data Analysis

The magnetic resonance signal changes during activation due to BOLD effect are quite small. For rats about 400 μ m voxel size BOLD signal change is about 1% to 4%. With fast spin echo sequence, the intrinsic signal to noise ratio is in the range of 40 to 60; but this is still not large enough to reliably detect 1% signal change in a voxel from a single image in a stimulus state and single image in control state. For this reason a large number of images are required to allow sufficient averaging to detect the small signal changes. In general we want to be able to detect activation that are not apparent to the eye but that are nevertheless statistically significant.

4.5.3.1 Subtraction technique

The most obvious processing strategy to identify activated voxels would be simply subtracting the averages of all images made during the control task from the averages of all the images made during the stimulus task. If the signal variations due to the noise are random with the normal distribution and independent of each time point, this averaging will improve the SNR and should provide a map of activated areas. However this naive approach to data processing does not work well and in practice the data processing can become quite bit more involved.

The first problem with simple averaging is that the standard deviation of the noise is different in different voxels so that noise is not uniform across the image plane. The noise that adds into a signal at a particular voxel has two sources: random thermal noise and physiological fluctuations. The random thermal noise arises primarily from stray currents in the body that induce random signals in the receiver coil. This thermal noise is spread through the raw acquired data, and when the image is reconstructed, the noise is spread throughout the voxels of the image. The result is that this thermal noise can be accurately described as uniform random Gaussian noise, with the noise in each voxel having the same standard deviation and independent of the noise in other voxels. If this thermal noise was only source of fluctuation in the MR signal, the noise would have no spatial structure. But, in fact, the variance of signal over time measured exhibits temporal and spatial structure [35, 36, 37].

The additional variation of MR signal in vivo is attributed to physiological fluctuations, which include several effects. Cardiac pulsation creates a pressure wave that strongly affects the signal of flowing blood, but it also creates pulsations CSF and in

the brain parenchyma. Although these motions are small they nevertheless can produce signal fluctuations.

Another physiological fluctuation is due to respiration. Rats, unlike humans, have very high heart rates (300 /min) and respiration rates (80 /min). FSE imaging technique usually collects one transient volume set consisting of 64X64X12 pixels over the course of 6 seconds. This single collection period has about 30 heart beats and 8 respiration cycles that can cause signal variations. There are also true low frequency variations that could result from drifts due to scanner hardware and that may include additional physiological pulsations. ([36] PP :447)

4.5.3.2 Student's t-test

This analysis technique is used for event related design. One of the standard statistical parameters used to quantify the quality of measured activation is the t-statistic. The signal measured from particular voxel is treated as samples of two populations, control and stimulus, and we want to know whether stimulus made a difference? Our first thought is to ask how many standard deviations one sample mean is from the other. This number does relate to the strength or importance of a difference of means. However, by itself, it says nothing about whether the difference is statistically significant.

A quantity that measures the significance of a difference of means is not the number of standard deviations that they are apart, but the number of so called standard errors that they are apart. The standard error of a set of values measures the accuracy with which the sample mean estimates the true (population) mean. Typically the standard error is equal to the samples standard deviation divided by the square root of the number points in the sample.

When two distributions have thought to have same variance but possibly different means then a students t-test is computed as follows: First estimate the standard error of the difference of means, s_D , from the pooled variance by the formula [85]

$$s_D = \sqrt{\frac{\sum_{i \in A} (x_i - \bar{x}_A)^2 + \sum_{i \in B} (x_i - \bar{x}_B)^2}{N_A + N_B - 2} \left(\frac{1}{N_A} + \frac{1}{N_B} \right)}. \quad (4.25)$$

Where each sum is over the point in one sample, the first or second , each mean like wise refers to one sample or the other and N_A and N_B are the number of points in the first and second samples, respectively. Second compute t by

$$t = \frac{\bar{x}_A - \bar{x}_B}{s_D} \quad (4.26)$$

Third evaluate the significance of this value of t for Student's distribution with $(N_A + N_B - 2)$ degrees of freedom. $A(t/\nu)$ is the probability ,for ν degrees of freedom that a certain statistic is smaller than the observed value. Two means are significantly different if $A(t/\nu) > 0.99$. In other words, $1 - A(t/\nu)$ is the significance level at which the hypothesis that the means are equal is disproved.

$$A(t/\nu) = \frac{i}{v^2 B\left(\frac{1}{2}, \frac{\nu}{2}\right)} \int_{-t}^t \left(1 + \frac{x^2}{\nu}\right)^{-\frac{\nu+1}{2}} d_x \quad (4.27)$$

Limiting values are

$$A(0/\nu) = 0 \quad A(\infty/\nu) = 1$$

$A(t/\nu)$ is related to incomplete beta function $I_a(a, b)$ by

$$A(t/\nu) = 1 - I_{\frac{\nu}{\nu+t^2}}\left(\frac{\nu}{2}, \frac{1}{2}\right) \quad (4.28)$$

The significance is between zero and one and is the probability that $|t|$ could be as large or larger just by chance, for distribution with equal means. Therefore a small numerical value ($\alpha = 0.05$ or 0.01) of the significance means that the observed difference is very significant.

As describes earlier due to noise the variance in control and stimulus period may not be the same hence a more conservative approach uses a heteroscedastic variance t-test.

$$t = \frac{\bar{x}_A - \bar{x}_B}{[Var(x_A)/N_A + Var(x_B)/N_B]^{1/2}} \quad (4.29)$$

This statistics is distributed approximately at student's t with the number of degrees of freedom equal to

$$v = \frac{\left[\frac{Var(x_A)}{N_A} + \frac{Var(x_B)}{N_B} \right]^2}{\frac{[Var(x_A)/N_A]^2}{N_A - 1} + \frac{[Var(x_B)/N_B]^2}{N_B - 1}} \quad (4.30)$$

4.5.3.3 Correlation technique

This data analysis technique is use for block design. Since the BOLD response is mediated by blood flow, it is possible to improve the detection of activations by predicting the shape of the response to the stimulus, and calculating correlation coefficients between each pixel time course and this reference waveform.[96, 97] This analysis is less sensitive to other physiological changes during the experiment, and to movement. For a time course X, and a reference waveform Y, the correlation coefficient is calculated as

$$cc = \frac{\sum (X - \bar{X})(Y - \bar{Y})}{\sqrt{\sum (X - \bar{X})^2 \sum (Y - \bar{Y})^2}} \quad (4.31)$$

and has a value of 1 for perfect correlation, a value of zero for no correlation, and a value of -1 for perfect anti-correlation.

The choice of an appropriate reference waveform is vital for the success of this technique in finding activations. The first approximation might be a square wave, which is high for scans acquired during the task, and low for scans acquired during rest (Figure 4.11 (a)). Such a waveform however takes no account of the delay and smoothness of the hemodynamic response which regulates the BOLD contrast. An improvement to this would be to change the phase of the square wave (Figure 4.11 (b)), with a time delay appropriate for the species being tested, perhaps a delay between 3 and 6 seconds for humans.[92, 93, 94]

To improve the reference waveform further, it is necessary to look more closely at the actual hemodynamic response. Say, figure 4.11(c) is the actual time series from single voxel or ROI and correlation coefficients are calculated between these waveform and that of every other pixel in the image. Such an analysis detects only those regions in the brain which respond to the stimulus [96, 97]. The major disadvantage of this technique is that it is particularly sensitive to motion artifact, since if such artifact is present in the reference waveform then the movement of other regions will be highly correlated. The reference waveform is then made up of a repetition of these single cycle average responses (Figure 4.11(d)).

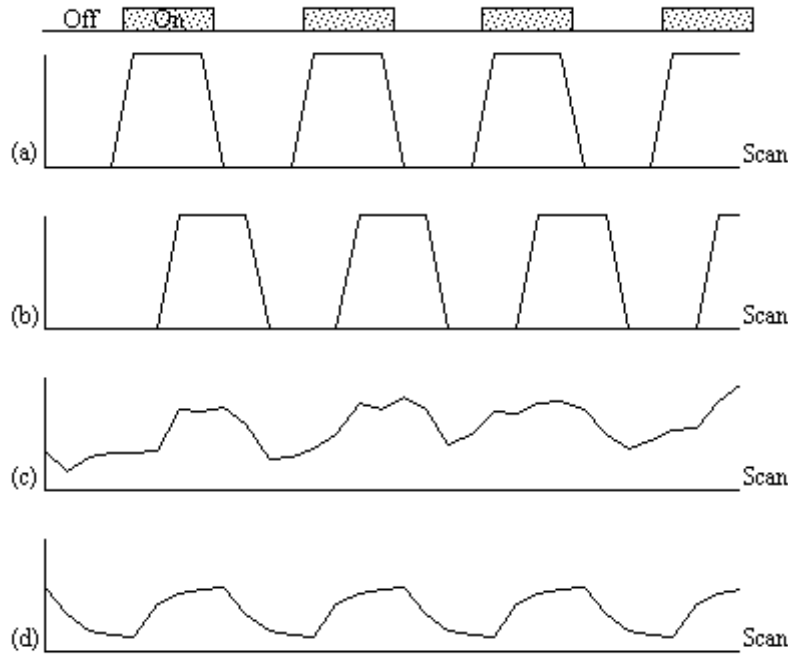


Figure 4.11: Various reference functions that can be used to correlate with a pixel time course to detect activations. [97]

To be more general in predicting the hemodynamic response, so that a reference waveform can be constructed for any length of stimulus, it is necessary to know the response to a single stimulus. Friston [37] suggested that a hemodynamic response function could be considered as a point spread function, which smoothes and shifts the input function. By deconvolving the response from a known area of activation with the stimulus function, the hemodynamic response function can be obtained. The hemodynamic response function is not completely uniform across the entire brain however, and the shape obtained from one region may not be optimum for another. As an alternative, the response can be modeled by a mathematical function, such as a beta function.[97]

$$B(z, w) = \int_0^1 t^{z-1} (1-t)^{w-1} dt = \frac{\Gamma(z)\Gamma(w)}{\Gamma(z+w)} \quad (4.32)$$

Since in general each slice of the volume imaged is not acquired at the same instant, it is necessary to accommodate timing differences in the correlation with the reference waveform. In order to do this, the relative magnitude of the activation at the time each slice was acquired is predicted, by convolving the input stimulus with a Poisson function. Then from this series, the correlation coefficients can be calculated on a slice by slice basis, constructing the reference waveform from the appropriate points in the predicted time series.

4.5.3.4 General Linear Model [99]

This technique is used for block design or box car design.[86, 87, 88 89, 90, 91] The aim of the general linear model is to explain the variation of the time course $y_1 \dots y_i \dots y_n$, in terms of a linear combination of explanatory variables and an error term. For a simple model with only one explanatory variable $x_1 \dots x_i \dots x_n$, the general linear model can be written

$$y_i = x_i b + e_i \quad (4.32)$$

where b is the scaling, or slope parameter, and e_i is the error term. If the model includes more variables it is convenient to write the general linear model in matrix form

$$Y = X\beta + \varepsilon \quad (4.33)$$

where now Y is the vector of observed pixel values, β is the vector of parameters and ε is the vector of error terms. The matrix X is known as the design matrix. It has one row for every time point in the original data, and one column for every explanatory variable in the model. In analyzing an fMRI experiment, the columns of X contain vectors corresponding to the 'on' and 'off' elements of the stimulus presented. By finding the

magnitude of the parameter in β corresponding to these vectors, the presence or absence of activation can be detected.

β can be determined by solving the 'normal equations'

$$X^T Y = (X^T X) \hat{\beta} \quad (4.34)$$

where $\hat{\beta}$ is the best linear estimate of β . Provided that $(X^T X)$ is invertible then $\hat{\beta}$ is given by

$$\hat{\beta} = (X^T X)^{-1} X^T Y \quad (4.35)$$

Such parameter estimates are normally distributed, and since the error term can be determined, statistical inference can be made as to whether the β parameter corresponding to the model of an activation response is significantly different from the null hypothesis.

The general linear model provides a framework for most kinds of modeling of the data, and can eliminate effects that may confound the analysis, such as drift or respiration, provided that they can be modeled. For example, a contrast agent introduced in the blood in fMRI experiment enhances signal to noise ratio. The kidneys filter the contrast agent out causing a loss of signal, over time. This situation can be modeled by introducing a linear or cubic term in GLM.

4.6 Multiple Comparison

The statistical tests discussed in section 4.5.3, to identify active voxels, are voxelwise hypothesis tests. At each voxel test statistics are computed from the data, usually related to null hypothesis of no difference between specified experimental conditions (control and stimulation period). The voxels which exceed the test statistics threshold are

classified as active. When one uses multiple tests or multiple comparison, as usually is the case with fMRI data, the probability that there will be false positive (or/and false negative) among all the tests become very evident. For example in a typical rat brain data set ($64 \times 64 \times 12$) approximately 4000 voxels represent brain area. At 95% confidence level ($\alpha = 0.05$) approximately 200 voxels will be classified as active voxels just by chance. Thus 5% error rate leads to a large number of false positives in absolute terms, especially relative to the typical number of true positives.

4.6.1 Bonferroni correction

There are a variety of methods available for controlling the false positives when performing multiple tests. Among the methods the most commonly used for multiple comparison is the Bonferroni correction. If there are k tests being performed, the Bonferroni correction replaces the nominal significance level α with the (α/k) for each test. So in the above example for 4000 voxels the significance level would be

$$(\alpha/k = 0.05/4000 = 1.25E - 04).$$

This is a very conservative condition and in practice the Bonferroni correction has tendency to wipe out both false and true positives when applied to entire fMRI data set.

To get useful results it is necessary to use more complicated method or to reduce number of tests considered simultaneously. For instance one could identify regions of interest (ROI) and apply the correction separately within each region. But as ROI size changes the result would change and analysis would loose its consistency.

4.6.2 False discovery rate

In typical functional magnetic resonance imaging data analysis a voxel is declared active if corresponding test statistics is sufficiently extreme with respect to statistics distribution under the null hypothesis. Let V denote the total number of voxels being tested in analysis. Each voxel can be classified into one of four types, depending on whether or not voxel is truly active and whether or not it is declared active as shown in Table 4.1.

	Declared active	Declared inactive	
Truly active	V_{aa}	V_{ai}	T_a
Truly inactive	V_{ia}	V_{ii}	T_i
	D_a	D_i	V

Table 4.1 Classification of voxels in V simultaneous tests.

In above table V_{ia} denotes the number of false positive and $D_a = V_{aa} + V_{ia}$ denotes number of voxels declared active. In any data analysis we only observe D_a , D_i and V ; the remaining counts are unknown. The FDR is given by ratio

$$FDR = \frac{V_{ia}}{V_{ia} + V_{aa}} = \frac{V_{ia}}{D_a}; \quad (4.36)$$

that is proportion of declared active voxels which are false positive. If none of the test is rejected the FDR is defined to be 0.

A procedure controlling the FDR specifies a rate q between 0 and 1 and ensures that “on average” the FDR is no bigger than q . This works even though V_{ia} , the number of false positives, is unknown.[38] The phrase “on average” here is important to the interpretation of the procedure. The guarantee is that if one were to replicate the

experiment many times, then the average FDR over those replications would be no bigger than q . For any particular data analysis, the actual FDR might be larger than q .

The FDR-controlling techniques introduced by Benjamini and Hochberg (1995) [39] are easily implemented, even for very large data sets. These procedures guarantee control of the FDR in the sense that

$$E(FDR) \leq \frac{T_i}{V} q \leq q, \quad (4.37)$$

Where E denotes expected value and where the first inequality is an equality when the P values are obtained from a continuous distribution. The unknown factor $\frac{T_i}{V}$, the proportion of truly inactive voxels, shows that the procedure somewhat over controls the expected FDR. In analyses of the entire data set, this factor will in practice be very close to 1 and can reasonably be ignored [38, 95].

For the V voxels being tested, the general procedure is as follows:

1. Select a desired FDR bound q between 0 and 1. This is the maximum FDR that the researcher is willing to tolerate on average.
2. Order the P values from smallest to largest: $P_{(1)} \leq P_{(2)} \leq P_{(3)} \dots \leq P_{(v)}$

Let i be the voxel corresponding to P value $P_{(i)}$.

3. Let r be the largest i for which

$$P_{(i)} \leq \frac{i}{V} \frac{q}{c(V)}, \quad (4.38)$$

where $c(V)$ is a predetermined constant described below.

4. Declare the voxels $V_{(i)}, \dots, V_{(r)}$ active, or in other words, threshold the image of test statistics at the value corresponding to the P value $P_{(r)}$.

The choice of the constant $c(V)$ depends on assumptions about the joint distribution of the P values across voxels. In fMRI analysis of Rat brain $c(V)$ was set to unity which is appropriate for data containing Gaussian noise [38, 39, 95].

To implement the procedure, one must choose a value for the parameter q , but one strength of the method is that this is not an arbitrary choice. From equation 4.38, q has a meaningful and rigorous interpretation that can be relied on in selecting its value and that makes it comparable across studies. While it is common to set q to conventional levels for significance testing (e.g., 0.01–0.05), this is by no means required. For instance, values of q in the range of 0.10–0.20 are reasonable in many problems [38]. In MIVA fMRI module q value is set to 0.05.

Another advantage of this method is that it is adaptive, in the sense that the chosen thresholds are automatically adjusted to the strength of the signal. The researcher chooses a tolerable rate of false discoveries, and the specific thresholds are determined from the data. This solves the threshold selection problem automatically, even for multiple subjects: there is no need to find an arbitrary and *ad hoc* threshold that works for all subjects simultaneously or to use a complicated method of targeting the threshold to each subject.

5: fMRI Module in MIVA

Medical Image Visualization and Analysis (MIVA) software was developed by the Visualization and Data analysis lab at Center for Comparative Neuroimaging (CCNI), WPI [105]. As a part of this work the functional MRI (fMRI) data analysis suite was developed as one of the application modules in MIVA. fMRI module provides an intuitive graphical interface to analyze functional images. The module also provides an interface for preprocessing of images and post processing of results.

There are many commercial and freeware software packages available for MRI and fMRI data analysis, including SPM [101], AFNI[102], Brain Voyager[103], Stimulate [104] etc. All these software follow the same philosophy; one subject, one analysis. The MIVA fMRI module was designed to visualize synchronized changes in neuronal activity across multiple subjects and brain areas as functional neuro-anatomical circuits. The advancement of fMRI Module over other software can be summarized in following points.

1. A self-contained Rat Brain Atlas and ability to incorporate other atlases in the system.
2. Fast reliable registration algorithms.
3. Atlas based mapping mechanism.
4. Ability to handle multiple subjects simultaneously and provide composite response maps.
5. Ability to provide 3D surface model of response maps for visualization.

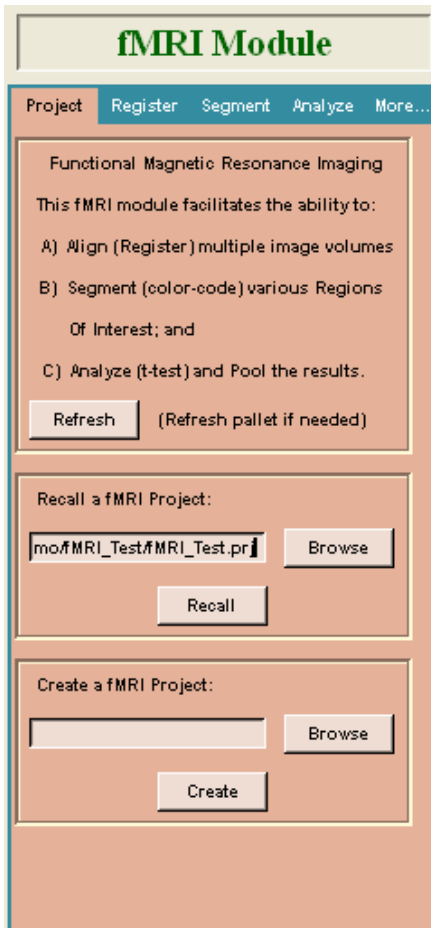


Figure 5.1: fMRI Module: Project

5.1 Project

The first tab in fMRI module is “Project”, that recalls or creates a project. This project module creates a folder named by the user. Within this folder the system maintains a ‘status’ file with the same name as the user specified Project Folder name with “.prj” extension. Several subfolders are created that are associated with each tab within the fMRI module. Data and results are stored within the project folder and subfolders. This module can be recalled and alternate or additional analyses can be performed. Figure 5.1 shows “Project” tab in fMRI Module.

Complete fMRI is a complicated and iterative analysis. This module walks one through the steps in sequence. These steps are not convoluted. This work presents multiple paths to obtain the final result. The fMRI module is divided into four components listed below. One can open fMRI module via “Application → fMRI” in menu bar.

1. Project
2. Registration
3. Segmentation
4. Analysis

Once the project is created the user must load Rat Atlas and anatomy images in that sequence. The rat atlas can be found in Atlas folder in MIVA core (default) directory. It is assumed that for all rats the anatomy images are precisely aligned to functional images. User must check alignment of functional and anatomy images prior to starting the project. If the anatomy image is not aligned to the functional image it must be aligned and resliced in functional space using reslice tab. The reslice operation is explained later in this chapter. Though the system is designed for any segmented image to be used as an atlas; fMRI module in this work is implemented and optimized for Rat Brain atlas.

5.2 Registration

MIVA offers several modes of registration: Manual, semiautomatic (4-point and N-point registration) and Automatic (AIR,). The goal of the registration process in fMRI analysis is to register all subjects to the atlas. As described in chapter 3 an atlas is a segmented image with pixel values ranging from 1 to 1277. At any location in the atlas the pixel value represents the anatomical area of rat brain. All the anatomical areas are listed alphabetically in Excel file based on their abbreviation in Swanson atlas [12]. There is no correlation between MRI anatomy pixel intensities and atlas pixel intensities. Consequently, all subjects are aligned to one standard subject taking advantage of intra-modality registration techniques. Then the single standard subject is registered to the atlas using fiducial registration techniques. Finally, the transformation matrices are combined to align all subjects to the atlas. That is:

- Intra Registration: One of the subjects was selected as ‘standard volume’. All other subjects are aligned to this standard subject using manual or an automated registration.
- Inter Registration: The standard subject is then aligned to ‘the atlas’ using manual or semiautomatic (4-point or N-Point registration) registration.
- Merge: Finally, all subjects are aligned to the Atlas based on the concatenated transformations that aligned each subject to a standard subject and the alignment of the standard subject to the atlas : Merge registration.

5.2.1 Intra Modality Registration

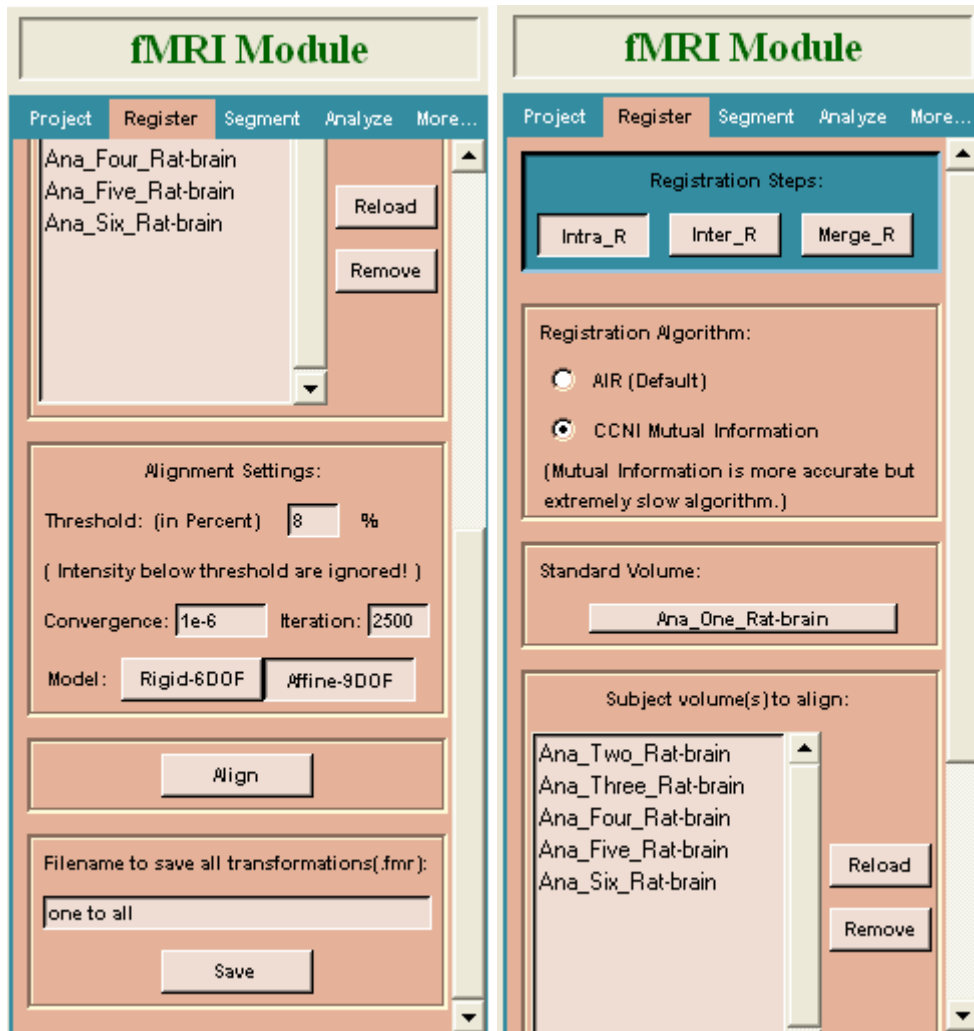


Figure 5.2: fMRI module: Intra-R registration Panel

As described in section 4.3.1 this component of the fMRI module deals with aligning all subjects to one subject. Select the 'Register' tab within the fMRI module. Press 'Intra-R' button (by default this button is pressed down when user first enters the 'Register' tab). There are two strategies for automatic intra-modality registration, 1) AIR (Automated Image Registration [19,20,21]) and 2) CCNI mutual information.

- 1) **AIR** : This strategy uses the AIR registration with several of the parameter options pre-selected. The code reads the Standard Volume set and defaults the Threshold to 8% of the data range. This value can be changed. Pixels with intensities below the threshold value are not used in the alignment process. The convergence (10^{-6}) and iteration count (2500) are our recommended values.
- 2) **CCNI Mutual Information** : This strategy aligns the subject to the reference image by maximizing the amount of mutual information. It essentially deforms the subject image based on the transformation constraints to minimize the intensity differences of the two images.

For both intra-modality registration strategies, select one subject as the ‘Standard Volume’. All other images, in MIVA’s memory are automatically loaded in the ‘Subject volume(s) to align:’ window. Any image not to be aligned can be removed. Highlight the undesired image and select ‘Remove’. The user can select two alignment strategies: ‘Rigid-6D0F’ or ‘Affine-9D0F’. The ‘Rigid-6D0F’ alignment rotates and translates the Subject Volumes to fit the Standard volume. However, it does not scale the image set. The ‘Affine-9D0F’ alignment also allows scaling in the 3 coordinates independently. An output file is specified to store all the transformations. The file extension ‘.fmr’ is automatically appended to the filename if an extension is absent. Similarly, a second file with the extension ‘.cni’ is created. The program uses the ‘.fmr’ file information for internal use. The ‘.cni’ file allows the user to resume the process at the same state.

The ‘Align’ button performs the registration. The subject volumes are distorted to fit the Standard volume. A $[T_j]$ matrix is created for each subject. Typical alignment time ranges are (1-5) minutes per subject for AIR and (7-8) minutes for CCNI mutual

information. These alignments are applied to the image volumes immediately. However, the user-specified output file will not be created until the ‘*Save*’ button is pressed. Prior to activating the ‘*Save*’ option, the user should inspect the quality of the alignments for each subject. Each subject volume ‘registration’ matrix was modified to fit the standard. The standard volume retains its ‘identity’ matrix. Under ‘Applications → Registration’ the user can select ‘*Active Matrix*’ and view its 4x4 values. The user can select ‘Tools → Slice Control’ and specify the background image to be the Standard volume and one of the Subject volumes as the foreground image. A variety of viewing tools exist to toggle the images, superimpose them, and alter the opacity of them. These can be used to verify the quality of the registration.

If the registration(s) are not acceptable, 3 general choices exist in order of preference: a) manually adjust the results, b) use the inter-registration alternative, or c) crop the images and redo Intra-Registration. Once the subject volumes are aligned satisfactorily to the standard volume the user specifies the output .fmr file name and selects the ‘*Save*’ button. This preserves the current status of the system and allows a clean restart of the project if desired, via the CNI file created.

AIR and CCNI mutual information are not the only two strategies for intra-modality registration. One can also register the data sets manually by going to ‘Applications → Registration’ or by any other mode. For the fMRI module to work smoothly, one still needs to create (Save) the final aligned image volumes. In this mode the ‘Align’ button is never used. The image volumes are still loaded in the ‘Subject(s) to align’ window and a reference image is specified in the ‘Standard Volume’ tab. Any

image volume not aligned yet can be aligned using tools other than the AIR option. The ‘Save’ button creates the necessary infrastructure to continue the fMRI module.

5.2.2 Inter-Modality Registration

One of the primary registrations is to align a subject to an atlas. This form of registration is inter-modality or fiducial registration since the subject volume is intensity based (grayscale) whereas the atlas is a segmented (or color-coded) image set.

We recommend as a 1st attempt the 4-point alignment. This strategy can be incredibly fast. The down side is that it requires closely matched points and spatial separation of the points. The ideal 4 points form an equilateral tetrahedron on one subject (the Standard subject) which will be mapped to the other volume image’s (the Atlas) equilateral tetrahedron. We recommend creating a triangle on one slice (the base of the tetrahedron) and a single center point on a distant slice (the tip of the tetrahedron) in the next section.

5.2.2.1 4-Point Fiducial Registration

At this stage of analysis user already has an atlas and anatomy images in the system, since user has already finished ‘Intra-R’ part of registration he has selected one of the images as standard volume. This standard volume is now automatically selected as subject volume and Rat Atlas is selected as reference volume in Inter-R registration (Figure 5.5). If the subject volume in Inter-R is not same as Standard volume in Intra-R then system will complain and would not allow registration.

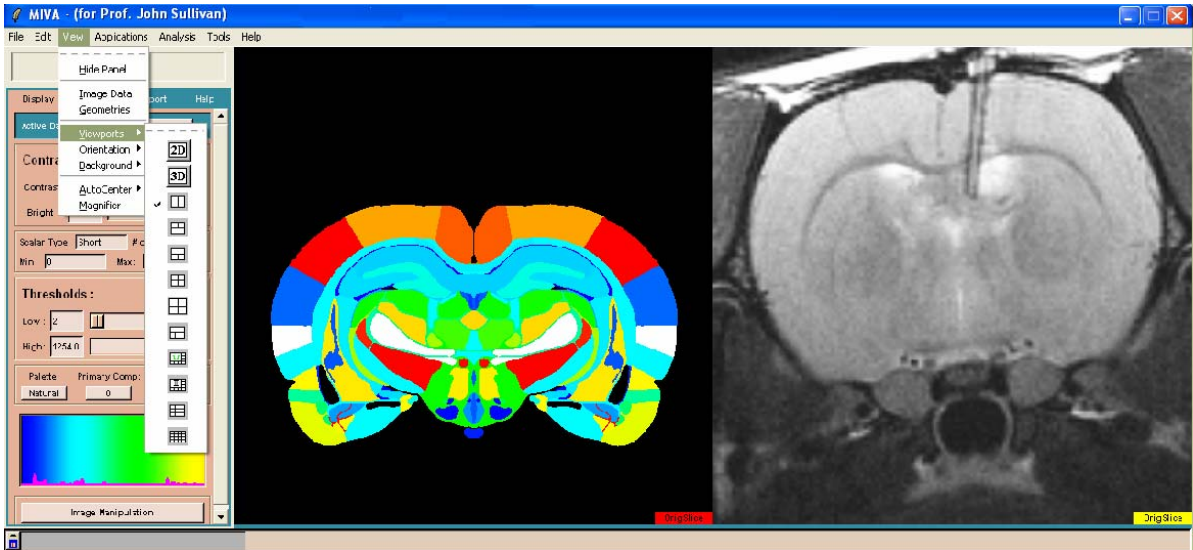


Figure 5.3: How to choose two panel view port and display atlas and standard image side by side.

Set the GUI view to be a 2 panel view and select one image set for each window as shown in figure 5.3. This setting provides ‘side-by-side’ image comparisons. One might need to adjust the orientation, such as axial view for each viewing pane. Under ‘Tools→Slice Control’ move the slide bar of each image set until the same distinct regions of the brain can be identified in each volume set. Preferably, select a slice towards one end of the brain. Ideally, we want to have 3 locations identified on this slice.

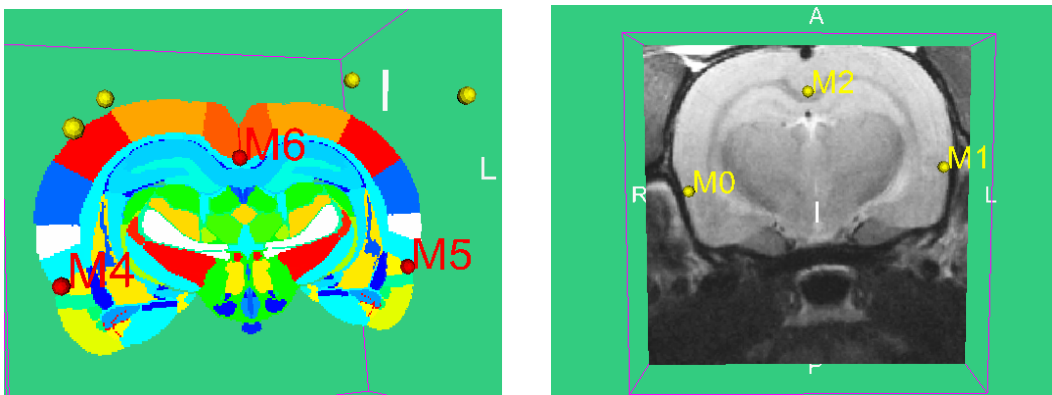


Figure 5.4: Markers created on Atlas image as well as on anatomy image.

Markers need to be created in both image sets. Select ‘Tools’ → ‘Marker’. Type in a new label for a group (eg. ‘standard’) and ‘Add’ this group. Select the ‘Create’

button and identify the 3 locations on the ‘Standard’ image set. The 3 target points are M0, M1, and M2, as shown in the Figure 5.4. The user must simultaneously hold down the ‘ctrl’ key and perform a left-mouse click to create each location. The ‘Markers’ do NOT show up on the 2D image. They are 3D geometries and their locations and labels are in the 3D window only. One can select a 2x2 view and turn on the visibility of the 2D slice in the 3D window to see the location of the 3 points relative to the image.

Repeat this process for the Rat Atlas. Be sure to create a new label (eg. Atlas) and ‘Add’ the group, then create markers at the **same** 3 locations in the **same** sequence on the Atlas; M4, M5, and M6, as shown in the Figure 5.4. If the sequence was not correct, one can move the point locations up and down in the ‘Marker’ application pallet. Ideally, one wants the 3 points on the plane to form an equilateral triangle that spans the 2D image slice. However, well identified and matched landmarks on the two image set slices are critical. A 4th point NOT in the same plane needs to be identified for both image sets. The 4th point is distant from this slice.

Two Marker sets have been created. Now to align the two image volumes based on these 4 paired points. Select ‘Inter-R’ tab within the fMRI application module. The graphics at the top of the panel indicate that the ‘Subject’ selection will be transformed to fit the ‘Reference’ space. There are two buttons in the ‘Reference Information’ area. Under the ‘Background Image’ and ‘Overlaid Marker Set’ columns, the user enters the Atlas and Standard Subject information. The third window displays the ‘Number of Points’ in the selected Marker set. A similar selection menu exists for the ‘Subject Information’ area. If more than 4 points exists in the Marker sets, the user can specify from 4 to N points for the transformation determination. For this example only 4 points

(the minimum) exist. Select ‘Get_T_Matrix’ button to determine the transformation matrix. The resultant 4x4 T matrix is displayed in the adjacent window. To verify that the transformation was sufficiently accurate, one needs to apply the matrix to the ‘Reference Image’ set. Select ‘Apply New Matrix’ and then sweep through the slices to check alignment. The effects of the transform are immediately apparent if the images are visible in the display windows. ‘Undo’ will revert to the previous matrix if selected. The marker points still exist. If the transformation is acceptable, the user supplies a name for this T matrix and selects ‘Save’. The default name concatenates the two selected volume labels with direction in the current folder, i.e. “Reference_To_Subject” (or Atlas-To_Subject for our example).

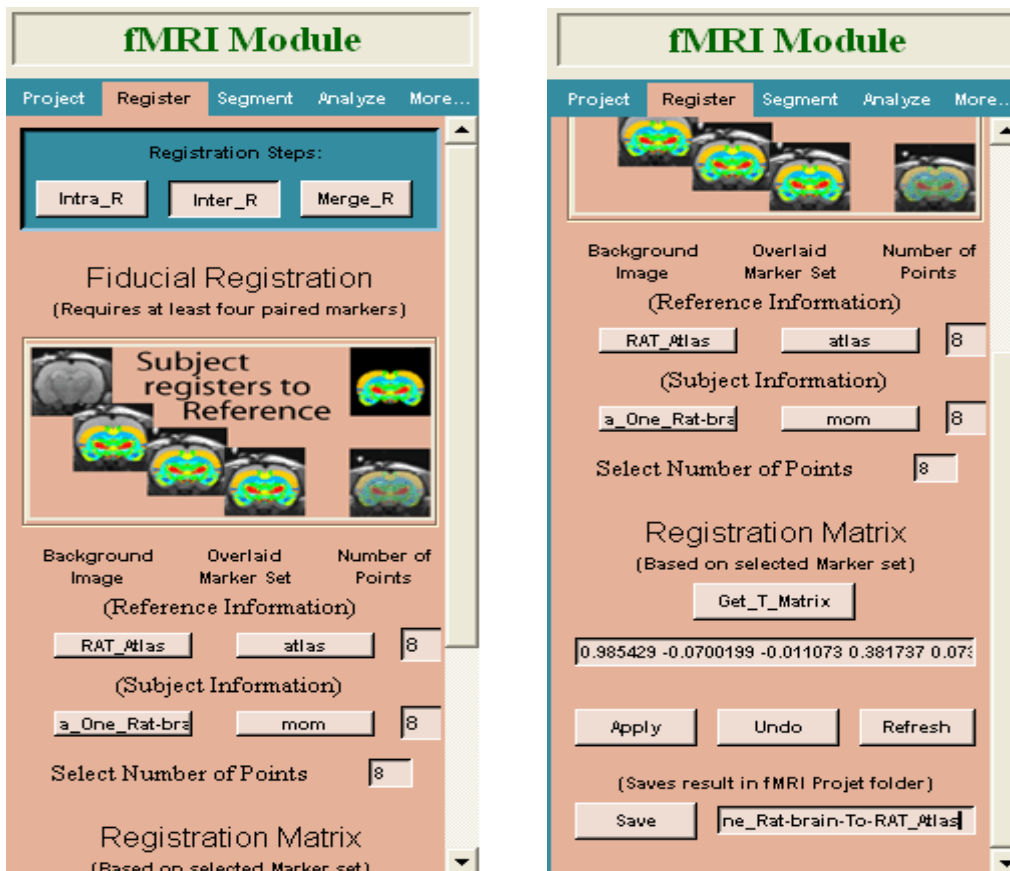


Figure 5.5: fMRI Module: Inter Registration Palate

5.2.2.2 N Point Fiducial Registration

If the 4-Point Inter-Registration results were less than desirable, one can perform ‘Manual’ registration to tweak the alignment. This tweak is usually performed within a few minutes. Alternately, one can use more points in the alignment process. The ‘Inter-Registration’ module displays the number of markers in each selected data set. Adjacent to the ‘Get_T_Matrix’ is a user-selectable marker-count entry. It defaults to the lower of the two selected marker counts. The user can enter any value between 4 and the default displayed, which has a ceiling at 10 markers. Adding more fiducial points can enhance the registration. The code performs a least-squared error analysis on all the paired points; complete mathematical derivation of this is described in section 4.2.2 . The downside is that it takes time to create and match locations on each image. The alignment algorithm is incredibly fast and does not create any bottleneck in the fMRI analysis process. From a user viewpoint there is no difference between the 4-point and N-point other than the number of points. However, the 4-point is a closed analytical solution as shown in Equation 4.8. The N-point registration minimizes the error of the point sets according to a least square minimization algorithm as shown in Equation 4.13.

5.2.3 Merge-Registration

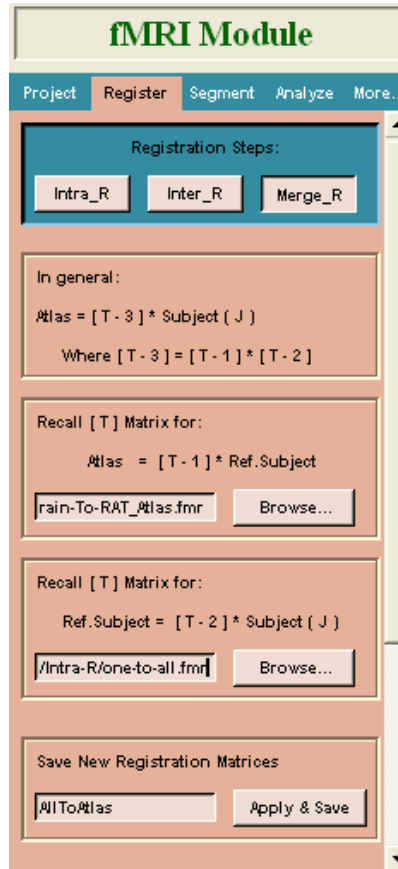


Figure 5.6: fMRI Module: Merge-R Palate

In ‘Intra-R’ all Subjects (2 to N) were aligned to fit Standard. In ‘Inter-R’ the standard was registered to fit the Atlas. Merge-Registration eliminates ‘Standard’ as the intermediary. The user recalls the file name saved within the Inter-R tab for the first Browse button. The program goes directly to that location by default. Similarly, the Intra-R saved file is recalled for the second Browse button. A new file is created that provides alignment of all subjects (that is Subject 1 through N) to the Atlas. The subject to atlas matrix is calculated as shown in equation 5.1.

$$\left[T_{Subject-to-Atlas} \right]_j = \left[T_{Standard-to-Atlas} \right] \left[T_{Subject-to-standard} \right]_j \quad (5.1)$$

5.3 Segmentation

A 3D atlas of the rat brain was created with a 'windows explorer' style tree browser. The tree browser allows one to select major (about 12) and/or minor (about 12 within each major region) anatomical regions interactively. Extensive work has also developed several functional 3D sub-volumes within the rat brain. Figure 5.7 displays this tree browser interface. The various ROIs are selected via the check boxes adjacent to the major or minor label. The entire shell of the rat brain is always selected to give relative position of anatomical areas with respect to whole brain. Once the desired Regions (or Volumes) of Interest have been selected and viewed (by pressing view button) for confirmation, the user saves the selections as *.roi file. If extension is not given then program appends '.roi' as an extension to filename. These regions or volumes of interest will be identified on each subject. The user needs to close the Tree-Browser and enter or select the file just saved from the tree browser. This allows user to create multiple roi files and use suitable one at a time.

The user selects the '*.fmr' file recently created within the Merge-R tab. The 'Run' tab color codes each anatomy image according to the VOIs identified for a fully segmented mask of each slice. A series of color-coded (or segmented) files are created. They are stored in the same folder as the anatomy files with a '_map' appended to each original anatomy filename. If the user is analyzing a single file that was aligned directly to the atlas, the '*.fmr' file within the Inter-R folder can be used to create the segmented map file.

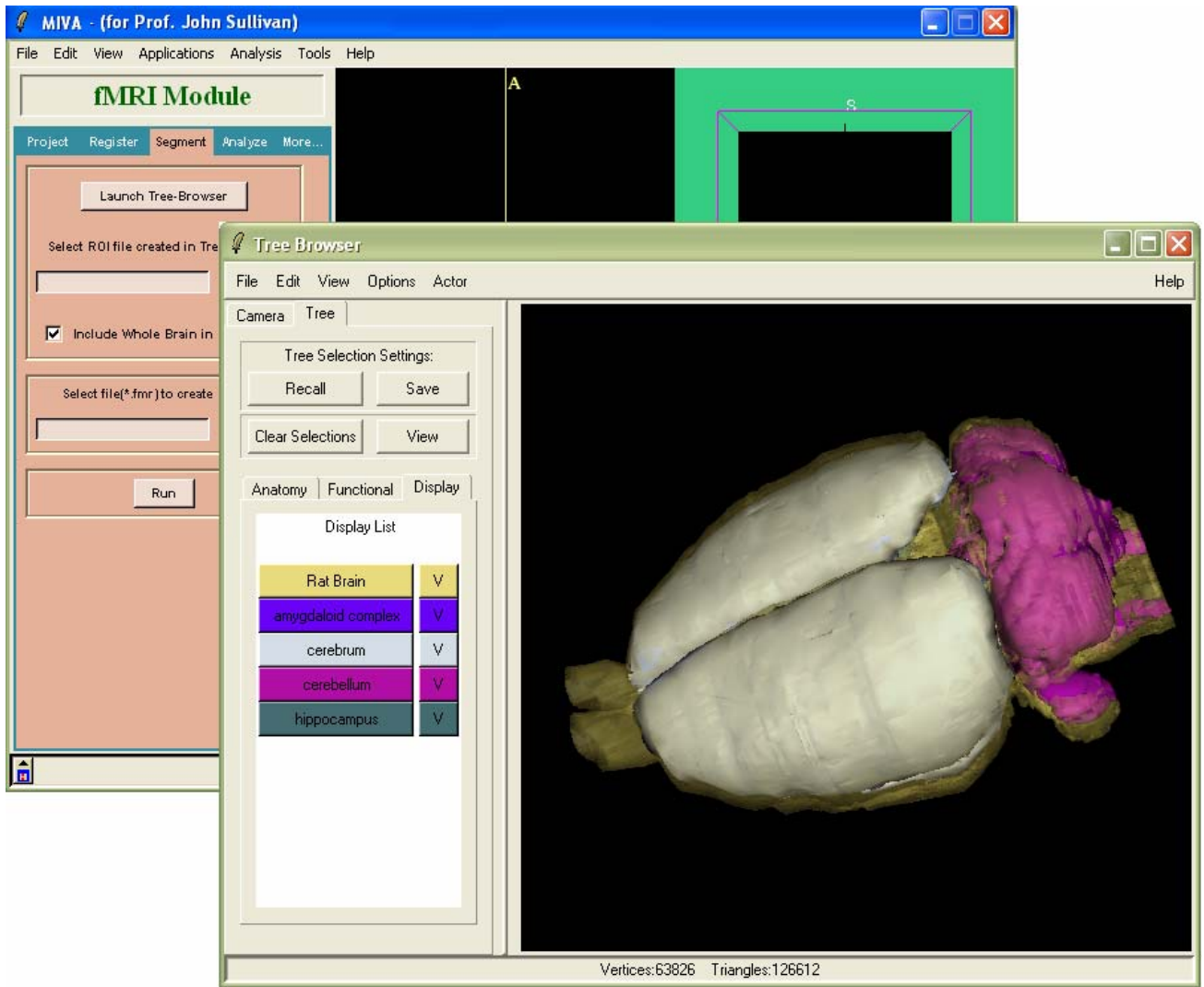


Figure 5.7: fMRI Module: Segmentation Palette.

5.4 T-test Analysis

The 'Analyze' module, by default, opens up the 'Load File' part of 'Analyze' tab. The module keeps track of all the subjects registered in Intra-R and Inter-R and their transformation matrices. The 'Update_File' button loads all subject anatomy files in the Anatomy Files window (Figure 5.8 a) and '*.map' files, created in segmentation section, in ROI masked File window (Figure 5.8 b). The user must manually 'Add' each

functional file to the functional Files window so that there is a one-to-one correspondence between anatomy image and functional image.

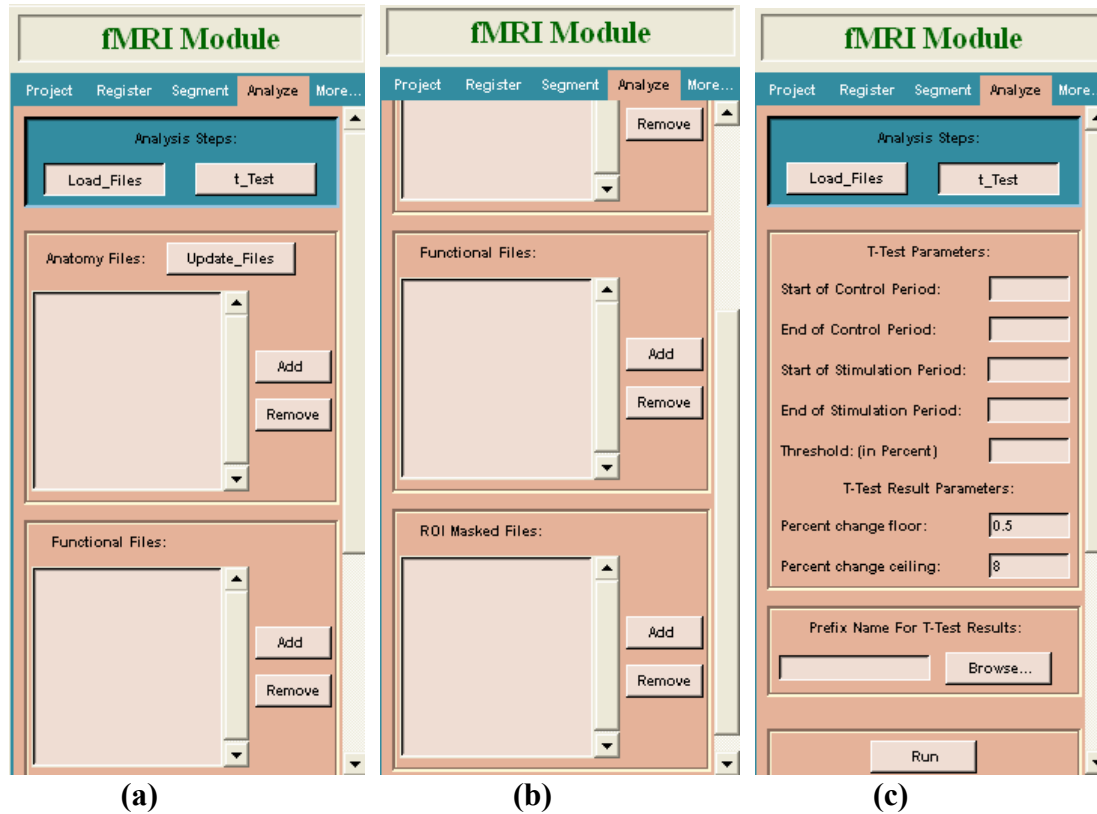


Figure 5.8: fMRI module: Analyze palate.

The t-Test button displays the various test parameters that need to be specified. The user enters these parameters based on the design of the experiment.

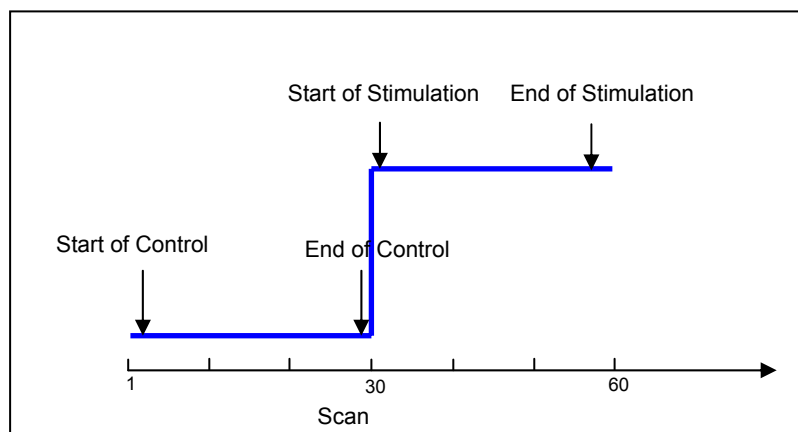


Figure 5.9: Design of fMRI experiment.

Figure 5.9 shows design of experiment and possible values for first four parameters. The Threshold value is statistical test confidence level and default value is 0.95 and can be changed to any value between 0 and 1. There are two other parameters user can set to filter noise from the signal; the percent change floor and ceiling. These two values are defaulted to 0.5% and 8%.

5.5 Results

The analysis results are presented in two forms: as an image for visualization and as a comma separated value (csv) files for numerical validation. The researcher usually wants to know;

- What were the responses of individual subjects?
- Which areas of the brain were activated?
- Did the stimulation affect different regions of the brain at different time?
- Finally it is important to know what the composite response from N subjects was.

The fMRI module outputs individual and composite image file (sdt/spr format) that has five components.

- 1) Positive Percent change for activated pixel.
- 2) Negative Percent change for activated pixels.
- 3) p values for activated pixels.
- 4) P values for all pixels in ROIs.
- 5) Percent change values for all Pixels in ROIs.

The composite statistics were built using the inverse transformation matrices. Each composite pixel location (i.e., row, column, and slice), pre-multiplied by $[T_i]^{-1}$, mapped it within a voxel of subject (i). A tri-linear interpolation of the subject's voxel

values (percentage change) determined the statistical contribution of subject (i) to the composite (row, column, and slice) location. The use of $[T_i]^{-1}$ ensured that the full volume set of the composite was populated with subject contributions. The average value from all subjects within the group determined the composite value. The BOLD response maps of the composite were somewhat broader in their spatial coverage than in an individual subject; so only average number of activated pixels that has highest composite percent change values in particular ROI was displayed in composite map. Activated composite pixels are calculated as follows:

$$Activated\ Composite\ Pixels\ ROI(j) = \frac{\sum_{i=1}^N Activated\ Pixels\ Subject(i)\ ROI(j)}{N}$$

The composite percent change for the time history graphs for each region was based on the weighted average of each subject, as follows:

$$Composite\ Percent\ Change = \frac{\sum_{i=1}^N Activated\ Pixel\ Subject(i) \times Percent\ Change(i)}{Activated\ Composite\ Pixels}$$

where N is number of subjects

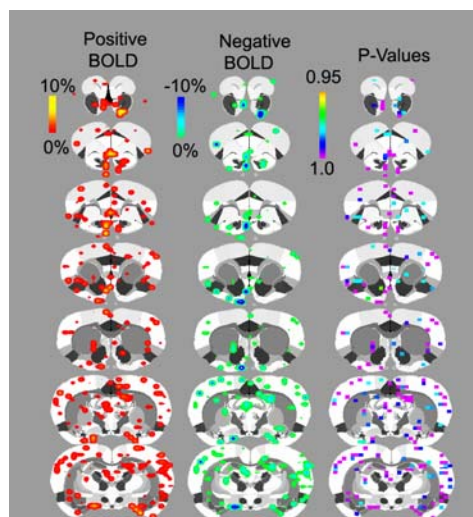


Figure 5.10: Positive, negative activation and p value map.

Figure 5.10 shows positive, negative percent change and p value maps on the on the foreground of Rat atlas. The images were created using MIVA and collage of different slices is created using Photoshop™ software.

The time history data of activation for each ROI was written in csv file besides the summary of all the subjects was written in summary file. Figure 5.11 shows the time history data in percent change and chart for one ROI.

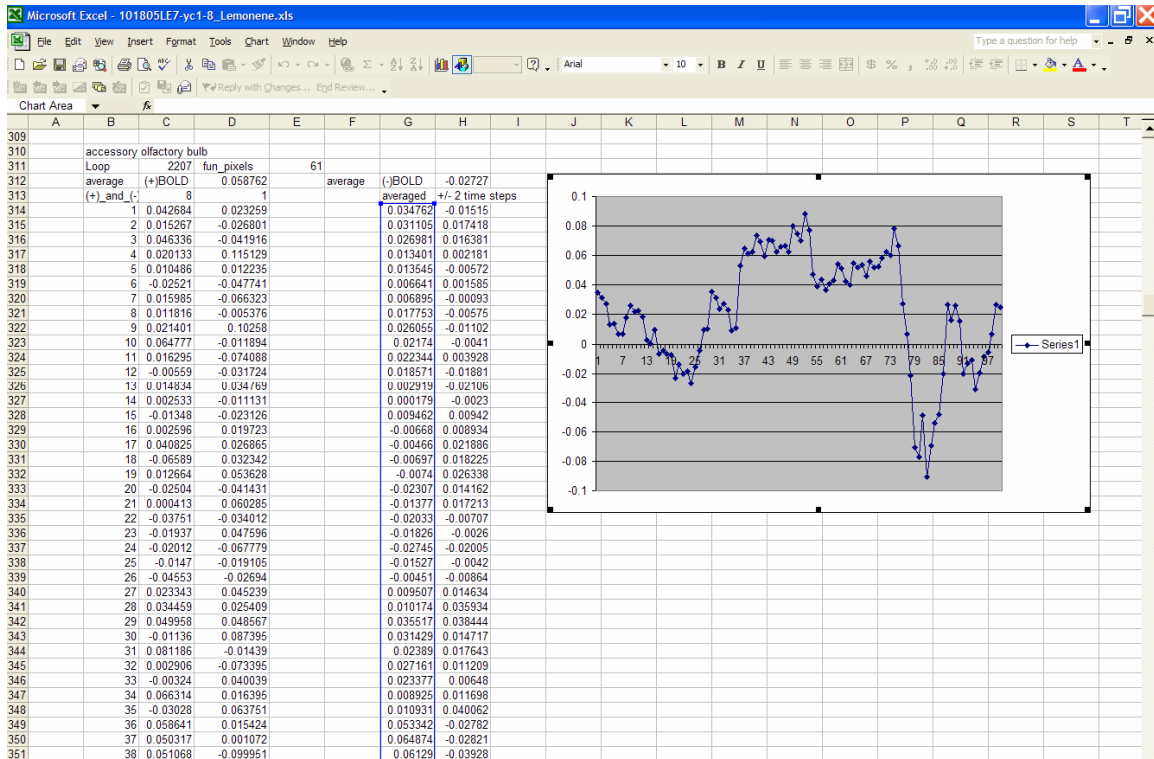


Figure 5.11: Time history chart of ROI.

Figure 5.12 shows the summary of all the subjects for each selected ROIs. The summary file

Microsoft Excel - LemoneneProject_summary.csv

File Edit View Insert Format Tools Data Window Help

100% Arial

	A	B	C	D	E	F	G	H	I	J	K	L	M	N
1		Summary of	Lemonene											
2														
3			30000		2089		2207		2071		2002		2068	
4			+ve voxels	-ve voxels	+ve voxels	-ve voxels	+ve voxels	-ve voxels	+ve voxels	-ve voxels	+ve voxels	-ve voxels	+ve voxels	-ve voxels
5														
6	101905LE2		166	146	4	6	4	2	2	1	0	0	0	0
7	101905LE3		608	65	18	5	12	0	7	1	7	0	1	1
8	101905LE4		45	164	3	4	3	0	2	0	0	3	0	0
9	102005LE4		175	1677	3	70	1	22	0	17	0	13	0	1
10	101805LE4		98	179	3	2	2	0	0	0	1	3	0	0
11	101805LE7		205	41	10	0	8	1	1	0	2	1	0	0
12	101805LE7		55	383	0	14	1	3	0	3	0	1	0	0
13	101805LE9		190	107	12	1	8	2	9	1	1	2	1	0
14	102005LE1		1327	1174	29	48	20	20	8	5	9	4	0	1
15	Average		318.7778	437.3333	9.111111	16.66667	6.555555	5.555555	3.222222	3.111111	2.222222	3	0.222222	0.333333
16														
17		Percent	BOLD	for	Lemonene									
18														
19			30000		2089		2207		2071		2002		2068	
20			+ve voxels	-ve voxels	+ve voxels	-ve voxels	+ve voxels	-ve voxels	+ve voxels	-ve voxels	+ve voxels	-ve voxels	+ve voxels	-ve voxels
21														
22	101905LE2		0.025625	-0.02167	0.032874	-0.03265	0.03382	-0.03064	0.022701	-0.02475	0	0	0	0
23	101905LE3		0.040772	-0.03642	0.066855	-0.07998	0.120515	0	0.130379	-0.04677	0.083214	0	0.248576	-0.03505
24	101905LE4		0.019467	-0.01874	0.022087	-0.02421	0.046935	0	0.017819	0	0	-0.01973	0	0
25	102005LE4		0.070899	-0.04079	0.111364	-0.061	0.110061	-0.05229	0	-0.0472	0	0	-0.0311	-0.02327
26	101805LE4		0.027575	-0.01769	0.021024	-0.03707	0.024289	0	0	0	0.013641	-0.01784	0	0
27	101805LE7		0.035626	-0.02737	0.041181	0	0.058762	-0.02727	0.050522	0	0.026908	-0.02096	0	0
28	101805LE9		0.026577	-0.0278	0	-0.05661	0.032832	-0.03319	0	-0.02778	0	-0.0208	0	0
29	101805LE9		0.032555	-0.02472	0.050539	-0.0773	0.038515	-0.048	0.033092	-0.03311	0.021831	-0.02371	0.030816	0
30	102005LE1		0.073477	-0.0794	0.061621	-0.09328	0.094317	-0.05438	0.039771	-0.04917	0.034471	-0.03317	0	-0.03074
31	Average		0.039175	-0.03273	0.045283	-0.05135	0.062227	-0.02731	0.032698	-0.02542	0.020007	-0.01859	0.031044	-0.0099
32														

Figure 5.12: The Composite data summary sheet

6: Mapping Olfactory System

In this work an fMRI module was developed as an analysis tool for mapping functional areas of the brain. This module provided an integrated system for neuroscientist that facilitated registration, segmentation, and statistical analysis of multiple subjects in one sweep. The self-contained atlas in this module provided a knowledgebase of anatomical areas of rat brain and facilitated automated mapping mechanism. The ability of the module to compute composite response maps and composite time-series provided great statistical resources for the analyses. The olfactory system of a rat was selected to demonstrate the effectiveness of this advanced medical visualization and analysis.

The rat olfactory system is important for reproductive [45, 46, 47]/maternal functions, neuroendocrine regulation, emotional responses, aggression, and the recognition of predators [48] and preys. Olfaction also plays critical role in food selection, as the perception and flavors results from the integration of olfactory and gustatory signals. The prepotency of olfactory stimuli in memory and control of animal behavior have long been recognized, yet the neural mechanism that underlie this phenomenon are poorly understood [6]. Investigation of these and other olfactory functions needs understanding of the neuronotomical and neurochemical organization of the olfactory system and it's linkage to other parts of the brain. Neurochemical organization involves understanding mechanism of odorant binding proteins, receptors, Ion-Protine channels, primary/secondary chemical messengers [40, 41, 42, 43, 44] and is out of scope of this work. The goal of this experiment is to study neuroanatomical

organization of olfactory stimulus using the fMRI techniques and modules developed in this dissertation. Before embarking on experimental methods let us take an overview of anatomical areas involved in olfaction.

6.1 Main Olfactory System

Air enters the rat's nostrils and flows past a patch of skin rich with smell receptors called the olfactory epithelium. Figure 6.1 shows section through nasal cavity of rat. Folded structures, the turbinates, serve to increase the surface and carry the olfactory epithelium. Here are olfactory neurons, which are tipped with little hair-like cilia that project into a thin bath of mucus at the cell surface. Odor particles in the air, called odorants, bind to special receptors on the cilia of the olfactory neurons, and their binding triggers a neural response that shoots up to the brain.

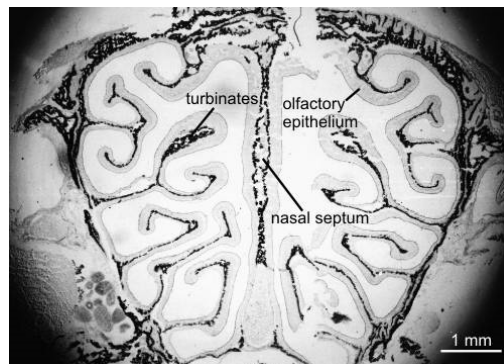


Figure 6.1: Section through the nasal cavity of a rat. [49]

Olfactory receptor cells are bipolar neurons. They send a single dendrite to the surface of the epithelium, where it ends in a knob. The knob gives rise to several fine processes, the olfactory cilia. The cilia are embedded in the mucus and cover the epithelium with a dense meshwork. The cilia are the site of sensory transduction. At their basal pole, olfactory neurons form an axon. Up to 1000 axons are clustered in bundles

that leave the nasal cavity through a thin bone to enter the adjacent olfactory bulb, a phylogenetically old region of the brain [6, 49].

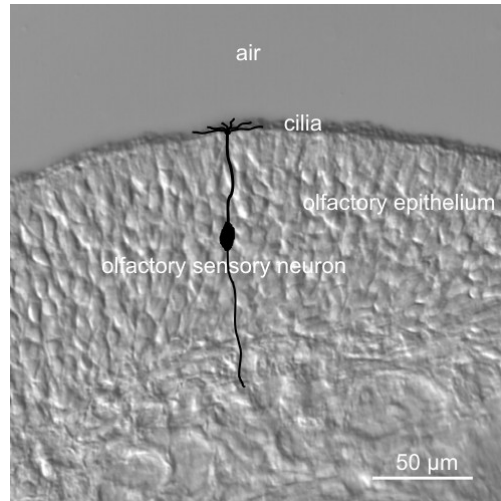


Figure 6.2: Olfactory epithelium of a rat with a schematic representation of an olfactory sensory neuron.[49]

In rats, two components of the olfactory system are recognized the main and accessory olfactory system. These two components are parallel, but are, for most part anatomically and functionally separate [6]. For example olfactory receptor neuron's (ORN's) in olfactory epithelium transduce mainly volatile odor and transmit this information to the main olfactory bulb (MOB). By contrast ORN's located in the vomeronasal organs are exposed to non volatile odors by engagement of physically regulated pump mechanism. Axons of the vomeronasal neurons projects exclusively to the accessory olfactory bulb (AOB) located at dorsocaudal limit of the MOB. In this study we will exclusively use volatile odorants to study main olfactory system. The main olfactory bulb (MOB) contains output neurons, mitral and tufted cells, which convey information to higher order olfactory structures and to other brain systems. The relay

from nose to the mitral and tufted cell is strongly regulated by local intrabulbar circuitry and by centrifugal inputs to the olfactory bulb from other parts of the brain. Higher order olfactory structures targeted by the mitral and tufted cells include, anterior olfactory nucleus, the piriform cortex, the olfactory tubercle and the entorhinal cortex. The MOB's projections to collections of above mentioned structures referred to collectively as primary olfactory cortex. Figure 6.3 shows 3D image of rat main olfactory system. This system of olfactory circuitry appears relatively simple, but this is not the case, there are number of critical gaps in our knowledge of olfaction that have prevented the kinds of integrative analysis of structure and function. Analyzing fMRI data with the described strategy can help fill some of these gaps since we can investigate each and every anatomical area at the same time during olfactory stimulus.

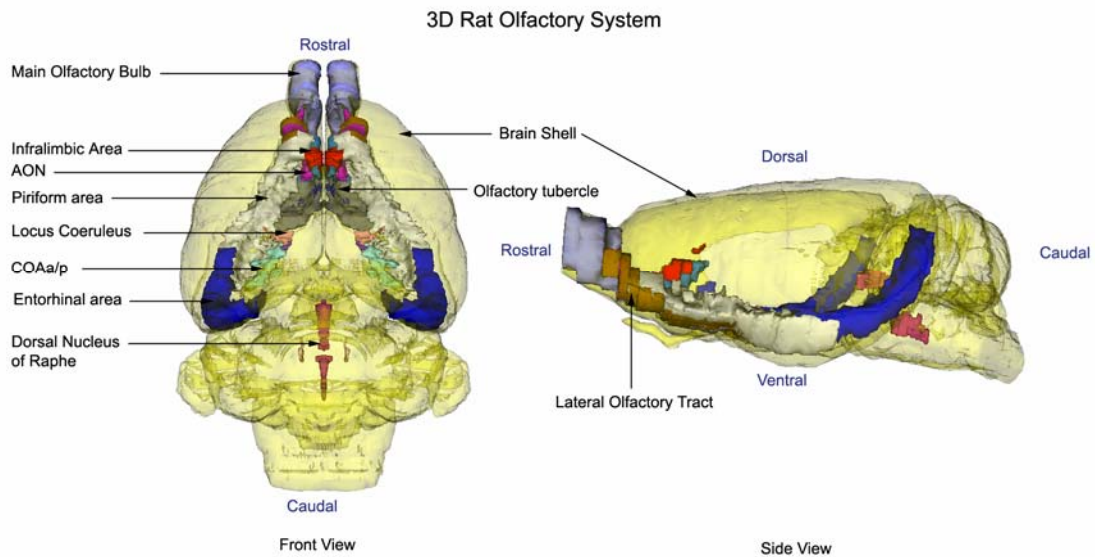


Figure 6.3: Rat olfactory system

6.2 Methods and Material

6.2.1 Animals

Long-Evans male rats, 80-90 days old, were obtained from Charles River Laboratories (MA) and housed individually in 48 x 25 x 20 cm Plexiglas cages. Animals were maintained on a 12 hr light-dark cycle with lights on at 0700 hr and provided food and water ad libitum. Animals were acclimated to the rodent restrainer and the imaging protocol as described below. The use of animals adhered to the animal welfare act the document entitled "Principle for Use of Animals" and Guide for the Care and Use of Laboratory Animals." [100]

6.2.2 Animal Restrainer

Studies were performed with a multi-concentric dual-coil, small animal restrainer (Insight Neuroimaging Systems, LLC, Worcester MA). In brief, just prior to the imaging session, rats were anesthetized with 4% isoflurane. A topical anesthetic of 2-5% lidocaine gel was applied to the skin and soft tissue around the ear canals and over the bridge of the nose. A plastic semicircular headpiece with blunted ear supports that fit into the ear canals was positioned over the ears. The head was placed into a cylindrical head holder with the animal's canines secured over a bite bar and ears positioned inside the head holder with adjustable screws fitted into lateral sleeves. An adjustable surface coil built into the head holder was pressed firmly on the head and locked into place. The body of the animal was placed into a body restrainer. The body restrainer "floats" down the center of the chassis connecting at the front and rear end-plates and buffered by rubber gaskets. The head piece locks into a mounting post on the front of the chassis.

This design isolates body movements from the head restrainer and minimizes motion artifact. Once the animal was positioned in the body holder, a volume coil was slid over the head restrainer and locked into position.

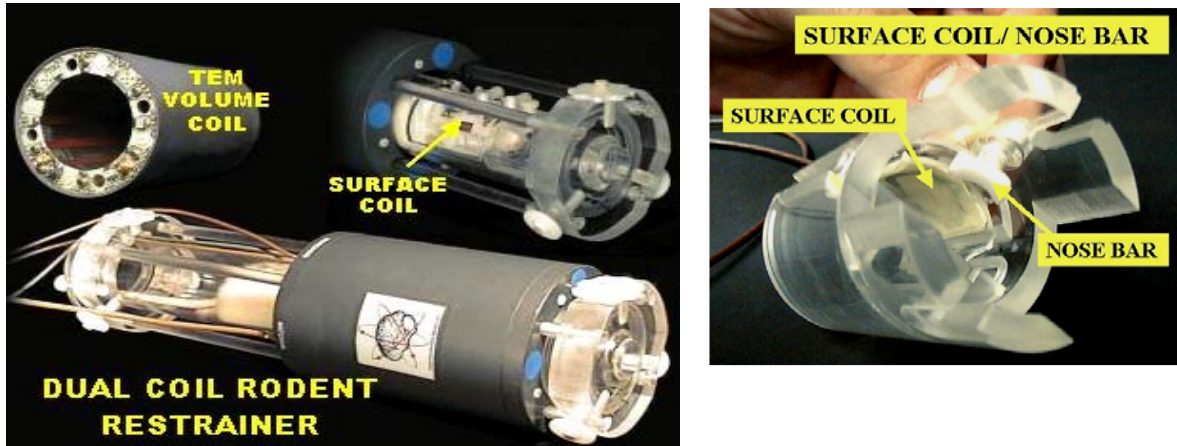


Figure 6.4: Studies were performed with a multi-concentric dual-coil, small animal restrainer developed by Insight Neuroimaging Systems, LLC, (Worcester, MA).

6.2.3 Acclimating Animals to the Imaging Protocol

Prior to imaging, animals were routinely acclimated to the restrainer and the imaging. Animals were anesthetized with isoflurane as described above for securing the animal into the restrainer. When fully conscious, the restraining unit was placed into a black opaque tube “mock scanner” with a tape-recording of an MRI pulse sequence for 90 min in order to simulate the bore of the magnet and an imaging protocol. This procedure was repeated every other day for four days and has been used successfully in several awake imaging studies to acclimate rats to the restrainer and imaging protocol [58, 59, 60, 62, 63, 64, 65, 66, 67]. Rats show a significant decline in body temperature, motor movements, heart rate and plasma corticosterone levels when comparing the first to the last acclimation periods. [67]

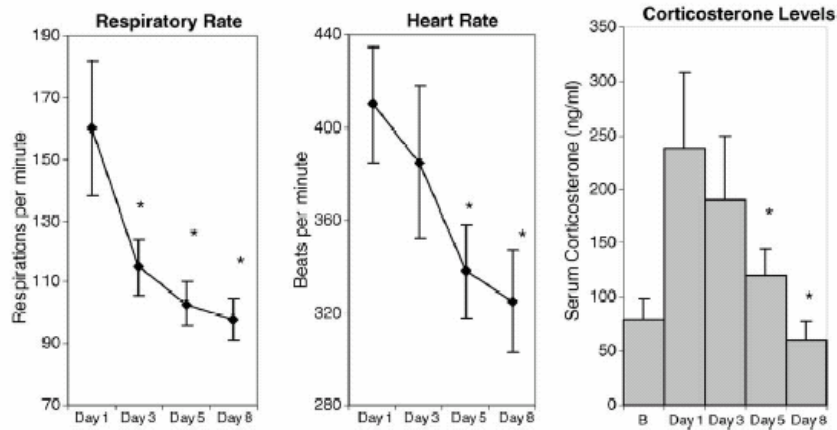


Figure 6.5: With repeated restraint and exposure to a simulated imaging session rats show reduced autonomic and endocrine measures of stress [67].

6.2.4 Imaging Protocol

Experiments were conducted in a Bruker Biospec 4.7-T/40-cm horizontal magnet (Oxford Instrument, Oxford, U.K.) equipped with a Biospec Bruker console (Bruker, Billerica, MA U.S.A) and a 20-G/cm magnetic field gradient insert (ID = 12 cm) capable of a 120- μ s rise time (Bruker). Radiofrequency signals were sent and received with the dual coil electronics built into the animal restrainer [68]. The volume coil for sending RF signal features an 8-element microstrip line configuration that, in conjunction with an outer copper shield, forms a TEM resonator structure. The arch-shaped geometry of the receiving surface coil provides excellent coverage and high signal-to-noise. To prevent mutual coil interference, the volume and surface coils were actively tuned and detuned. Figure 6.6 shows the Bruker 4.7 T/ 40-cm horizontal magnet.



Figure 6.6: Bruker Biospec 4.7T/40cm horizontal magnet (Oxford Instruments, U.K.) equipped with a Biospec Bruker console (Bruker, MA, U.S.A) and a 20-G/cm magnetic field gradient insert.

Functional images were acquired using a multi-slice fast spin echo sequence. A single data acquisition acquired twelve, 1.5 mm slices in 6 sec (FOV 3.0 cm; data matrix 64 x 64; TR 1.4 sec TE 7 msec; NEX 1). This sequence was repeated 150 times in an 15 min imaging session consisting of 3 min of baseline data followed by 4.5 min of stimulation data and then 7.5 min of control. At the end of each imaging session a high resolution anatomical data set was collected using the RARE pulse sequence (12 slice; 1.5 mm; FOV 3.0 cm; 256 X 256; TR 2.1 sec; TE 12.4 msec; NEX 12; 10 min acquisition time).

6.3 Experiment Design

Olfactory response from four odorants (stimulants) were studied using same set of ten animals. The four odorants were;

1. Benzaldehyde (Almond odor)
2. Iso-amyl acetate (Banana odor)
3. Methyl Benzoate (Rosy odor)
4. Limonene. (citrus odor)

In rats the duration, volume and velocity of sniff are important determinants of an odor stimulating effectiveness [6]. For each condition, male rats were exposed to 1% concentration odor for a four and half minute stimulation period. All animals were temporally anesthetized with 4% isoflurane, secured in the holder and allowed to awaken. A nozzle was placed in front of the nose that is connected to air pump outside of the magnet room by plastic tubing. An odorant bottle was connected between nozzle and air pump during stimulation period. A constant airflow was maintained during experiment.

For each session five scans were collected; the sequence of scans was as follows.

1. Anatomy scans 1.
2. Functional scan of 10% CO₂ challenge.
3. Anatomy scans 2.
4. Functional scan of 1% odorant.
5. Anatomy scans 3.

Anatomy images for each subject were obtained at a resolution of $256^2 \times 12$ slices and a FOV of 30mm with a slice thickness of 1.5 mm. Subsequent functional imaging was performed at a resolution of $64^2 \times 12$ slices with the same FOV and slice thickness.

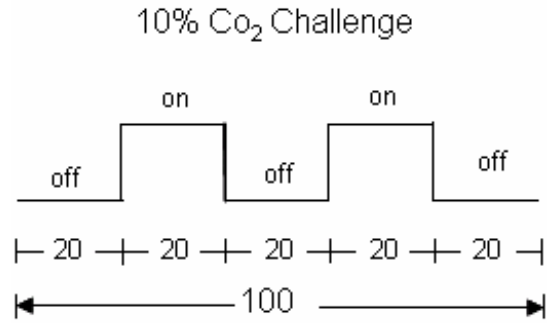


Figure 6.7: Block diagram for CO₂ challenge.

CO₂ challenge (hypercapnia) scan was collect to check brain performance and animal condition. Hypercapnia results in a passive dilation of blood vessel that increases blood flow [70, 71]. In conscious animals hypercapnia produces significantly greater increase MR signal (6% to 13%) as compared to anesthetized (2% to 4%) animals [69]. Data was collects for 2 cycles of two minutes off (control) and two minutes on condition. Figure 6.7 shows schematic diagram of 10% CO₂ challenge scan.

Functional scans of odorant stimulation were collected for 15 (150 scans) minutes. Acquisitions were performed with a period of 6s each scan at one time point. First 3 minutes (30 scans) of control/ baseline was collected followed by 4.5 minutes (45 scans) of stimulation. Remaining 7.5 minutes (75 scans) of baseline were collected but never used in the analysis. Figure 6.8 shows schematic diagram of 1% odorant challenge.

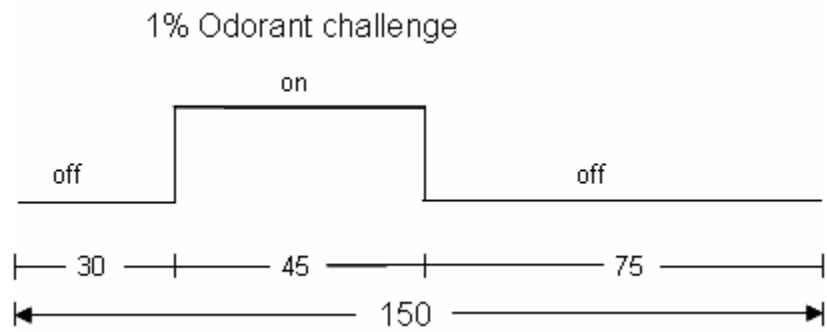


Figure 6.8: Schematic diagram of 1% odorant challenge.

After the functional sequences, repeated anatomy images were collected and compared with the initial anatomy image sets. Motion artifact was assessed by: (1) subtraction of anatomical data across the imaging session and (2) qualitative analysis of time-series movies looking for voxel displacement. The multiple data sets collected from these imaging sessions showed very little motion artifact using these criteria. There were no discernable differences in motion artifact as a function of stimulus type. On rare occasions, there would be a course spike; the data for these images were excluded. Figure 6.9 shows anatomy image collected before and after functional scan and subtraction of those two images for assessment of motion.

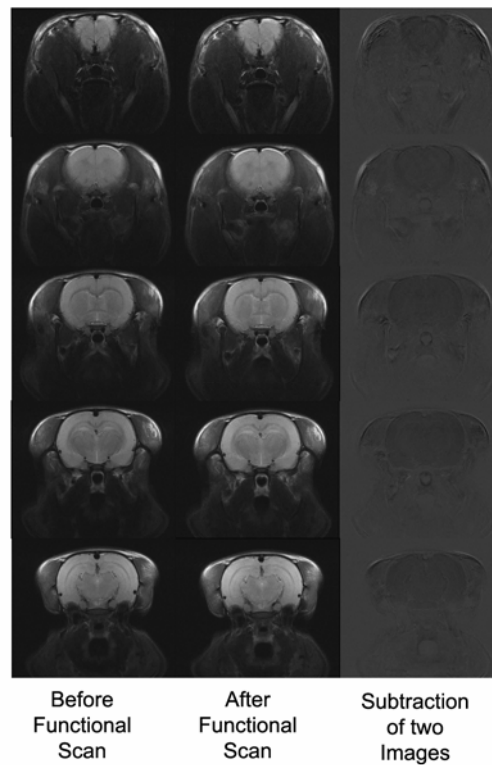


Figure 6.9: Motion artifact assessments by subtraction of images.

6.4 Data Analysis

Complete data analysis was performed using fMRI module in MIVA. To summarize the analysis process: Each subject was registered or aligned to a fully segmented rat brain. The affine registration involved translation, rotation, and scaling in all three dimensions, independently. Figure 6.10 shows intra registration where four representative subjects were registered to standard image. In Figure 6.10 iron color foreground images is standard and gray color background images are four different subjects.

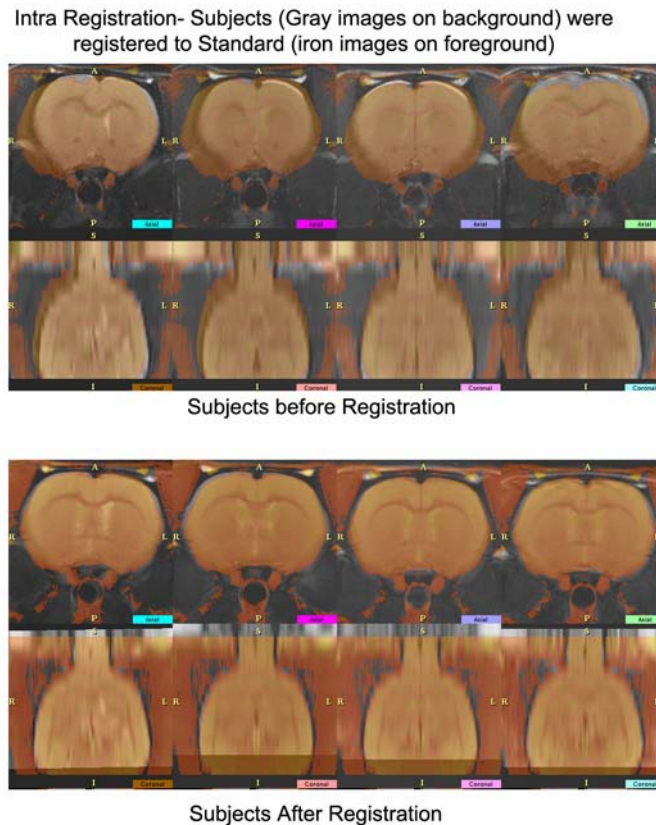


Figure 6.10: Registration of four different subjects to standard subject.

Figure 6.11 shows registration of standard image to Atlas. The colored segmented image in the foreground is Rat atlas and gray background image is standard image.

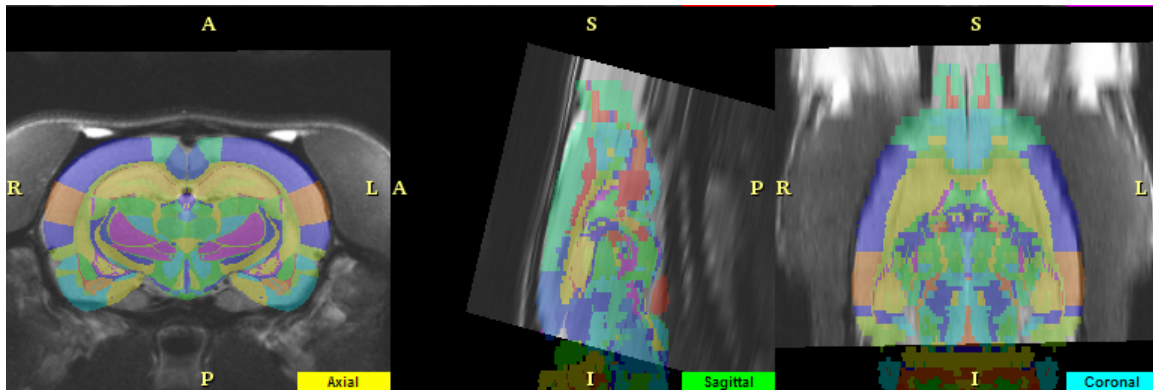


Figure 6.11: Registration of standard image to Rat Atlas.

The matrices that transformed the subject's anatomy to the atlas space were used to embed each slice within the atlas. All transformed pixel locations of the anatomy images were tagged with the segmented atlas major and minor regions creating a fully segmented representation of each subject. The inverse transformation matrix $[Ti]^{-1}$ for each subject (i) was also calculated. Statistical t tests were performed on each subject within their original coordinate system. The control window was the first 30 time periods. The stimulation window was the 45 time periods. The t test statistics used a 95% confidence level, two-tailed distributions, and heteroscedastic variance assumptions. As a result of the multiple t test analyses performed, a false-positive detection controlling mechanism was introduced. This subsequent filter guaranteed that, on average, the false-positive detection rate was below our cutoff of 0.05. These analysis settings provided conservative estimates for significance. Those pixels deemed statistically significant retained their percentage change values (stimulation mean minus control mean) relative to control mean. All other pixel values were set to zero.

A statistical composite was created for each group. The average value from all subjects within the group determined the composite value. The BOLD response maps of the composite were somewhat broader in their spatial coverage than in an individual subject; so only average number of activated pixels that has highest composite percent change values in particular ROI was displayed in composite map. Activated composite pixels are calculated as follows:

$$Activated\ Composite\ Pixels\ ROI\ (j) = \frac{\sum_{i=1}^N Activated\ Pixels\ Subject\ (i)\ ROI\ (j)}{N}$$

The composite percent change for the time history graphs for each region was based on the weighted average of each subject, as follows:

$$Composite\ Percent\ Change = \frac{\sum_{i=1}^N Activated\ Pixel\ Subject\ (i) \times Percent\ Change\ (i)}{Activated\ Composite\ Pixels}$$

where N is number of subjects.

Figure 6.12 shows positive activation in axial slices of different subjects and composite map that is laid out on the foreground of Atlas.

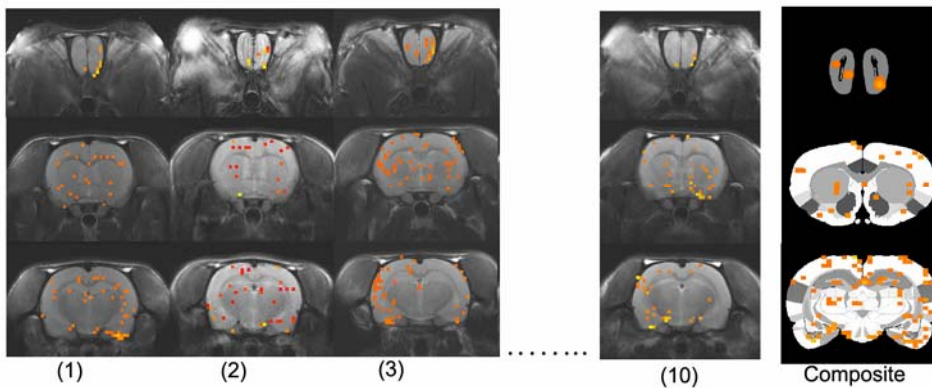


Figure 6.12: Composite map of ten different subjects was created to map olfactory system.

6.5 Results and Discussion

A priori hypothesis would predict activation of primary (main) olfactory system (MOS). Figure 6.13 shows 2D axial slices of activation maps in olfactory system.

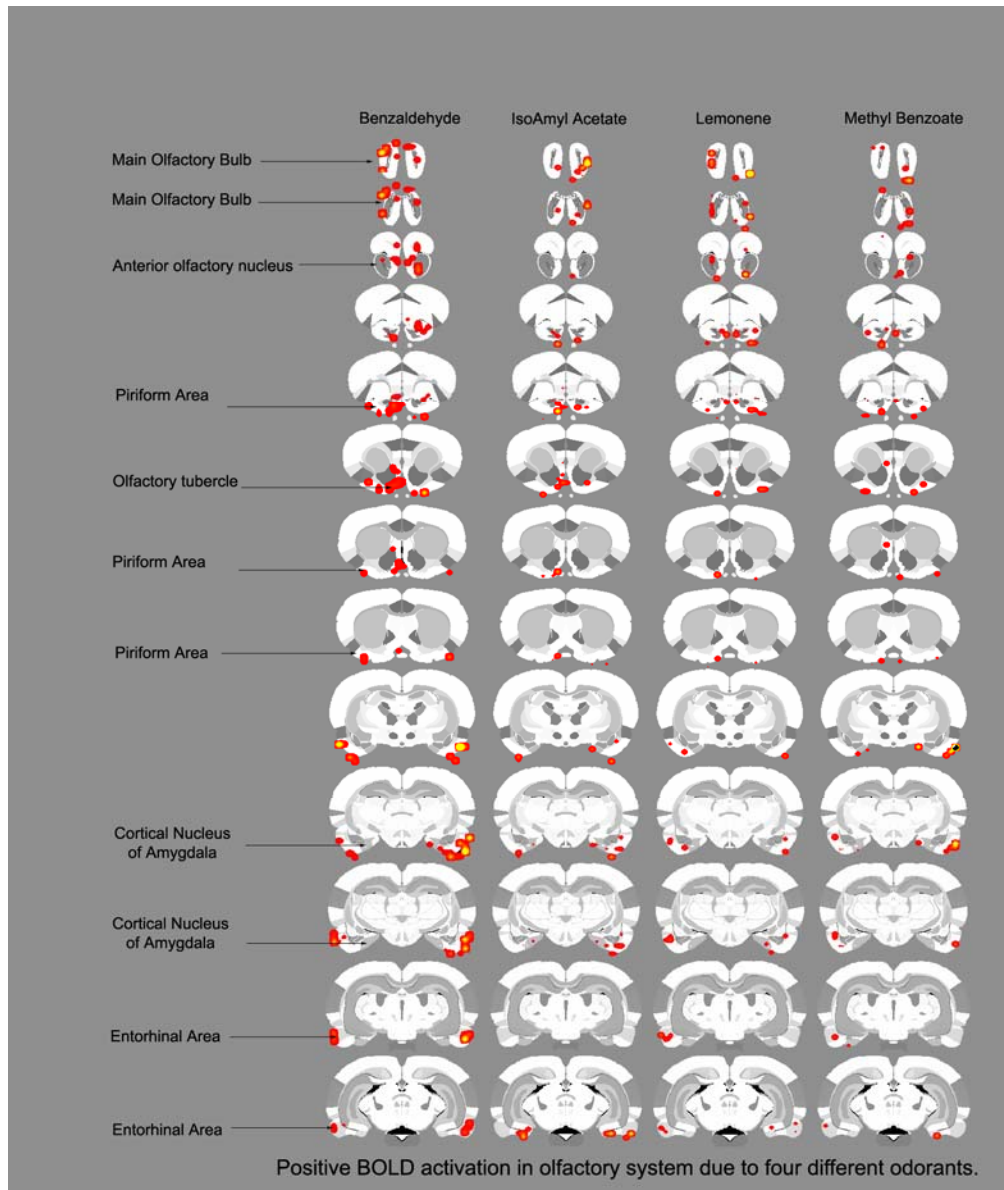


Figure 6.13: Activation in primary olfactory system due to four odorants.

Figure 6.14 shows comparison of number of voxels of three odorants (Isoamyl acetate, Lemonene, Methyl Benzoate) with Benzaldehyde. The aim here was to determine if there is any significance difference in number of voxels activated by particular odorant.

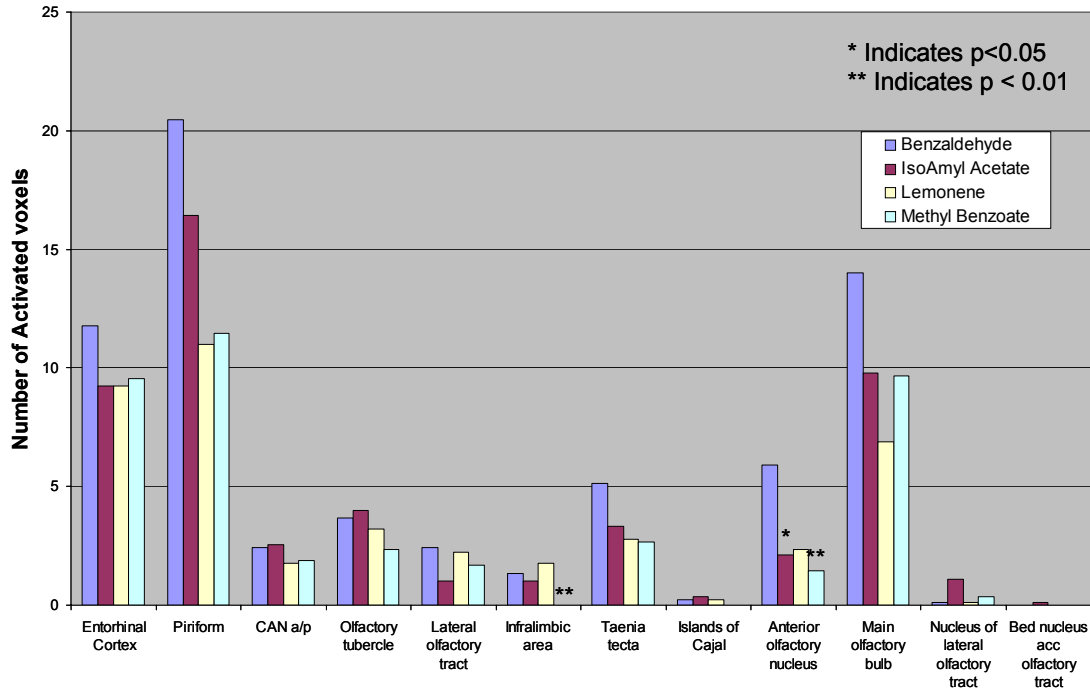


Figure 6.14: Comparison of number of voxels activated in different ROIs of Primary Olfactory system

From figure 6.13 and 6.14 it is quite evident that there is no significant difference in number of activated voxels in different ROIs of MOS. This supports the hypothesis that these areas are part MOS and are involved in interpretation of volatile odorants.

The forte of the system developed in this work is not limited to hypothesis based analysis as are other software programs available commercially or as openware. A neuroscientist or researcher can simply choose to analyze all regions with all major areas, sub-major area or combination of them. Once the analysis is done he/she can visualize the data by laying over positive and negative activation maps over atlas and investigate response from the stimulus. The neuroscientist can look at the csv file, which can be opened into any spreadsheet program, generated by fMRI module. This file gives quantitative information of;

1. positive and negative number of voxels per ROI per subject and their averages,
2. positive and negative percent change in BOLD signal per ROI per subject and their average.

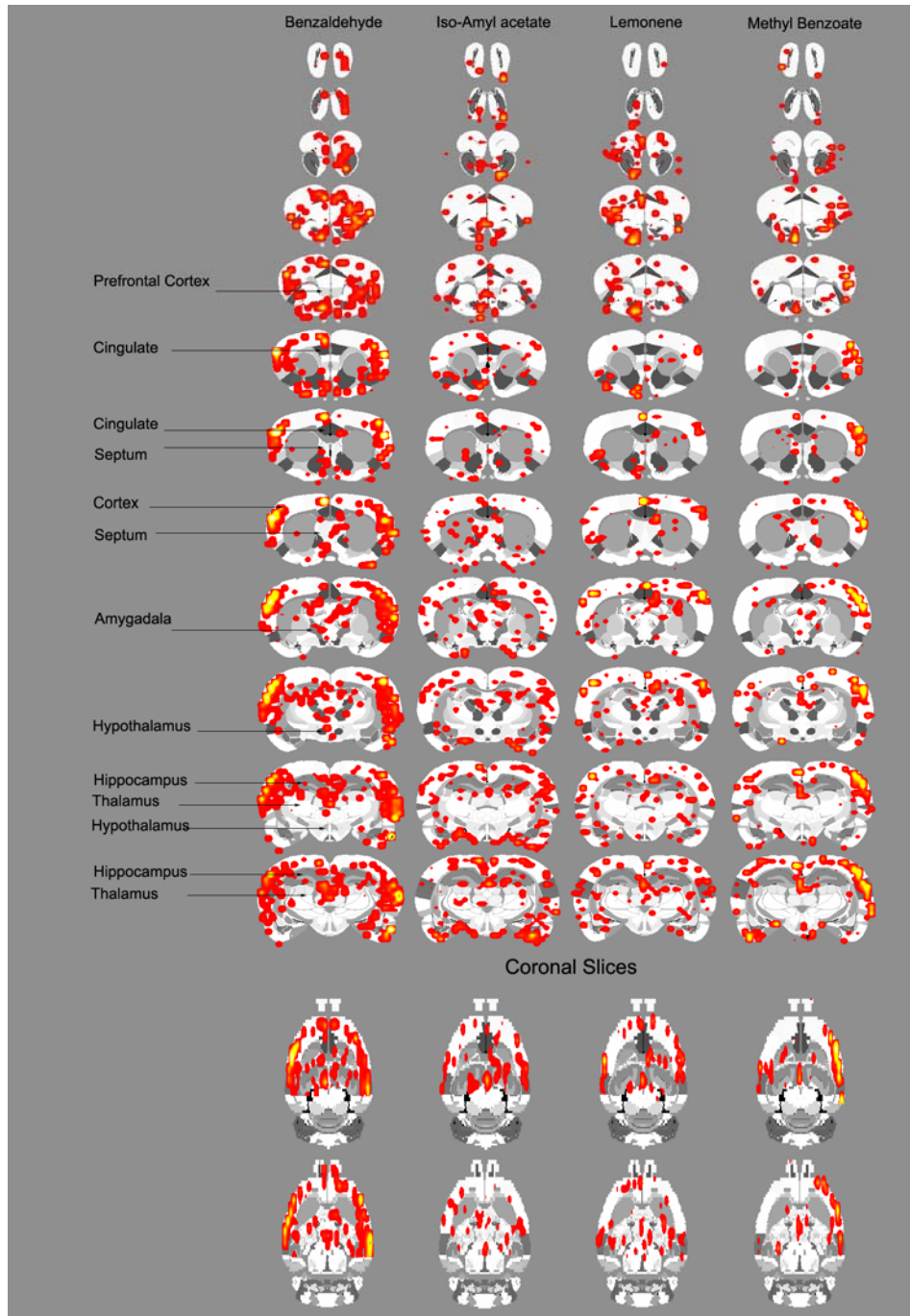


Figure 6.15: Whole brain responses from four odorants axial and coronal views.

Figure 6.15 shows positive activation maps of whole brain analysis for four odorants. One can easily see that response from Benzaldehyde is quite different from rest of the three odorants. A significant difference was found in number activated voxels in neocortical area, hippocampus, hypothalamus, thalamus, amygdala, septum and cingulated gyrus. These are the areas that constitute limbic system that is responsible for emotions, pleasure and memory formation [72,73].

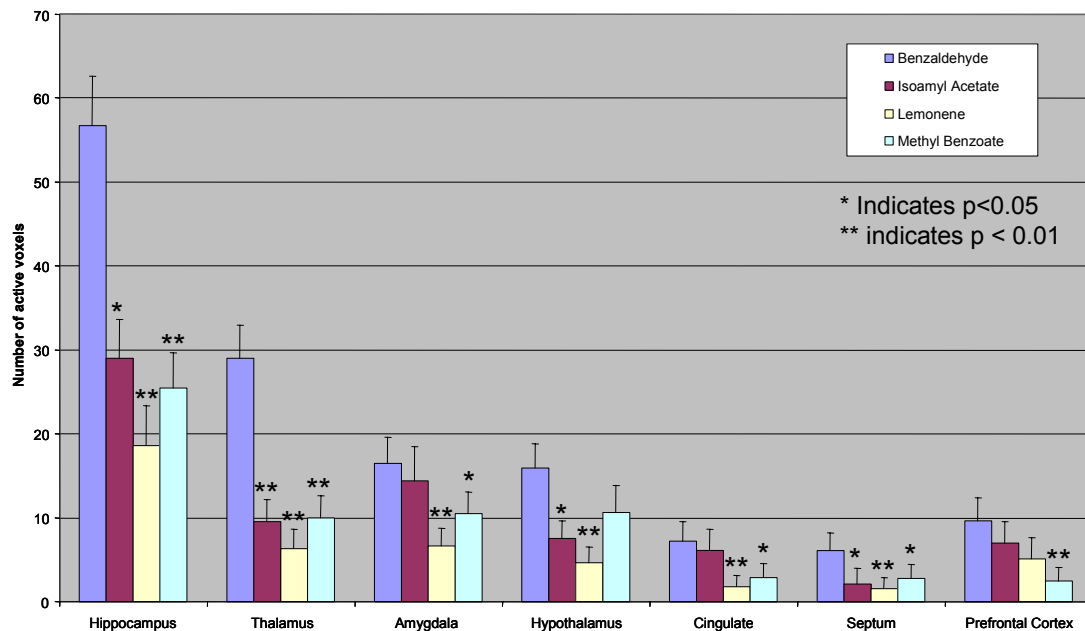


Figure 6.16: Comparison of number of activated voxels of three odorants with Benzaldehyde

Figure 6.16 shows comparison of number of activated voxels in areas of limbic system. Bar graph shows that brain activity due to benzaldehyde is significantly different than other three odorants in limbic system. This can be attributed to the fact that Benzaldehyde has an almond smell which is a nut and nuts are major food source for rats. The smell of food instigates limbic-thalamic system in rat's brain. The emotional valiance of benzaldehyde can be further investigated and confirmed using behavior studies which are beyond scope of this dissertation.

7: Conclusions

The ability to image brain activity noninvasively using BOLD fMRI was a remarkable development in the last decade. The fMRI module developed in this work provides a robust tool for neuroscientists to measure, quantify and visualize brain activity.

In this work a quantitative analysis strategy was successfully developed, implemented and optimized for the rat brain. Therein, each subject was registered, semi-automatically or manually, to a complete volume-segmented rat atlas containing a dozen major volumes of interest as well as more than 1000 detailed sub-volumes that, when coalesced, form approximately 100 sub-major regions of the rat brain. These sub-major regions were collected into the dozen major regions of the brain, e.g. amygdaloid complex, cerebrum, cerebellum, hypothalamus, etc. In addition the atlas was segmented to represent functional neuro-anatomical systems including the primary olfactory systems, limbic system and reward system.

A mapping algorithm classifies registered fMRI image voxels of all subjects to selected ROIs based on atlas information. Creating ROIs with this mapping technique is extremely fast and accurate as compared to manual ROI drawings.

Statistical t-tests were performed on each subject within their original coordinate system. User specified control and stimulation windows defined the image acquisition analysis periods. The imaging is continuous without interruption. The tests statistics used a confidence level, usually 95%, two-tailed distributions and heteroscedastic variance assumptions. Due to the multiple t-test analyzes performed, a false-positive detection controlling mechanism was introduced. This subsequent filter guarantees that, on

average, the false-positive detection rate is below the specified cutoff (0.05 in these datasets). These analysis settings provided conservative estimates for significance. Those pixels deemed statistically significant, retained their percent change values, relative to control mean. All other pixel values are set to zero.

A statistical composite was created for each group automatically. The individual analyses were summed within groups. The composite statistics were built using the inverse transformation matrices. The use of $[T_i]^{-1}$ ensured that the full volume set of the composite was populated with subject contributions. The average value from all subjects within the group determined the composite value.

Power of this system was demonstrated by mapping olfactory system of rat brain. Synchronized changes in neuronal activity across multiple subjects and brain areas can be viewed as functional neuro-anatomical circuits coordinating the thoughts, memories and emotions for particular behaviors using this fMRI module.

References

- 1) Savoy, R. "History and future directions of human brain mapping and functional Neuroimaging." *Acta Psychologica*, 107, 9 – 42, 2001.
- 2) Ogawa S, Lee TM, Nayak AS, Glynn P. Oxygenation-sensitive contrast in magnetic resonance image of rodent brain at high magnetic fields. *Magn Reson Med* 1990; 14:68-78.
- 3) Ogawa S, Menon R, Kim S, Ugrubil K, On the characteristics of functional magnetic resonance imaging of the brain. *Annual Rev. Biophys. Biomol. Struct.* 1998; 27:447-474.
- 4) Functional Magnetic Resonance Imaging, Mark S. Cohen, Susan Y. Bookheimer; UCLA Brain mapping center; Los Angeles, CA 90095
- 5) A Primer on MRI and Functional MRI (version 2.1, 6/21/01) Douglas C. Noll, Ph.D. Departments of Biomedical Engineering and Radiology University of Michigan, Ann Arbor, MI 48109-2125
- 6) Paxinos G, *The rat Nervous system* (second edition) Academic. (1994).
- 7) C.S. Springer, C.S. Patlak, I. Palyka, and W. Huang,, Principles of Bulk Magnetic Susceptibility and the Sign of the fMRI Response, *Functional Magnetic Resonance Imaging*, Ed. by C.T.W. Moonen and P.A. Bandettini; Springer-Verlag, New York , pp. 91- 102 (1999).
- 8) Kwong, K. K., Belliveau, J. W., Chesler, D. A., Goldberg, I. E., Weisskoff, R. M., Poncelet, B. P., Kennedy, D. N., Hoppel, B. E., Cohen, M. S., Turner, R., Cheng, H.-M., Brady, T. J., & Rosen, B. R. "Dynamic magnetic resonance

- imaging of human brain activity during primary sensory stimulation.” Proc Natl Acad Sci USA, 89, 5675-5679, (1992). .
- 9) Ogawa, S., D.W. Tank, R. Menon, *et al.*, Intrinsic signal changes accompanying sensory stimulation: Functional brain mapping with magnetic resonance imaging. *Proc. Natl. Acad. Sci., USA*, 1992. 89: p. 5951-5955.
 - 10) Keller, P. Basic Principles of MR Imaging. GE Medical Systems, Milwaukee (1988).
 - 11) Roy, C.S. and C.S. Sherrington, On the regulation of the blood-supply of the brain. *J Physiol (London)*, 1890. **11**: p. 85-108.
 - 12) Swanson, L.W.; *Brain Maps: Structure of the Rat Brain*, Second Edition, Elsevier, 1998
 - 13) Cubic Spline, <http://mathworld.wolfram.com/CubicSpline.html>
 - 14) Kulkarni, P.P.; Sullivan, J.M.; Ghadyani, H.R.; Huang, W.; Wu, Z.; King, A. “Automatic Segmentation of a Rat Brain Atlas via a Multiple-Material Marching Cube Strategy”, *Proc. Intl. Soc. Mag. Reson. Med.* 11(2003), Canada
 - 15) Wu, Ziji; Sullivan, John M., Jr. “Multiple material marching cubes algorithm”, *International Journal for Numerical Methods in Engineering*, 58(2):189-207, July 2003
 - 16) W. Huang, J.M. Sullivan, Jr., R. Ludwig, P. Kulkarni, J.Q. Zhang, J.A. King, “Stair-Stepped Removal via Automatic Linearization for Marching Cubes Formulations”, *Proc. 12th Intl. Soc. Mag. Reson. Med.*, No. 756, (2004).

- 17) Habboush, Mitchell, K.D., Mulkern, R.V., Barnes, P.D. and Treves, S.T., “Registration and Alignment of Three-Dimensional Images: An Interactive Visual Approach”, *Radiology*, Vol.199, pp: 573-578, (1996).
- 18) J.Q. Zhang, J.M. Sullivan, Jr., P.P. Kulkarni, M. Brevard, U. Benz, and H.L.Yu, "Intermodality Registration via Interactive Graphics Coupled with A.I.R. Intramodality Registration", *Proc. 11th Intl. Soc. Mag. Reson. Med.*, No. 3430, (2003).
- 19) Woods, R.P., Grafton, S.T., Holmes, C.J., Cherry, S.R. and Mazziotta, J.C., “Automated Image Registration: I. General Methods and Intrasubject, intramodality Validation”, *Journal of Computer Assisted Tomography*, Vol. 12, p: 153-165, (1994).
- 20) Woods, R.P., Grafton, S.T., Watson, J.D.G., Sicotte, N.L. and Mazziotta, J.C., “Automated Image Registration: II. Intersubject Validation of Linear and Nonlinear Models”, Vol, (1994).
- 21) Woods, R.P., Cherry, S.R. and Mazziotta, J.C., “Rapid Automated Algorithm for Aligning and Reslicing PET Images”, *Journal of Computer Assisted Tomography*, Vol.16, pp: 620-633, (1994).
- 22) Wells, W.M., Viola, P., Atsumi, H., Nakajima, S. and Kikinis, R., “Multi-modal volume registration by maximization of mutual information”, *Medical Image Analysis*, Vol. 1, pp: 35-51, (1996).
- 23) Viola, P. and Wells, W.M., “Alignment by maximization of mutual information”, *Journal of Computer Vision*, Vol. 24, pp: 137-154, (1997).

- 24) Maes, F., Collignon, A., Vandermeulen, D., Marchal, G. and Suetens, P.,
 “Multimodality Image Registration by Maximization of Mutual Information”,
 IEEE, Transactions on Medical Imaging, Vol.16, pg: 187-198, (1997).
- 25) Shannon, C.E., “A Mathematical Theory of Communication”, Reprinted with
 corrections from The Bell System Technical Journal Vol. 27, pg: 379–423,
 623–656, (1948).
- 26) Yu, H.L., Sullivan, J.M., Ghadyani, H.R., Zhang, J.Q., “Image Registration
 by Global Maximization of Mutual Information Based on a Genetic
 Algorithm”, International Society for Magnetic Resonance in Medicine,
 (2005).
- 27) Woods R P, Grafton S T, Holmes C J, Cherry S R, Mazziotta J C. Automated
 image registration: I. General methods and intrasubject, intramodality
 validation. *Journal of Computer Assisted Tomography* 1998;22:139-152.
- 28) Jasjit, S.S.; Sameer S.; Laura R.; *Computer Vision and Pattern Recognition
 Techniques for 2-D and 3-D MR Cerebral Cortical Segmentation (Part I): A
 State-of-the-Art Review*, *Pattern Analysis and applications* 5:77-98, 2002
- 29) Wu, Z., K.D. Paulsen, and J.M. Sullivan, Jr., "Adaptive Model Initialization
 and Deformation for Automatic Segmentation of T1-weighted Brain MRI
 Data" *IEEE Trans. Biomed. Eng.*, V52, No 6, p1128-1131, (2005)
- 30) M. Murugavel, J.M. Sullivan, Jr., P.P. Kulkarni, "An Integrated Volume
 Approach Enhances the Accuracy of Functional Voxel Classifications", *Proc.
 13th Intl. Soc. Mag. Reson. Med.*, No 1565, Miami, FL, (2005).

- 31) Spiridon, M. & Kanwisher, N. (2002) How distributed is visual category information in human occipital-temporal cortex? An fMRI study. *Neuron*. 35 (6) 1157-1165
- 32) Culham, J., Cavanagh, P., & Kanwisher, N. (2001) Attention Response Functions: Characterizing Brain Areas Using fMRI Activation during Parametric Variations of Attentional Load. *Neuron*. 32 737-745
- 33) P.P.Kulkarni, J.M.Sullivan, Jr., J.A.Harder, T.L.Messenger, C.F.Ferris, "Cocaine suppresses reward circuitry in lactating dams: Evidence from functional MRI and 3D computational analyses" 34th annual meeting, The Society of Neuroscience. San Diego, 2004.
- 34) Ferris CF, Kulkarni PP, Sullivan, JM, Harder JA, Messenger TL, Feibo M, "Pup suckling is more rewarding than cocaine: Evidence from functional MRI and 3D computational analysis." *J.Neuroscience* 25:149-156, 2005.
- 35) Purdon PL and Weisskoff RM, "Effect of temporal autocorrelation due to physiological noise and stimulus paradigm on voxel-level false-positive rates in fMRI." *Human Brain Mapping* 6: 239-249, 1998.
- 36) Buxton R.B. "Introduction to functional magnetic resonance imaging: Principles and techniques" Cambridge University Press, ISBN: 0-521-58113-3, 2002.
- 37) Friston KJ, Jezzard P and Turner R, (1994) Analysis of Functional MRI Time-Series. *Human Brain Mapping* 1,153-171.
- 38) Christopher R. Genovese, Nicole A. Lazar, Thomas E. Nichols, "Thresholding of Statistical Maps in Functional Neuroimaging Using the False Discovery Rate". *NeuroImage* 15:870-878, 2002.

- 39) Benjamini Y, Hochberg Y, "Controlling the false discovery rate: a practical and powerful approach to multiple testing" *J. R. statist. soc. B* 57, No1, pp 289-300, (1995).
- 40) Goldberg S., J. Turpin and S. Price, Anisole binding protein from olfactory epithelium evidence for a role in transduction, *Chem. Senses & Flavour*, 4:207 (1979).
- 41) Fesenko E.E., V.I. Nonoselov and L.D. Krapivinskaya, Molecular mechanisms of olfactory reception, *Biochim. Biophys. Acta*, 587:424 (1979).
- 42) Lacazette E, Gachon AM, Pitiot G., A novel human odorant-binding protein gene family resulting from genomic duplicons at 9q34: differential expression in the oral and genital spheres, *Hum Mol Genet*, Jan 22;9(2):289-301 (2000)
- 43) Price, S., Willey, A., Effects of antibodies against odorant binding proteins on electrophysical responses to odorants, *Biochem Biophys Acta*, 965: 127ff (1988)
- 44) Langedijk AC, Spinelli S, Anguille C, Hermans P, Nederlof J, Butenandt J, Honegger A, Cambillau C, Pluckthun A., Insight into odorant perception: the crystal structure and binding characteristics of antibody fragments directed against the musk odorant traseolide, *J Mol Biol* 1999 Oct 1;292(4):855-69
- 45) Wysocki CJ. "Neurobehavioral evidence for the involvement of the vomeronasal system in mammalian reproduction" *Neurosci Biobehav Rev.* 1979 Winter;3(4):301-41
- 46) Ferris CF, Snowdon CT, King JA, Duong TQ, Ziegler TE, Ugurbil K, Ludwig, R, Schultz-Darken NJ, Wu Z, Olson DP, Sullivan JM, Tannenbaum

- PL, Vaughan JT, "Functional imaging of brain activity in conscious monkeys responding to sexually arousing cues" *Neuroreport*. 12(10):2231-2236, 2001.
- 47) Ferris CF, Snowdon CT, King JA, Duong TQ, Ziegler TE, Ugurbil K, Ludwig, R, Schultz-Darken NJ, Wu Z, Olson DP, Sullivan JM, Tannenbaum PL, Vaughan JT, "Activation of neural pathways associated with sexual arousal in non-human primates" *Journal of Magnetic Resonance Imaging* Volume 19, Issue 2 , Pages 168 – 175, 2004.
- 48) J.A. King, C.F. Ferris, T.Q. Duong, R Ludwig, J.M. Sullivan, Jr., M. Does, "Functional Imaging of Brain Activity in Conscious Animals: The Smell of Fear" *Proc. 10th Intl. Soc. Mag. Reson. Med*, No. 1352, (2002).
- 49) Institute of biological information processing. <http://www.fz-juelich.de/ibi/ibi-1/Chemosensation>
- 50) V.S. Caviness, Jr. and R.L. Sidman, Olfactory structures of the forebrain in the reeler mutant mouse. *J Comp Neurol* **145** (1972), pp. 85–104.
- 51) J. De Olmos, H. Hardy and L. Heimer, The afferent connections of the main and accessory olfactory bulb formations in the rat: An experimental HRP-study. *J Comp Neurol* **181** (1978), pp. 213–244
- 52) L.B. Haberly and J.L. Price, Association and commissural fiber systems of the olfactory cortex of the rat. I. Systems originating in the pyriform cortex and adjacent areas. *J Comp Neurol* **178** (1978), pp. 711–740.
- 53) L. Heimer, The olfactory cortex and ventral striatum. In: Kenneth E. Livingston and Okek Hornykiewicz, Editors, *Limbic Mechanisms: the*

- Continuing Evolution of the Limbic System Concept*, Plenum Press, New York (1975), pp. 95–189.
- 54) K.C. Kosel, G. Van Hoesen and I.R. West, Olfactory bulb projections to the parahippocampal area of the rat. *J Comp Neurol* **198** (1981), pp. 467–482.
- 55) F. Macrides and B.J. Davis, The Olfactory Bulb. In: P.C. Emson, Editor, *Chemical Neuroanatomy*, Raven Press, New York (1983), pp. 391–426.
- 56) F. Scalia, Some olfactory pathways in the rabbit brain. *J Comp Neurol* **126** (1966), pp. 285–310.
- 57) Shepley M, Adamek G, “The connections of the mouse olfactory bulb: A study using orthograde and retrograde transport of wheat germ agglutinin conjugated to horseradish peroxidase” *Brain Research Bulletin*, 12(6), pp 669-688, 1984.
- 58) Febo M, Ferris CF, Segarra AC. Estrogen influences cocaine-induced blood oxygen level-dependent signal changes in female rats. *J Neurosci*. 2005 Feb 2;25(5):1132-6.
- 59) Ferris CF, Kulkarni P, Sullivan JM Jr, Harder JA, Messenger TL, Febo M. Pup suckling is more rewarding than cocaine: evidence from functional magnetic resonance imaging and three-dimensional computational analysis. *J Neurosci*. 2005 Jan 5;25(1):149-56.
- 60) Febo M, Segarra AC, Nair G, Schmidt K, Duong TQ, Ferris CF. The Neural Consequences of Repeated Cocaine Exposure Revealed by Functional MRI in Awake Rats. *Neuropsychopharmacology*. 2004 Dec 22.

- 61) Febo M, Segarra AC, Tenney JR, Brevard ME, Duong TQ, Ferris CF.
Imaging cocaine-induced changes in the mesocorticolimbic dopaminergic system of conscious rats. *J Neurosci Methods*. 2004 Oct 30;139(2):167-176.
- 62) Tenney JR, Marshall PC, King JA, Ferris CF. fMRI of generalized absence status epilepticus in conscious marmoset monkeys reveals corticothalamic activation. *Epilepsia*. 2004 Oct;45(10):1240-7.
- 63) Tenney JR, Duong TQ, King JA, Ferris CF. FMRI of brain activation in a genetic rat model of absence seizures. *Epilepsia*. 2004 Jun;45(6):576-82.
- 64) Brevard M, Meyer J, Ferris C. Imaging the Neural Pathways Activated by Oral MDMA in Conscious Marmosets. *Folia Primatol. (Basel)*. 2004; 75 (suppl 1). p221.
- 65) Ferris C. Functional Magnetic Resonance Imaging in Conscious Marmosets: Methods and Applications in Neuroscience Research. *Folia Primatol. (Basel)*. 2004; 75 (suppl 1). p220.
- 66) King J., Tenney J. Imaging gbl-induced absence seizures in marmoset monkeys. *Folia Primatol. (Basel)*. 2004; 75 (suppl 1). p221-222.
- 67) King J, Garelick T, Brevard M, Chen W, Messenger T, Duong T, Ferris C, “Procedure for minimizing stress for fMRI studies in conscious rats”, *J Neurosci Methods*, 148 ,154-160, 2005.
- 68) Ludwig R, Bodgdanov G, King J, Allard A, Ferris CF. A dual RF resonator system for high-field functional magnetic resonance imaging of small animals. *J Neurosci Methods*. 2004 Jan 30;132(2):125-35.

- 69) Brevard ME, Duong TQ, King JA, Ferris CF. Changes in MRI signal intensity during hypercapnic challenge under conscious and anesthetized conditions. *Magn Reson Imaging*. 2003 Nov;21(9):995-1001.
- 70) Grubb RL, Raichle ME, Eichling JO, Ter-Pogossian MM. The effects of changes in PaCO₂ on cerebral blood volume, blood flow, and vascular mean transit time. *Stroke* 1974;5(5):630–639.
- 71) Walker BR, Brizzee BL. Cardiovascular responses to hypoxia and hypercapnia in barodenervated rats. *J Appl Physiol* 1990;68(2):678–86.
- 72) Papez JW. A proposed mechanism of emotion. 1937. *J Neuropsychiatry Clin Neurosci*. 1995 Winter;7(1):103-12.
- 73) Sitoh YY, Tien RD. “The limbic system. An overview of the anatomy and its development.” *Neuroimaging Clin N Am*. 1997 Feb;7(1):1-10.
- 74) Pauling, L. and Coryell, C.D. (1936) The magnetic properties and structure of haemoglobin, oxyhaemoglobin and carbon monoxihaemoglobin. *Proc. Natl. Acad. Sci. U. S. A.* 22, 210–216
- 75) Thulborn, K.R. *et al.* (1982) Oxygenation dependence of the transverse relaxation time of water protons in whole blood at high field. *Biochim. Biophys. Acta* 714, 265–270
- 76) Hornak JP, “The Basics of MRI”
<http://www.cis.rit.edu/htbooks/mri/index.html>
- 77) Pfuhl M. “Description of NMR experiments I”.
<http://www.le.ac.uk/biochem/mp84/teaching/lecture2.html>

- 78) Ferris CF, Febo M, Luo, F, Schmidt K, Brevard M, Kulkarni PP, Messenger T, King JA, “Functional Magnetic Resonance Imaging in conscious animals: A new tool in behavioral neuroscience research” (2005) accepted at J Neuroendocrinology.
- 79) Studholme, C., Hill, D.L.G. and Hawkes, D.J., “Automated 3D MR and PET brain image registration”, Journal of Computer Assisted Radiology, pp: 248-253,1(1995).
- 80) Maintz, J.B.A., Elsen, V.D. and Viergever, M.A., “Evaluation of ridge seeking operators for multimodality medical image matching”, IEEE, Transactions on Pattern Analysis and Machine Intelligence, Vol.18, pp: 353 – 365, (1996).
- 81) Edwards, A. L. "The Correlation Coefficient." Ch. 4 in *An Introduction to Linear Regression and Correlation*. San Francisco, CA: W. H. Freeman, pp. 33-46, 1976.
- 82) Hajnal, J.V., Saeed, N., Soar, E.J., Oatridge, A., Young, I.R. and Bydder, G.M, “A Registration and Interpolation Procedure for Subvoxel Matching of Serially Acquired.MR Images”, Journal of Computer Assisted Tomography, Vol. 19, pp: 289-296,(1995).
- 83) Bezdek, J.C.; Hall, L.O.; et al; *Review of MR image segmentation using pattern recognition*, Med. Phys. 20:1033-1048, 1993
- 84) Koyama T, McHaffie JG, Laurienti PJ, Coghill RC, *The single-epoch design : validation of simplified paradigm for the collection of subjective ratings; J. NeuroImage19(2003) 976-987.*
- 85) W. H. Press W. T. Vetterling, and P. B. Flannery, *Numerical Recipe in C.* (Cambridge University Press, 1992).

- 86) Gruber SA,. (2002) Stroop performance in normal control subjects: An fMRI study. *NeuroImage*, 16, 349-360.
- 87) Kanwisher et al. (1997) The fusiform face area: a module in human extrastriate cortex specialized for face perception. *The Journal of Neuroscience*, 17, 4302-4311.
- 88) Price, C.J., et al. (1999) The critical relationship between the timing of stimulus presentation and data acquisition in blocked designs with fMRI. *Neuroimage*, 10, 36 - 44.
- 89) K.J. Friston, P. Jezzard, and R. Turner. Analysis of functional MRI time-series. *Human Brain Mapping*, 1:153-171, 1994.
- 90) K. J. Friston, A. P. Holmes, J.-B. Poline, P. J. Grasby, S. C. R. Williams, R. S. J. Frackowiak, and R. Turner. Analysis of fMRI time series revisited. *NeuroImage*, 2:45-53, 1995.
- 91) K. J. Worsley and K. J. Friston. Analysis of fMRI time-series revisited - again. *NeuroImage*, 2:173-181, 1995.
- 92) Kim S-G, Richter W, and Ugurbil K. Limitations of temporal resolution in fMRI. *Magn Reson Med* 1997; 37: 631-636.
- 93) Richter W, Andersen PM, Georgopoulos AP, and Kim S-G. Sequential activity in human motor areas during a delayed cued movement task studied by time-resolved fMRI. *NeuroReport* 1997; 8: 1257-1261.
- 94) Richter W, Ugurbil K, Georgopoulos AP, and Kim S-G. Time-resolved fMRI of mental rotation. *NeuroReport* 1997; 8: 3697-3702.

- 95) Benjamini Y, Yekutieli D, *The control of false discovery rate in multiple testing under dependency*. Technical report, Department of statistics and Operations research. Tel Aviv University (2001)
- 96) Clare, S., Humberstone, M., Hykin, J., Blumhardt, L., Bowtell, R. and Morris, P. (1999) 'Detecting Activations in Event-Related fMRI Using Analysis of Variance'. *Magnetic Resonance in Medicine*. 42 1117-1122.
- 97) Jezzard, P. and Clare, S. (2001) 'Principles of Nuclear Magnetic Resonance and MRI', in 'Functional Magnetic Resonance Imaging: An Introduction to Methods', Edited by Jezzard, Matthews and Smith, Oxford University Press, Oxford, pp.67-92
- 98) Ward BD, *Deconvolution analysis of FMRI time series data*. (2002) Afni documentation, Biophysics Research Institute, Medical of Wisconsin.
- 99) Neter J, Kutner MH, Nachtsheim CJ, Wasserman W, *Applied linear regression models*, 3rd edition, (1996) The McGraw-Hill Companies. ISBN 0-256-08601-X.
- 100) *Guide for the Care and Use of Laboratory Animals (ILAR)*, Institute of Laboratory Animal Resources Commission on ,Academy Press, Washington, D.C. 1996. <http://www.nap.edu/readingroom/books/labrats/>
- 101) SPM: <http://www.fil.ion.ucl.ac.uk/spm>
- 102) AFNI: <http://afni.nimh.nih.gov/afni>
- 103) Brain Voyager : <http://www.brainvoyager.de>
- 104) Stimulate : <http://www.cmrr.umn.edu/stimulate>
- 105) MIVA: <http://ccni.wpi.edu/cwbench/cwbench-tiles.jsp>

- 106) Tootell RB, Dale AM, Sereno MI, Malach R, (1996) *New Images from human visual cortex Trends in neuroscience* 19(11), 481-489.
- 107) Klob B, Whishaw IQ, (1996) *Fundamentals of human neuropsychology* (4th ed) New York Freeman.
- 108) Calvin WH, Ojemann GA, (1995) *Conversation with Neil Brain: The neural nature of thought and language* Reading, MA: Perseus Publishing.
- 109) Swartz BE, Goldensohn ES, (1998) *Timeline of the history of EEG and associated field* Electroencephalography and clinical Neuropsychology.